Quantum correlations of ultracold atoms in optical lattices

by

Shuming Li

B.A., Nanjing University, 2004

M.S., Chinese Academy of Science, 2007

A thesis submitted to the

Faculty of the Graduate School of the

University of Colorado in partial fulfillment

of the requirements for the degree of

Doctor of Philosophy

Department of Physics

2014

This thesis entitled:
Quantum correlations of ultracold atoms in optical lattices
written by Shuming Li
has been approved for the Department of Physics

Prof. Ana Maria Rey

Prof. John Bohn

Date

The final copy of this thesis has been examined by the signatories, and we find that both the content and the form meet acceptable presentation standards of scholarly work in the above mentioned discipline.

Li, Shuming (Ph.D., Physics)

Quantum correlations of ultracold atoms in optical lattices

Thesis directed by Prof. Ana Maria Rey

An optical lattice is the periodic potential that atoms experience via the ac-Stark shift when they are illuminated by counter-propagating laser beams that form a standing-wave pattern. Optical lattices have been widely used as a versatile platform in cooling, trapping, controlling atoms, and also for the study of a variety of problems in physics. The many-body states of ultracold atoms in optical lattices can be characterized by the quantum-correlations encoded in time-of-flight images. In this thesis, we mainly discuss the use of correlations function as a natural framework for characterizing quantum states in optical lattices.

The outline of the thesis is as follows. Chapter 1 gives a brief introduction to optical lattice potentials and ways for describing particles moving in a periodic potential. Chapter 2 explains the importance of correlations and discusses common methods to detect them in cold atom experiments.

Chapter 3 presents work done to study the many-body Schrödinger equation in a quasi-periodic potential and discusses its connection with the Kolmogorov-Arnold-Moser (KAM) problem of classical mechanics. We posed a possible visualization of such a connection in experimentally accessible many-body observables. These observables are useful probes for the three characteristic phases of the problem: the metallic, Anderson, and band-insulator phases. In addition, they exhibit fingerprints of nonlinear phenomena such as bifurcations and devil's staircases. Our numerical treatment is complemented with a perturbative analysis that provides insight on the underlying physics. The perturbative-theory approach is particularly useful in illuminating the distinction between the Anderson-insulator and the band-insulator phases in terms of paired sets of dimerized states.

Chapter 4 discusses several theoretical procedures developed to understand a recent experiment on macroscopic quantum self-trapping (ST) performed in a 2D optical lattice. Mean field and truncated-Wigner-approximation (TWA) calculations are performed trying to reproduce the experimental observations. The discrepancy between the theory and the experiment lead to the hypothesis of a new type of ST caused by strong correlations. We analyze toy models to support it.

Dedication

To my husband and my son.

Acknowledgements

I want to thank all the people who made this dissertation possible. First and foremost I would like to thank my advisor Ana Maria Rey for giving me the opportunity to join her group. For the past six years, she gave me not only very good advice and detailed guidance, but also the encouragement I needed to feel that the work I was doing was important and worthwhile. It has been a great pleasure to work with and learn from such an extraordinary person.

I also want to thank Prof. Indubala I. Satija from George Mason University and Prof. Charles W. Clark from the Joint Quantum Institute and NIST in Maryland. Without their great ideas and critical thinking, the work described in Chapter 3 would have been impossible.

I am also very thankful to Prof. David Weiss, as well as Aaron Reinhard, Jean-Felix Riou and Laura Zundel from his group. They did the self-trapping experiment that is described in Chapter 4 while we did the theoretical counterpart. After a lot of discussions in Skype meetings and hundreds of emails back and forth, we finally brought forward a new mechanism of self-trapping.

I also owe special gratitude to everyone including former members in the group for the beneficial discussions, Javier Von Stecher (Seagate), Michael Foss-Feig (JQI), Chester Rubbo (Cedar-Crestone), Kaden Hazzard (Rice university), Salvatore R. Manmana (University of Göttingen), Andrew Koller, Bihui Zhu, and all the new members in the group. Especially, I want to thank Salvatore R. Manmana for his help on DMRG calculations in this thesis. Also, thanks for the useful discussions with Murray Holland, Dana Anderson, Jinx Cooper, Dominic Meiser and Ryan Wilson.

At last, I owe my deepest thanks to my family — my grandmother, my parents, my sister, my son, and my husband. My parents are helping me by taking care of my son when I am working on my thesis. Without their support, the complete of this thesis would not have been possible.

Contents

Chapter

Appendix

Tables

Table

Figures

Figure

Chapter 1

Optical lattices

An optical lattice is created by the interference of counter-propagating laser beams, which give rise to a spatially periodic intensity-pattern. The intensity pattern generates a potential for neutral atoms via the a.c. Stark shift of the atomic energy levels. Ultracold atoms in an optical lattice are analogous to valence electrons in a solid crystal, where the optical lattice potential mimics the crystal lattice in a solid, and the atoms loaded in the lattice mimic the valence electrons. In recent years, optical lattices have been widely used as a platform for studying various problems in solid state physics [1].

In contrast to solid-state materials where impurities and structural defects are inevitable, optical lattices are rigid, free of defects, and fully controllable. The two important parameters that characterize an optical lattice are the depth of the lattice potential wells, V_0, and the lattice constant, a. The depth of the lattice can be tuned by changing the intensity of the laser, while the lattice constant can be tuned by changing the wavelength of the laser or by changing the relative angle between the two laser beams. By interfering laser beams in different ways, atoms can be confined in different types of geometries [2, 3]. By controlling the intensity of the trapping lasers, the dimensionality of the system can be varied from 3D to 0D [4, 5, 6, 7]. All these features make optical lattices a versatile arena for the investigation of nonlinear phenomena, nonequilibrium dynamics, quantum phase transitions, quantum information, and so on [1, 8].

In this chapter, we introduce the basic theory of optical lattices and discuss the single-particle physics of atoms in such a periodic potential. We follow with a brief introduction to the

Bose-Hubbard model.

1.1 Light-matter interactions

Light-matter interactions are what generate the optical lattice potential. In the dipole approximation, the light-matter Hamiltonian is given by [9],

$$H_{\text{dip}} = -\vec{d} \cdot \vec{E}, \tag{1.1}$$

where $\vec{d}$ is the dipole moment of the atom, and $\vec{E}$ is the electric field.

This dipole interaction can be considerably simplified if the external field is weak and nearly on resonance with an atomic transition. In this case, only the ground state and the near-resonance excited level have appreciable probability of occupation, and thus the complicated multilevel atomic system can be treated as a two level atom with states $|g\rangle$ and $|e\rangle$.

We denote the energy difference between the $|e\rangle$ and $|g\rangle$ states as $\hbar\omega_a$, the laser frequency as ω_o, and the detuning of the laser from the atomic transition as $\delta = \omega_o - \omega_a$. If both the atom and the laser field are treated quantum mechanically, $\vec{E}$ can be replaced by,

$$\vec{E} = \vec{e}\sqrt{\frac{\hbar\omega_o}{2\epsilon}}\left[\Xi(\vec{x})\hat{a} + \Xi^*(\vec{x})\hat{a}^\dagger\right], \tag{1.2}$$

with $\vec{e}$ the unit polarization vector of the field, and $\Xi(\vec{x})$ the field mode evaluated at the atomic position $\vec{x}$ (for example, for a 1D optical lattice potential, $\Xi(x) = \frac{2}{\sqrt{V}}\cos(kx)$). $\hat{a}$ is the annihilation operator of photons.

The dipole moment can be written in matrix form as,

$$\hat{e} \cdot \vec{d} = \mu_{ge}|g\rangle\langle e| + \mu_{eg}|e\rangle\langle g|, \tag{1.3}$$

with $\mu_{eg} = \vec{e} \cdot \langle e|\vec{d}|g\rangle \equiv \mu$. The total Hamiltonian of the system can thus be written as,

$$H = \frac{\hbar\omega_a}{2}\left(\hat{a}_e^\dagger\hat{a}_e - \hat{a}_g^\dagger\hat{a}_g\right) + \hbar\omega_o\left(\hat{a}^\dagger\hat{a} + \frac{1}{2}\right) + \sqrt{\frac{\hbar\omega_o}{2\epsilon_0}}\left[\Xi(\vec{x})\hat{a} + \Xi^*(\vec{x})\hat{a}^\dagger\right]\left(\mu|e\rangle\langle g| + \mu^*|g\rangle\langle e|\right), \tag{1.4}$$

where $\hat{a}_g$ and $\hat{a}_e$ are, respectively, the atomic annihilation operators of states $|g\rangle$ and $|e\rangle$.

When δ is much smaller than the laser frequency, $|\delta| \ll \omega_o$, the rapidly oscillating terms, $\hat{a}|g\rangle\langle e|$ and $\hat{a}^\dagger|e\rangle\langle g|$ can be neglected, i.e., we use the rotating-wave approximation. Now only the near-resonant processes need to be considered. In the rotating frame of the laser and by treating the laser field classically, the Hamiltonian can then be reduced to

$$H \approx -\frac{\hbar\delta}{2}\left(\hat{a}_e^\dagger\hat{a}_e - \hat{a}_g^\dagger\hat{a}_g\right) + \frac{\hbar\Omega(\vec{x})}{2}a_e^\dagger a_g + \frac{\hbar\Omega^*(\vec{x})}{2}a_g^\dagger a_e, \tag{1.5}$$

where $\Omega(\vec{x})$ is the Rabi frequency given by $\hbar\Omega(\vec{x}) = -2\sqrt{\frac{\hbar\omega_o\langle N\rangle}{2\epsilon_0}}\Xi(\vec{x})\mu$ ($\langle N\rangle = \langle\hat{a}^\dagger\hat{a}\rangle$).

$|\Omega(x)|^2$ is proportional to the laser intensity $I(\vec{x}) = \hbar\omega_o c\langle N\rangle|\Xi(\vec{x})|^2$, and

$$\hbar^2|\Omega(\vec{x})|^2 = \frac{2I(\vec{x})}{\epsilon_0 c}|\mu|^2. \tag{1.6}$$

1.1.1 AC-Stark shift

If the detuning is large compared to the Rabi frequency, i.e., $|\delta| \gg \Omega$, the atom-laser interaction gives rise to energy shifts in states $|g\rangle$ and $|e\rangle$. Using second-order perturbation theory, the energy shifts are

$$\Delta E = \pm\hbar\frac{|\Omega(\vec{x})|^2}{4\delta}, \tag{1.7}$$

with the plus sign for the $|g\rangle$ state and the minus sign for the $|e\rangle$ state. The ac-Stark energy shift of the atoms, $\hbar\frac{|\Omega(\vec{x})|^2}{4\delta}$, gives rise to the optical lattice potential in the ground state. The sign of the potential depends on the sign of the detuning. See Fig.1.1.

When $\delta > 0$ (the laser is blue detuned), the dipole interaction repels atoms out of the field, and the potential minima correspond to the places with minimum intensity. In contrast, when $\delta < 0$ (the laser is red detuned), the dipole interaction attracts atoms into the light field, and the potential minima are therefore found at positions with maximum laser intensity. Therefore, atoms accumulate at the bright parts in a red-detuned lattice and at the dark parts in a blue-detuned lattice.

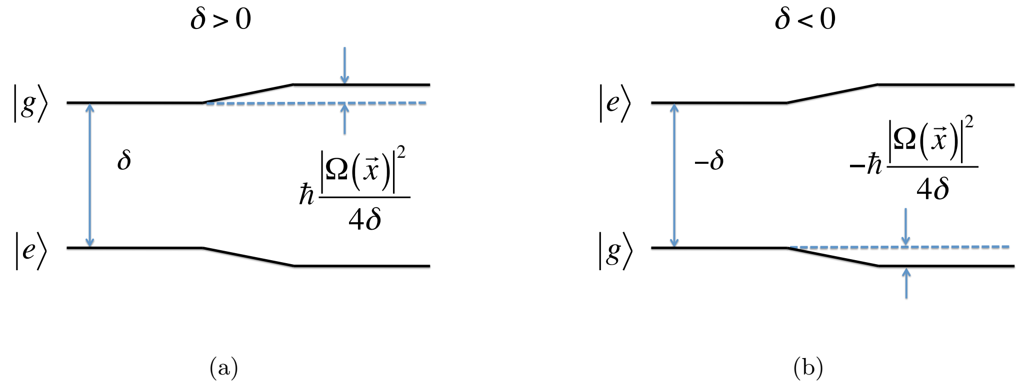

Figure 1.1: AC Stark shift induced by the atom-laser interaction. The energy shifts are $\hbar\frac{|\Omega(\vec{x})|^2}{4\delta}$ for the $|g\rangle$ state (and $-\hbar\frac{|\Omega(\vec{x})|^2}{4\delta}$ for the $|e\rangle$ state). When $\delta > 0$ (the laser is blue detuned), the minima of the lattice potential correspond to the places with minimum laser intensity. In contrast, when $\delta < 0$ (the laser is red detuned), the minima of the lattice potential correspond to the place with maximum laser intensity.

1.1.2 Dissipative interactions

In real atoms, besides the atomic transitions induced by the laser, atoms in the excited states also spontaneously emit photons and decay to the ground state. This process destroys the internal coherence between the $|g\rangle$ and $|e\rangle$ states of the atoms. This effect can be taken into account phenomenologically by attributing to the excited state a complex energy. Denoting the spontaneous-decay rate of the excited state into the ground state as Γ, when $\delta \gg \Gamma$ the energy of the perturbed ground state becomes a complex quantity that can be written as [10, 11],

$$
\begin{aligned}
E &= \frac{\hbar}{4}\frac{|\Omega(\vec{x})|^2}{\delta - i\Gamma} = V(\vec{x}) + i\Gamma_{sc}(\vec{x}), && (1.8)\\
V(\vec{x}) &= \frac{\hbar}{4}\frac{|\Omega(\vec{x})|^2\delta}{\delta^2+\Gamma^2} \approx \hbar\frac{|\Omega(\vec{x})|^2}{4\delta}, && (1.9)\\
\Gamma_{sc} &= \frac{\hbar}{4}\frac{|\Omega(\vec{x})|^2\Gamma}{\delta^2+\Gamma^2} \approx \hbar\frac{|\Omega(\vec{x})|^2\Gamma}{4\delta^2}. && (1.10)
\end{aligned}
$$

The real part of the energy corresponds to the optical potential.

The damping rate Γ can be determined from the theory of spontaneous emission as [10]

$$\Gamma = \frac{\omega_0^3}{3\pi\epsilon_0\hbar c^3}|\langle e|\mu|g\rangle|^2. \tag{1.11}$$

The general expressions for the dipole potential and the scattering rate can be rewritten in terms of Γ and $I(\vec{x})$,

$$
\begin{aligned}
V(\vec{x}) &= \frac{3\pi c^2}{2\omega_0^3}\frac{\Gamma}{\delta}I(\vec{x}). && (1.12)\\
\Gamma_{sc}(\vec{x}) &= \frac{3\pi c^2}{2\hbar\omega_0^3}\left(\frac{\Gamma}{\delta}\right)^2 I(\vec{x}). && (1.13)
\end{aligned}
$$

The dipole potential scales as I/δ, whereas the scattering rate scales as I/δ^2. Therefore optical dipole traps usually use large detunings and high intensities to keep the scattering rate as low as possible at a certain potential depth [10].

1.1.3 Gaussian beams

A typical laser beam has a Gaussian intensity-profile. For example, the intensity of the laser propagating along the z direction has the form,

$$I(r,z) = \frac{2P}{\pi w^2(z)} \exp[-2r^2/w^2(z)], \tag{1.14}$$

where P is the total power of the laser beam, $r = \sqrt{x^2+y^2}$ is the radial distance from the beam's center, and $w(z)$ is the $1/e^2$ radius. For a beam with wavelength λ, the variation of the spot size at point z is given by $w(z) = w_0\sqrt{1+z^2/z_R^2}$, where w_0 is called the beam waist, and $z_R = \pi w_0^2/\lambda$ is called the Rayleigh length. Around the intensity maximum, the ac-Stark shift for a red-detuned laser beam is approximated by the harmonic potential

$$V_{\mathrm{dip}}(r,z) \approx -V_0[1 - 2(r/w_0)^2 - (z/z_R)^2]. \tag{1.15}$$

Here V_0 is the trap depth, and it is linearly proportional to the laser power. V_0 typically ranges from a few kHz up to 1 MHz, i.e., from the nanokelvin to the microkelvin regime. The harmonic confinement is characterized by radial (ω_r) and axial (ω_z) trapping frequencies, with $\omega_r = \sqrt{4V_0/Mw_0^2}$ and $\omega_z = \sqrt{2V_0/Mz_R^2}$, where M is the mass of the atom.

1.1.4 1D, 2D, and 3D optical lattices

The simplest lattice-potential is a one-dimensional lattice formed by two counter-propagating beams. For a Gaussian beam, the typical value of z_R is significantly larger than w_0, so around the intensity maximum, the trapping potential has the simplified form of

$$V_{\mathrm{dip}}(r,z) \approx -V_0 e^{-2r^2/w_0^2} \sin^2(kz), \tag{1.16}$$

where $k = \frac{2\pi}{\lambda}$ is the wave vector of the laser light, and V_0 is the maximum depth of the lattice potential. The 1D optical potential generates an array of disk-shaped potentials (pancakes).

If two additional counter-propagating beams are added perpendicularly to the original 1D lattice (the polarization vectors of the second-set of beams are also orthogonal to the first set of

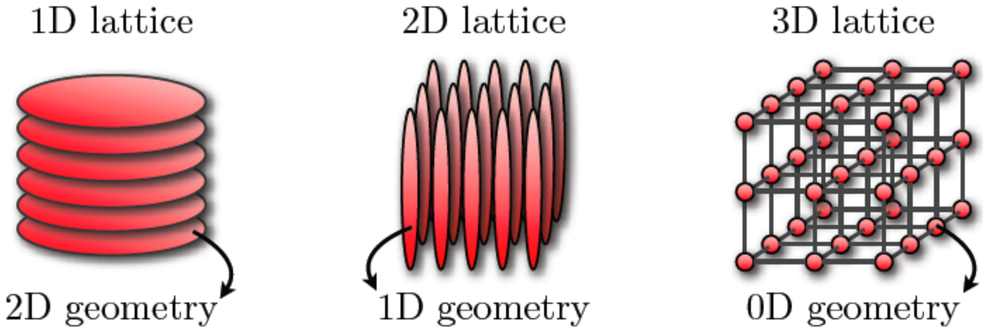

Figure 1.2: Optical lattice in different dimensions. Courtesy of Michael Foss-Feig.

beams), the resulting trapping potential has the form,

$$\begin{aligned} V_{\text{dip}}(x,y,z) &\approx -V_x e^{-2(y^2+z^2)/w_x^2}\sin^2(kx) - V_y e^{-2(x^2+z^2)/w_y^2}\sin^2(ky) \\ &\approx -V_x\left[1-2\frac{y^2}{w_x^2}-2\frac{z^2}{w_x^2}\right]\sin^2(kx) - V_y\left[1-2\frac{x^2}{w_y^2}-2\frac{z^2}{w_y^2}\right]\sin^2(ky), \end{aligned} \tag{1.17}$$

where w_x and w_y are, respectively, the beam waists along x and y. The above 2D optical potential generates an array of elongated 1D traps (tubes).

If a third pair of counter-propagating beams are added to the 2D optical lattice, the resulting trapping-potential has the form in the case where any additional potential from the Gaussian shape of the laser intensity is neglected

$$V_{\text{dip}}(x,y,z) \approx -V_x\sin^2(kx) - V_y\sin^2(ky) - V_z\sin^2(kz). \tag{1.18}$$

Schematic configurations of optical lattices in 1D, 2D, and 3D are shown in Fig. 1.2.

1.2 Single particle properties

1.2.1 Band structure

Considering a single atom in an 1D optical lattice potential, the single-particle Hamiltonian is

$$H_0 = \frac{p^2}{2M} + V_0 \sin^2(kx). \tag{1.19}$$

For convenience, the depth of the lattice potential V_0 is generally specified by the recoil energy $E_R = \hbar^2 k^2/2M$, which is the kinetic energy gained by an atom with M by absorbing one photon. The typical value of a lattice depth ranges from several recoil up to hundreds.

From condensed matter theory, it is known that in such a periodic potential, the eigenstates are the so-called Bloch functions $\phi_q^{(n)}(x)$ [12], where

$$H_0 \phi_q^{(n)}(x) = E_q^{(n)} \phi_q^{(n)}(x). \tag{1.20}$$

Bloch functions have the form of a plane wave e^{iqx} times a periodic function $u_q^{(n)}(x)$ with $u_q^{(n)}(x) = u_q^{(n)}(x+a)$. Here a is the lattice spacing and q is a quantum number that characterizes the translational symmetry of the periodic potential. $\hbar q$ is called quasimomentum, and it plays a similar role in a periodic potential as momentum does in free space. Each Bloch function has a specific value of q and eigenvalue $E_q^{(n)}$, where n is an integer, called the band index. If $\phi_q^{(n)}(x)$ is an eigenfunction of H_0, so is $\phi_{q+G_m}^{(n)}(x)$, where $G_m = m\frac{2\pi}{a}$ is called the reciprocal lattice vector with m an arbitrary integer. In general, the wave vector q is confined to the first Brillouin zone, i.e., $q \in (-\pi/a, \pi/a]$. If we plot $E_q^{(n)}$ as a function of q, we will get a series of smooth curves from $q \in (-\pi/a, \pi/a]$. Each curve corresponds to a specific band with band index n. Larger n corresponds to higher band with larger energy.

In the case of a sinusoidal potential, the Bloch functions $\phi_q^{(n)}(x)$ and their eigenvalues $E_q^{(n)}$ can be solved analytically. The Bloch functions $\phi_q^{(n)}(x)$ can be expressed in terms of Mathieu functions, and the eigenvalues $E_q^{(n)}$ be written in terms of Mathieu characteristic values. Fig. 1.3 shows the band structure of an optical lattice for different lattice depths. For $V_0 = 0$, particles

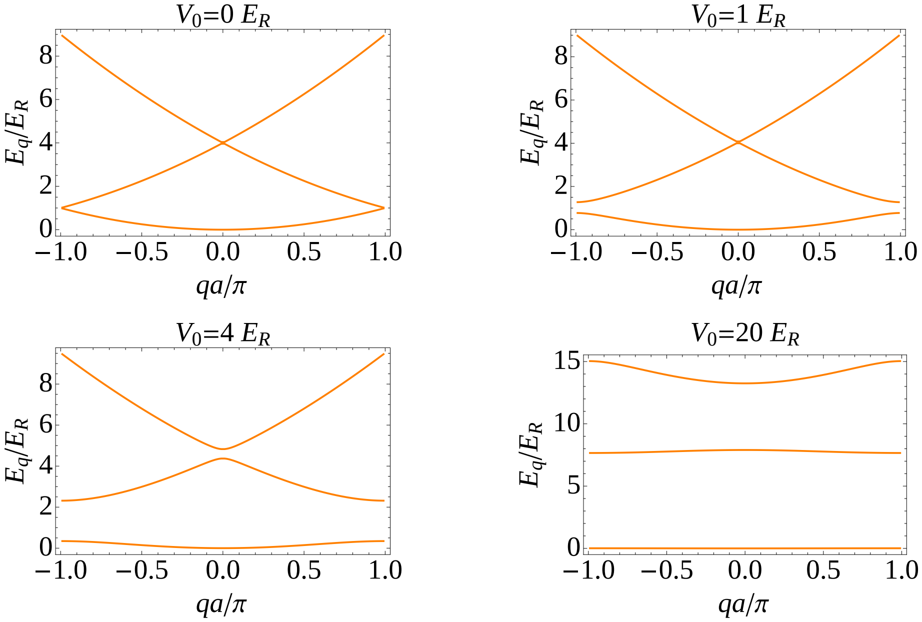

Figure 1.3: Band structure of an optical lattice with different lattice depths.

move in free space, and the spectrum is quadratic in q. As the potential depth is increased, the band structure appears. For small V_0, a gap opens at the edge of the first Brillouin zone. As the depth increases, the band gap enlarges, the bandwidth shrinks, and more and more gaps open at the edge of the first Brillouin zone. For very deep lattices, the spectrum is almost degenerate in q and exhibits a dependence on n similar to the one of a particle in a harmonic trap.

1.2.2 Wannier functions

In many cases, it is more convenient to use another complete set of orthonormal wave functions, which are called Wannier functions, to describe atoms in a optical lattice. As Fourier transforms of Bloch functions, Wannier functions constitute an equivalent basis to describe the periodic system, i.e.,

$$w_n(x - x_i) = \frac{1}{\sqrt{N}} \sum_q e^{-iqx_i} \phi_q^{(n)}(x). \tag{1.21}$$

Replacing $\phi_q^{(n)}(x)$ with $\frac{1}{\sqrt{N}} \sum_i e^{iqx_i} w_n(x - x_i)$ in equation (1.20) and using the orthonormal

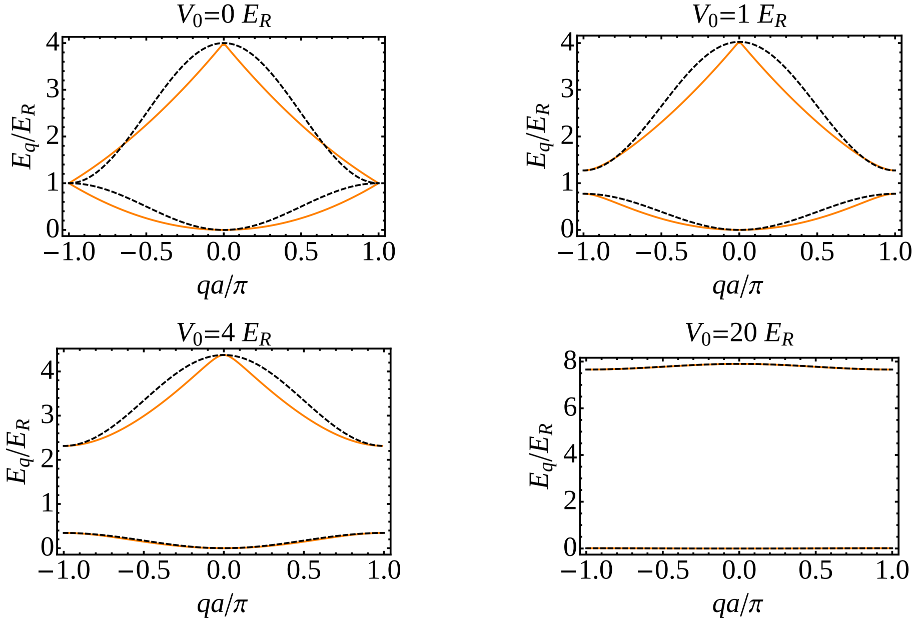

Figure 1.4: Band structure: orange curves—exact solution from Mathieu equation, black-dashed curves—from the tight-binding approximation.

properties of Wannier functions, we get

$$\begin{aligned} E_q^{(n)} &= \sum_i e^{iqx_i} \int dx\ w_n^*(x) H_0 w_n(x - x_i) \\ &\approx \int dx\ w_n^*(x) H_0 w_n(x) + e^{iqa} \int dx\ w_n^*(x) H_0 w_n(x-a) + e^{-iqa} \int dx\ w_n^*(x) H_0 w_n(x+a) + \cdots \\ &= \epsilon_n - 2J^{(n)} \cos(qa) + \cdots . \end{aligned} \tag{1.22}$$

The last line is called the tight-binding approximation.[1] The tight-binding approximation is widely used for atoms in deep lattices.

As we mentioned in the last section, the band structure of an atom in a sinusoidal potential can be solved exactly. Therefore, we can get the value of J and ϵ_n in Eqn. (1.22) from the bandwidths and the band gaps of the exact band-structure. On the other hand, the validity of the tight-binding approximation can be checked by comparing the exact band-structure with the

---

[1] The terminology of "tight binding" was first used in condensed matter physics for calculating the electronic band structure of tightly bound electrons in solids. When an electron is tightly bound to the atom to which it belongs and the effect of surrounding atoms on the electrons is limited, the Wannier functions are replaced by atomic orbitals of the free atom to which the electron belongs. In the tight-binding approximation, usually only the on-site energy E_n and first order correction due to the nearest-neighboring tunneling are included, other terms are neglected.

band-structure in the tight-binding approximation, as shown in Fig. 1.4. We can see that the tight-binding approximation is a good approximation when the lattice depth is deep enough. Provided atoms only occupy the lowest band, the tight-biding approximation is good for a lattice depth larger than $4E_R$.

1.2.3 External potentials

The tight-binding approximation is commonly used to solve the problem of a particle in a periodic potential when an external field is also applied.

When the lattice is deep enough and the external perturbation is not strong enough to induce inter-band transitions, one may only expand the moving-particle wave function in the Wannier bases in the first band, i.e.,

$$\psi(x,t) = \sum_i z_i(t) w_0(x - x_i), \tag{1.23}$$

where i is the lattice site index, and x_i is the position of the i^{th} lattice-site. The Schrödinger equation for a particle that moves in the periodic potential of a 1D lattice V_{lat} plus a perturbative external-potential $V_{\text{ext}}(x)$ is

$$i\hbar \frac{\partial}{\partial t}\psi(x,t) = \left[-\frac{\hbar^2}{2M}\frac{\partial^2}{\partial x^2} + V_{\text{lat}}(x)\right]\psi(t) + V_{\text{ext}}(x)\psi(x,t). \tag{1.24}$$

By substituting Eqn. (1.23) in the Schrödinger equation, we get the following equations of motion,

$$i\hbar \frac{\partial}{\partial t} z_i(t) = -\sum_j J_{ij} z_j(t) + V_{ij}(x) z_j(t), \tag{1.25}$$

where

$$\begin{aligned} J_{ij} &= -\int dx\ w_0^*(x - x_i)\left[-\frac{\hbar^2}{2M}\frac{\partial^2}{\partial x^2} + V_{lat}(x)\right] w_0(x - x_j), && (1.26) \\ V_{ij} &= \int dx\ w_0^*(x - x_i) V_{\text{ext}}(x) w_0(x - x_j). && (1.27) \end{aligned}$$

If the external perturbation is a slowly varying function, it can be assumed constant inside each individual lattice-site. And the Wannier function $w_0(x - x_i)$ can be replaced with the delta function $\delta(x - x_i)$, and then $V_{ij} = V_{\rm ext}(x_i)\delta_{ij}$. Moreover, since the lattice is deep enough, only the tunneling to nearest-neighbors (for $j = i \pm 1$) is relevant. The equations of motion reduce to

$$i\hbar\frac{\partial}{\partial t}z_i(t) = -J\left[z_{i-1}(t) + z_{i+1}(t)\right] + \epsilon_0 z_i(t) + V_i z_i(t), \tag{1.28}$$

with

$$\begin{aligned} J &= -\int dx\ w_0^*(x)\left[-\frac{\hbar^2}{2m}\frac{\partial^2}{\partial x^2} + V_{lat}(x)\right] w_0(x+a), && (1.29)\\ \epsilon_0 &= \int dx\ w_0^*(x)\left[-\frac{\hbar^2}{2m}\frac{\partial^2}{\partial x^2} + V_{lat}(x)\right] w_0(x), && (1.30)\\ V_i &= \int dx\ w_0^*(x - x_i)V_{\rm ext}(x)w_0(x - x_i) \approx V_{\rm ext}(x_i). && (1.31) \end{aligned}$$

Here J is the tunneling matrix element between nearest-neighboring sites, ϵ_0 is the on-site energy-shift, and V_i is the external potential at lattice-site i. Equation (1.28) is called the discrete Schrödinger equation (DSE).

1.2.4 Semiclassical dynamics

The wave-packet solutions of the Schrödinger equation behave like classical particles obeying the classical Hamiltonian equations,

$$\dot{x} = \frac{\partial H}{\partial p}, \quad \dot{p} = -\frac{\partial H}{\partial x}. \tag{1.32}$$

Bloch's theorem introduces a wave-vector q that turns out to play the same role in the general problem of motion in a periodic potential as the momentum $p/\hbar$ does in free space. So the semiclassical equations [2] of a particle with momentum $\hbar q$ in the first band can be written as [12, 13],

$$\dot{x} = v^{(0)}(q) = \frac{1}{\hbar}\frac{dE_q^{(0)}}{dq}, \quad \dot{p} = \hbar\dot{q} = -\frac{dV_{\rm ext}(x)}{dx}. \tag{1.33}$$

The first equation simply states that the velocity of a semiclassical atom is the group-velocity of the underlying wave-packet. The second equation states that the rate-of-change of an atom's

---

[2] The semiclassical model is a partial classical limit in the sense that the externally applied fields are treated classically, but the periodic potential is not [12].

quasi-momentum is given only by the external force, but not by the periodic field of the lattice. In sum, the semiclassical equations-of-motion describe how, in the absence of collisions and in the presence of an external potential, the position x and the wave vector q of a particle evolve entirely in terms of the band structure of the lattice.

If we compare the acceleration predicted by the model with the conventional Newtonian equation, $M\ddot{x} = -dV_{\text{ext}}(x)/dx$, we can associate an effective-mass m^* induced by the presence of the lattice. This is given by,

$$\frac{1}{m^*} = \frac{1}{\hbar^2}\frac{d^2}{dq^2}E_q^{(0)} = \frac{\hbar^2}{2Ja^2\cos(qa)}. \tag{1.34}$$

Close to the bottom of the band, $q \to 0$, $m^* \to \frac{\hbar^2}{2Ja^2}$. Since the tunneling decreases exponentially with the lattice depth [11], the effective mass grows exponentially. In the presence of interactions, the large effective-mass manifests itself in a substantial enhancement of the interaction to kinetic energy ratio, in comparison to the free particle case. Therefore atoms in optical lattices can easily reach the strongly interacting regime, in which the interaction energy of the atoms at a given density dominates over their characteristic quantum kinetic-energy.

1.3 Bose-Hubbard model

The simplest nontrivial model that gives an approximate description of the physics of interacting bosons in a lattice is the Bose-Hubbard model [14]. It is closely related to the Hubbard model [15], which originated in solid-state physics as an approximate model to describe the motion of electrons in a crystal lattice. The Bose-Hubbard Hamiltonian (for bosons) exhibits a quantum phase-transition from a superfluid state to a Mott-insulator state. Following the proposal by Jaksch *et al* in 1998 [16], the Bose-Hubbard model has been realized experimentally using ultracold atomic systems in various dimensions [7, 17, 18, 19].

The Bose-Hubbard model can be derived using second quantization which describes interacting atoms in an external trapping-potential. When the lattice is deep enough, and the external perturbation is too weak to induce inter-band transitions, in the language of second quantization, the field operator can be expanded in terms of Wannier orbitals in the first band and their associated annihilation-operators, i.e.,

$$\hat{\Psi} = \sum_i \hat{a}_i w_0(\vec{x} - \vec{x}_i), \tag{1.35}$$

where i is the lattice site index, and $\vec{x}_i$ is the position of the i^{th} lattice site. The Bose-Hubbard model can be derived by substituting Eqn. (1.35)

$$\begin{aligned} \hat{H} &= \int d\vec{x}\ \hat{\Psi}^\dagger(\vec{x}) \left[-\frac{\hbar^2}{2m}\nabla^2 + V_{\text{lat}}(\vec{x}) \right] \hat{\Psi}(\vec{x}) + \int d\vec{x}\ V_{\text{ext}}(\vec{x})\hat{\Psi}^\dagger(\vec{x})\hat{\Psi}(\vec{x}) \\ &+ \frac{1}{2}\int d\vec{x}d\vec{x}'\ \hat{\Psi}^\dagger(\vec{x})\hat{\Psi}^\dagger(\vec{x}')U_{\text{int}}(\vec{x}-\vec{x}')\hat{\Psi}(\vec{x})\hat{\Psi}(\vec{x}') - \int d\vec{x}\ \mu(\vec{x})\hat{\Psi}^\dagger(\vec{x})\hat{\Psi}(\vec{x}). \end{aligned} \tag{1.36}$$

As mentioned in the last section, $V_{\text{lat}}(\vec{x})$ is the periodic lattice potential, $V_{\text{ext}}(\vec{x})$ denotes any additional slowly varying external-potential, and μ is the chemical potential. $U_{\text{int}}(\vec{x} - \vec{x}')$ is the two-body interatomic potential. When the atomic distance is much larger than the effective extent of the U_{int}, the atomic interaction due to s-wave scattering can be well approximated by a contact interaction, i.e.,

$$U_{\text{int}}(\vec{x} - \vec{x}') \approx g\delta(\vec{x} - \vec{x}'), \quad g = \frac{4\pi a_s \hbar^2}{M}, \tag{1.37}$$

where a_s is the s-wave scattering length.

In the tight-binding approximation, we get the Hamiltonian in the second quantization form

$$H = -J\sum_{\langle i,j\rangle} \hat{a}_i^\dagger \hat{a}_j + \sum_i (V_i - \mu)\hat{a}_i^\dagger \hat{a}_i + \frac{U}{2}\sum_i \hat{a}_i^\dagger \hat{a}_i^\dagger \hat{a}_i \hat{a}_i, \tag{1.38}$$

with J and V_i as in Equation (1.29, 1.31) and

$$U = \frac{4\pi a_s \hbar^2}{M}\int dx |w_0(x)|^4. \tag{1.39}$$

The first term in the Hamiltonian proportional to J is a measure of the kinetic energy of the system. Next-to-nearest neighbor tunneling amplitudes are typically two orders of magnitude smaller than nearest-neighbor ones, and to a good approximation they can be neglected [11]. The second term in the Hamiltonian takes into account the energy offset between lattice sites due to a slow-varying external potential $V_{\text{ext}}(x)$, and chemical potential μ. The third term accounts for interatomic interactions. The parameter U measures the strength of the repulsion between two

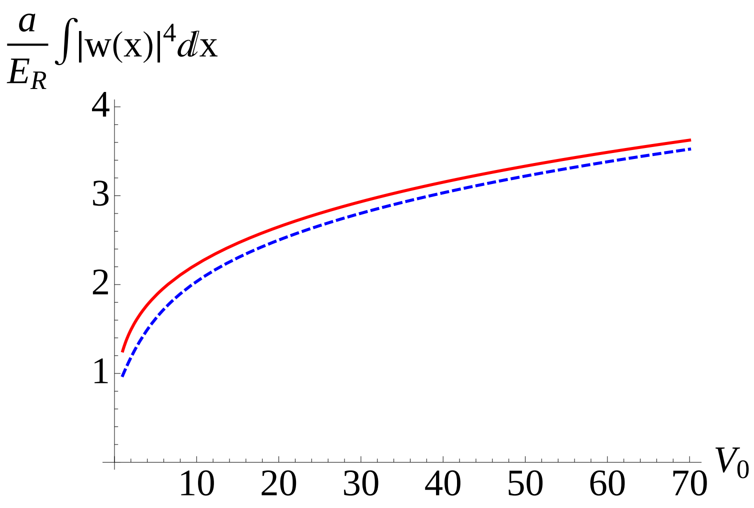

Figure 1.5: Comparisons of $\int dx|w(x)|^4$, for the red solid line, $w(x)$ is approximated by the Gaussian function $\psi_0(x)$, and for the blue dashed line $w(x)$ is calculated numerically by its definition.

atoms at the same lattice-site. While J decreases exponentially with lattice depth V_0, U increases as a power law, $V_0^{D/4}$, where D is the dimensionality of the lattice.

The integral of U is not sensitive to the oscillatory tails of the Wannier orbitals, therefore when calculating $\int dx|w_0(x)|^4$, the Wannier functions can be approximated by the eigenfunctions of the harmonic trap, i.e., $\psi_n(x) = \frac{1}{\sqrt{2^n n!}}\left(\frac{x_0^2}{\pi}\right)^{1/4} e^{-\frac{x^2}{2x_0^2}} H_n\left(\frac{x}{x_0}\right)$ with $x_0 = \sqrt{\frac{\hbar}{M\omega_x}}$ the characteristic length of an harmonic potential. In Fig. (1.5), we compare the numerical values between $\int dx\ |w_0(x)|^4$ and $\int dx\ |\psi_0(x)|^4$. We can see that these two curves are very close to each other, which means that Gaussian functions are good approximations of Wannier orbitals in estimating U.

1.3.1 The superfluid to Mott-insulator transition

Here we skip the details about the phase diagram of the Bose-Hubbard model, but only introduce the superfluid and Mott-insulator states, since we will use them a lot in this thesis.

At zero temperature, the physics described by the Bose-Hubbard Hamiltonian can be divided into two different regimes in the homogeneous case when $V_i = 0$. The first regime is the kinetic-energy-dominated regime, when tunneling overwhelms the repulsion, and the atoms exhibit superfluid properties. Another regime is the interaction-dominated regime when J is much smaller than U, and the atoms behave like an insulator, the so-called Mott-insulator. The transition between the two regimes is a consequence of the competition between the kinetic energy, which tries to delocalize the particles, and the interaction energy, which tries to localize them and penalizes multiple-occupied lattice sites.

In the superfluid regime, the kinetic energy term dominates the Hamiltonian, and the system behaves as a weakly interacting Bose gas. Quantum fluctuations can be neglected, and the system can be described by a macroscopic wave function. For a translationally invariant lattice, the ground state consists of all atoms in the zero-quasi-momentum mode. In this case,

$$|\Psi_{SF}\rangle = \frac{1}{\sqrt{N!}} \left(\hat{b}_0^\dagger\right)^N |0\rangle, \tag{1.40}$$

where N is the total number of atoms, $|0\rangle$ is the state of vacuum, and $\hat{b}_q^\dagger = \frac{1}{\sqrt{L}} \sum_j \hat{a}_j^\dagger e^{iqx_j}$ is the creation operator of an atom with quasi-momentum q, and L is the total number of lattice sites.

With increasing interatomic interactions, the average kinetic-energy required for an atom to hop from one site to the next becomes insufficient to overcome the interaction-energy cost. Atoms tend to get localized at individual lattice-sites, and fluctuations of the atom-number at a given lattice-site are penalized. In this strongly interacting limit, if the number of atoms is commensurate with the number of lattice sites, the ground state of the system enters the Mott-insulator phase characterized by localized atomic wave functions and a fixed number of atoms per site, i.e.,

$$|\Psi_{MI}\rangle = \prod_j \frac{1}{\sqrt{n!}} \left(\hat{a}_j^\dagger\right)^n |0\rangle, \tag{1.41}$$

where $n = N/L$ is the filling factor or mean number of particles per site. We have assumed that the number of particles is commensurate with lattice sites, i.e., that n is an integer.

For fermionic atoms with two possible spin-states $|\uparrow\rangle$, $|\downarrow\rangle$ confined to the lowest band in 1D optical-lattices, the system can be described by the single-band Hubbard model [1],

$$H = -J \sum_{i,\sigma} \left(\hat{c}_{i,\sigma}^\dagger \hat{c}_{i+1,\sigma} + \hat{c}_{i+1,\sigma}^\dagger \hat{c}_{i,\sigma}\right) + U \sum_i \hat{n}_{i,\uparrow} \hat{n}_{i,\downarrow} + \sum_{i,\sigma} V_i \hat{n}_{i,\sigma}. \tag{1.42}$$

Similar to the Bose-Hubbard model, the Hubbard model of fermonic atoms in an optical lattice describes a quantum phase-transition from a superfluid state to a fermionic Mott-insulator state [20].

For spin-polarized fermionic atoms, because of the Pauli-exclusion principle, the s-wave interaction between two atoms is zero, therefore the low-energy physics is described by the Hamiltonian of free atoms moving in an optical lattice in the presence of an additional external potential,

$$H = -J \sum_{i} \left(\hat{c}_i^{\dagger} \hat{c}_{i+1} + \hat{c}_{i+1}^{\dagger} \hat{c}_i \right) + \sum_{i} V_i \hat{n}_i. \tag{1.43}$$

In the case of $V_i = 0$, the atomic eigenstates are the Bloch states. As the Puali principle does not allow two fermionic particles to occupy the same Bloch state, atoms occupy the Bloch states one by one, starting from the bottom of the lowest-energy band to the top. The full occupation of the lowest band and the energy gap to the empty second band characterizes the fermionic band-insulating state.

Chapter 2

Detection of correlations

2.1 Introduction

Correlation functions are a natural framework for characterizing quantum states. This chapter starts with a general discussion about the basic concepts of coherency, interference, and correlation. We then introduce the amplitude interferometry such as Young's double slit experiment, and Hanbury Brown and Twiss (HBT) intensity-interferometry. Next the investigation of quantum correlations and their detection in ultracold gases in an optical lattice is discussed. For example, absorption images after time of flight (TOF) provide a useful tool in determining correlation functions. The reason is that after the atoms are released from the trap and allowed to expand until the size of the cloud becomes much larger than the original separation between the atoms, the momentum distribution of the trapped gas gets mapped into the density distribution in TOF images after the expansion. The latter displays an interference pattern in the superfluid regime, and disappears in the Mott-insulator phase. Moreover, it has been pointed out that measurements of shotnoise in TOF images after the expansion (the results of which are different from one experimental run to another) contain information about the quantum statistics of the particles and can help to further characterize the quantum phases. These ideas were first theoretically developed by Altman et al. in 2004 [21].

2.2 Coherence, interference and correlations

2.2.1 Coherence

A Bose-Einstein condensate (BEC) is a state of matter that emerges in a degenerate Bose gas, and it is usually described as a macroscopic matter-wave field. The first study of BEC goes back to nighty years ago when it was first predicted for photons by S. Bose in 1924 and for atoms by A. Einstein in 1925. The experimental realization of BEC in trapped atomic clouds [22, 23] opened up the exploration of quantum phenomena on a macroscopic scale.

In atomic BECs, most atoms occupy the same ground state, so quantum fluctuations can be neglected to a good approximation. Therefore the field operator can be replaced by a c-number, $\hat{\Psi}(\vec{x}) \to \Psi(\vec{x})$. The function $\Psi(\vec{x})$ is often called the "condensate wave function" or "order parameter", and it evolves according to the time-dependent GPE [24] as

$$i\hbar\frac{\partial\Psi}{\partial t} = -\frac{\hbar^2}{2M}\nabla^2\Psi + \left(V_{\text{ext}} + g|\Psi|^2\right)\Psi. \tag{2.1}$$

Here V_{ext} is the external potential, and $g = \frac{4\pi\hbar^2 a_s}{M}$ with M the atomic mass and a_s the scattering length.

Phase coherence is one of the most essential features exhibited by BECs. Assuming a condensate confined by a box with infinitely hard walls, the wave function vanishes at the wall, and in the interior of the box the wave function has its bulk value. The distance ξ over which the wave function arises from 0 to its bulk values can be estimated from the GP equation, since far away from the wall the wave function is governed by competitions between the kinetic energy $\sim \hbar^2/2M\xi^2$ and the interaction $\sim nU$ (U as in Eqn. (1.39)). These two energies are equal when

$$\frac{\hbar^2}{2M\xi^2} = nU, \tag{2.2}$$

or $\xi^2 = \frac{1}{8\pi n a_s}$. ξ is referred to as the coherence length. Since it describes the distance over which the wave function tends to its bulk value when subjected to a localized perturbation, it is also referred to as the healing length [24].

2.2.2 Interference

Interference is a generic property of coherent waves. One of the simplest, yet most profound, interference experiments was implemented by Thomas Young in 1803: The Young's double-slit experiment. In the double-slit setup, a monochromatic light source with wavelength λ goes through two small closely spaced holes, separated by a distance d. Two split waves interfere and form an interference pattern on the screen. The resulting interference-pattern is composed of bright bands due to constructive interference, interlaced with dark bands due to destructive interference.

A powerful generalization of Young's interferometer is the diffraction grating. A grating is an array of N regularly space lines that act as N slits. The diffracted light-signal through a grid results in a constructive interference-pattern with N^2 enhancement in intensity. This device is widely used from spectroscopy to telecommunications. For example, regular arrays of atoms in crystals provide as a natural grating for X-rays and generate a diffraction pattern known as Bragg diffraction, which are used to study the structure of crystalline solids.

In quantum mechanics, all objects have wave-like properties. For instance, electrons can be used instead of light in the Young's double-slit experiment. When a large number of electrons is accumulated, something like regular fringes begin to appear in the detecting plane. Historically, the wave nature of particles was first put forward by De Broglie in 1924 and confirmed three years later for electrons with the observation of electron diffraction independently by Clinton Davisson and George Thomson.

A revolutionary step towards the understanding of macroscopic matter-wave arose from the experimental-realization of BEC in atomic vapors. BECs along with quantum degenerate Fermi gases, have provided a new platform and scope to the subject of interferometry of matter waves. For example, interference between two BECs were observed [25], demonstrating that BECs are "laser-like" matter-waves.

In the discussion so far, interference reflects first-order correlations associated with the amplitude of two coherent waves. Interestingly, interference phenomena can also be observed with incoherent sources provided one probes the effects beyond first-order correlations. In other words, many-particle correlations can exhibit interference effects even when single-particle correlations do not. This was first discovered by Hanbury Brown and Twiss more than fifty years ago [26]. The HBT experiment shows that coherence between sources is not a prerequisite for interference effects.

The simplest picture of HBT interferometry, which illustrates the basic idea behind HBT [26], is to consider two distant point-sources of light, a and b, of the same frequency and with random phase at a distance $\vec{R}$ apart. One measures the light falling in two independent detectors, separated by a distance d, as shown in Fig. 2.1. The distance L between the source and the detector is much larger than R or d. Treating electromagnetic radiations as classical waves, the radiation field from two sources at point $\vec{r}$ is

$$\frac{A}{|\vec{r}-\vec{r}_a|}e^{ik|\vec{r}-\vec{r}_a|+i\phi_a}+\frac{B}{|\vec{r}-\vec{r}_b|}e^{ik|\vec{r}-\vec{r}_b|+i\phi_b}, \tag{2.3}$$

with ϕ_a and ϕ_b being the random and uncorrelated phases. After averaging the phases, one obtains the intensity-correlation function from two sources at a distance $\vec{R}$ apart to be

$$\langle I_1 I_2\rangle = \langle I_1\rangle\langle I_2\rangle + \frac{2}{L^2}|A^2||B^2|\cos\left[k(r_{1a}-r_{2a}-r_{1b}+r_{2b})\right], \tag{2.4}$$

where r_{1a} (r_{1b}) is the distance from source a (b) to detector D1. Same for r_{2a} (r_{2b}).

The above equation shows a signal that varies as a function of detector separation d on a characteristic length-scale $d=\lambda/\theta$, where λ is the wavelength of the light, and $\theta = R/L$ is the angular size of the sources as seen from the detectors. Thus, by varying the separation of the detectors, one learns the apparent angle between the two sources, and with a knowledge of the individual wave-vectors, the physical size of the source.

To summarize, while the double slit with a single detector is an example of amplitude interferometry, HBT interferometry is an example of intensity interferometry that measures the correlation function $\langle I_1 I_2\rangle$ of two intensities at two different detectors at a given time.

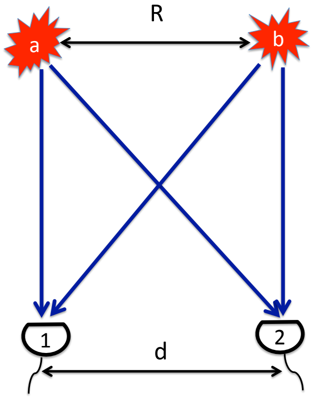

Figure 2.1: Schematic of the Hanbury-Brown and Twiss experiment, showing two independent detectors 1 and 2 that record the intensities of radiations from two sources a and b simultaneously.

2.2.3 Correlations

We now give the definition of two important correlation-functions in cold atoms and discuss their measurements and applications. The correlation functions are

$$\langle n(\vec{x})\rangle = \langle\hat{\Psi}^\dagger(\vec{x})\hat{\Psi}(\vec{x})\rangle, \text{and} \tag{2.5}$$

$$G^{(2)}(\vec{x},\vec{x}') \equiv \langle\hat{\Psi}^\dagger(\vec{x})\hat{\Psi}^\dagger(\vec{x}')\hat{\Psi}(\vec{x}')\hat{\Psi}(\vec{x})\rangle, \tag{2.6}$$

where $\hat{\Psi}(\vec{x})$ is the wave-field operator, $\langle n(\vec{x})\rangle$ is a first-order correlation-function, and $G^{(2)}(\vec{x},\vec{x}')$ is a second-order correlation- function. As we discussed above, the first-order correlation-functions can be measured by using amplitude interferometry, while $G^{(2)}(\vec{x},\vec{x}')$ can be measured by HBT interferometry. In cold atoms, both interferometries take advantage of the time-of-flight technique.

2.3 Time-of-flight technique

Consider a cloud of atoms loaded in an optical lattice. It is of interest to probe the *in situ* correlations of this system. However, imaging limitations make it difficult to resolve two lattice-sites spaced by less than one μm apart. Although recently there has been great progress in the development of high-resolution imaging techniques that could resolve single lattice-sites [27, 28, 29], until now most cold-atom experiments still probe the system by using time-of-flight images taken on the expanded atomic-cloud after turning off the lattice and other external confinement-potentials.

The expansion itself is a rather complex process. In general, interactions between particles during the expansion can generate additional noise and correlations in the system. However, since the system's density sufficiently decreases after a short time of expansion, to a good approximation, one can neglect collisional processes and assume that upon release the atoms freely evolve.

The key point behind TOF images relies on the fact that the spatial distribution after expansion reflects the momentum distribution of the atoms in the trap. There are two prerequisites for this to be true. First, the time of flight must be long enough, so that the initial size of the atom cloud in the trap can be neglected. Second, during the expansion process, interactions between atoms do not modify the initial momentum-distribution. For an atom of mass M moving with an average velocity x/t, it's characteristic momentum is $\hbar Q(x) = Mx/t$. Appendix A discusses details of the TOF images for a single particle.

We first consider a BEC released from a trapping potential. After a time of flight t, the resulting density distribution yields a three-dimensional density-distribution $n(\vec{x})$. If interactions can be neglected during the TOF, the average density-distribution is related to the in-trap quantum state via the relation [1]

$$\hat{a}(\vec{x})_{\mathrm{TOF}} \approx \left(\frac{M}{\hbar t}\right)^{3/2} \hat{a}(\vec{q})_{\mathrm{trap}}, \tag{2.7}$$

where $\vec{q}$ and $\vec{x}$ are related by the ballistic-expansion condition $\vec{x} = \frac{\hbar t}{M}\vec{q}$, and $\hat{a}(\vec{q})$ is the field operator for destroying a particle with momentum $\vec{q}$.

Now, assume that initially a BEC is trapped in a 3D simple-cubic optical-lattice. The field operator $\hat{\Psi}(\vec{r})$ can be expressed as a sum over the destruction operator $\hat{a}(\vec{R})$ of localized Wannier-states by using the expansion $\hat{\Psi}(\vec{r}) = \sum_{\vec{R}} w(\vec{r} - \vec{R})\hat{a}_{\vec{R}}$. Therefore $\hat{a}(\vec{q})_{\mathrm{trap}}$ is given by

$$\hat{a}(\vec{q})_{\mathrm{trap}} = \int e^{-i\vec{q}\cdot\vec{r}} \hat{\Psi}(\vec{r}) d^3\vec{r} = \tilde{w}(\vec{q}) \sum_{\vec{R}} e^{-i\vec{q}\cdot\vec{R}} \hat{a}_{\vec{R}}, \tag{2.8}$$

where $\tilde{w}(\vec{q})$ is the Fourier transform of the Wannier function $w(\vec{r})$. The density distribution observed in the TOF image is,

$$\hat{n}(\vec{x})_{\text{TOF}} = \left(\frac{M}{\hbar t}\right)^3 |\tilde{w}(\vec{q})|^2 \mathcal{G}(\vec{q}), \tag{2.9}$$

where the coherence properties of the many-body state are characterized by,

$$\mathcal{G}(\vec{q}) = \sum_{\vec{R},\vec{R}'} e^{i\vec{q}\cdot(\vec{R}-\vec{R}')} G^{(1)}(\vec{R},\vec{R}'), \tag{2.10}$$

which is the Fourier transform of the one-particle density matrix $G^{(1)}(\vec{R},\vec{R}') = \langle \hat{a}^\dagger_{\vec{R}} \hat{a}_{\vec{R}'} \rangle$.

Below, we compute various correlation-functions extractable from the TOF images [30].

2.3.1 Experimental evidence of superfluid to Mott-insulator phase transition

The Superfluid to Mott-insulator transition (tuned by increasing the lattice depths) has been probed in a gas of ultracold bosonic atoms by using TOF images [7].

As explained in Chapter 1, bosonic atoms in optical lattices are described by the Bose-Hubbard model, which includes nearest-neighbor tunneling and on-site atomic interactions in a lattice potential. In the superfluid regime, the ground-state energy is minimized if all N atoms occupy the same identical lowest-Bloch-state (the single-particle wave function for each atom is spread out over the entire lattice with L lattice sites). The many-body ground state is then given by (for a homogeneous system) as

$$|\Psi_{SF}\rangle = \frac{1}{\sqrt{N!}} \left(\hat{b}^\dagger_0\right)^N |0\rangle \quad \text{or} \quad |\Psi_{SF}\rangle = \frac{1}{\sqrt{N!}} \left(\frac{1}{\sqrt{L}} \sum_{j=1}^{L} \hat{a}_j\right)^N |0\rangle, \tag{2.11}$$

where $\hat{b}^\dagger_q = \frac{1}{\sqrt{L}} \sum_{j=1}^{L} \hat{a}^\dagger_j e^{iqx_j}$.

Then the expected value of $\langle \hat{n}(x) \rangle$ in the TOF image is given by

$$\langle \hat{n}(x) \rangle_{\text{TOF}} \propto N |\tilde{w}(q)|^2 \delta_{q,G}, \tag{2.12}$$

which predicts a high-contrast three-dimensional interference-pattern where sharp peaks arise at the zero momentum and reciprocal lattice vectors. In real experiments, what is measured is a 2D absorption image by integrating $n(\vec{x})$ along one lattice direction such as $\int dx\ \langle \hat{n}(\vec{x}) \rangle_{\text{TOF}}$. See Figs. 2.2 and 2.3.

In the Mott-insulator limit, to minimize the interaction energy, atoms tend to avoid each other. The many-body ground state is then a product of local Fock-states (also known as number states). For a commensurate filling of n atoms per site (n is an integer) in the homogenous case, the many-body ground state is

$$|\Psi_{\mathrm{MI}}\rangle = \prod_{j=1}^{L} \frac{1}{\sqrt{n!}} \left(\hat{a}_j^\dagger\right)^n |0\rangle. \tag{2.13}$$

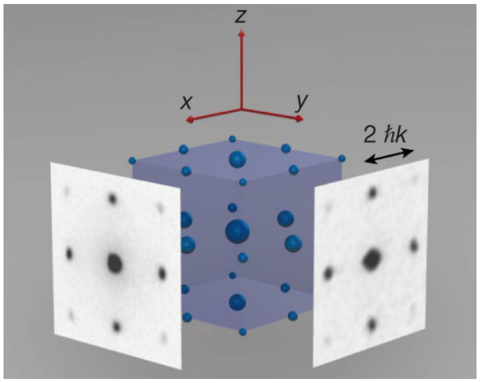

Figure 2.2: Schematic 3D interference-pattern (in the superfluid regime) with measured absorption-images taken along x and y directions after some time-of-flight. From [7].

Then the expected value of $\langle \hat{n}(x)\rangle_{\mathrm{TOF}}$ in the TOF image is given by

$$\langle \hat{n}(\vec{x})\rangle_{\mathrm{TOF}} \propto \langle \hat{n}(\vec{q})\rangle_{\mathrm{trap}} = N|\tilde{w}(\vec{q})|^2, \tag{2.14}$$

which predicts an approximated Gaussian background and no visible interference pattern.

2.4 Noise correlations and the Hanbury-Brown-Twiss spectroscopy

Although the strongly correlated properties of the Mott insulator are hidden in the TOF image of $n(\vec{x})$, they are revealed by higher-order correlations in TOF images. We now discuss how to detect noise correlations (density-density correlations) in the expanding atomic-cloud [21]. These correlations are characterized by [21, 1]

$$\langle \hat{n}(\vec{x})\hat{n}(\vec{x}')\rangle = \langle \hat{n}(\vec{x})\rangle\langle \hat{n}(\vec{x}')\rangle g^{(2)}(\vec{x},\vec{x}') + \delta(\vec{x}-\vec{x}')\langle \hat{n}(\vec{x}).\rangle \tag{2.15}$$

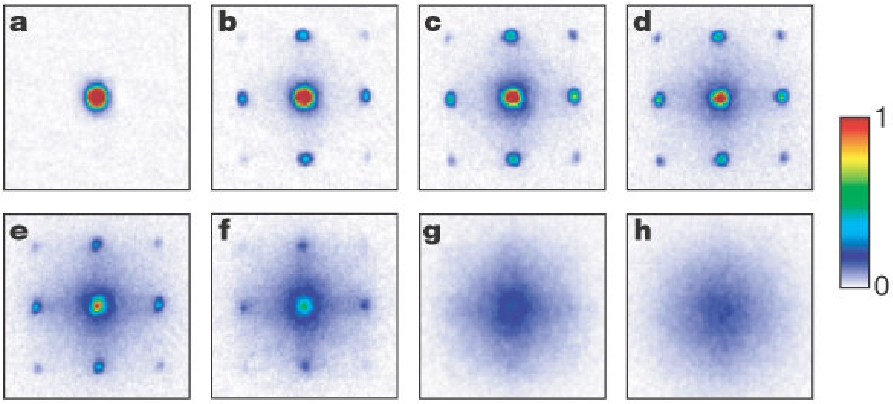

Figure 2.3: Time-of-flight images. The figure shows the interference pattern for different lattice-depths, (a) $0E_R$, (b) $3E_R$, (c) $7E_R$, (d) $10E_R$, (e) $13E_R$, (f) $14E_R$, (g) $16E_R$, and (h) $20E_R$. As the lattice depth is increased, a quantum phase-transition from superfluid to Mott-insulator occurs (The superfluid-Mott transition happens around 12-13 E_R). The ballistic-expansion time was 15ms. The narrow peaks developed during the expansion demonstrate its phase coherence across the lattice at the moment of release. Peaks appear at Reciprocal lattice vectors, with an envelope function $|\tilde{w}(\vec{q})|^2$. From [7].

Here $g^{(2)}(\vec{x},\vec{x}')$ is the normalized pair-distribution-function. $\delta(\vec{x}-\vec{x}')\langle\hat{n}(\vec{x})\rangle$ is a self-correlation term.

In a bosonic Mott-insulating or fermionic band-insulating state [31, 32, 33] in a three-dimensional simple-cubic lattice, each lattice site is occupied by a fixed atom number $n_{\vec{R}}$. Such a quantum gas is released from the lattice potential and freely expands. After a flight time t, the density-density correlation-function is given by

$$\langle\hat{n}(\vec{x})\hat{n}(\vec{x}')\rangle = |\tilde{w}(M\vec{x}/\hbar t)|^2|\tilde{w}(M\vec{x}'/\hbar t)|^2 N^2 \times \left(1 \pm \frac{1}{N^2}\left|\sum_{\vec{R}} .e^{i(\vec{x}-\vec{x}')\cdot\vec{R}(M/\hbar t)} n_{\vec{R}}\right|^2\right) \tag{2.16}$$

The plus sign corresponds to the case of bosonic particles, and the minus sign to the case of fermionic particles. The different sign reveals that noise correlations contain information on the quantum statistics. Equation (2.16) shows peaks (bunching) or dips (antibunching) in the density-density correlations for bosons or fermions whenever $\vec{q}-\vec{q}'$ is a reciprocal lattice vector $\vec{G}$ of the underlying lattice. The peaks (dips) become sharper with increasing N.

The different behavior exhibited by bosons and fermions can be understood in the following way. Consider the case of two atoms localized at two sites i and j, as indicated in Fig. 2.4 (b). There are two indistinguishable ways for particles to reach two detectors at position $P1$ and $P2$. The two paths constructively interfere for identical bosonic-particles, giving rise to bunching (peaks in the correlation function), and destructively interfere for fermions, giving rise to anti-bunching (dips in the correlation function).

The bunching for a bosonic Mott insulator and the anti bunching for a fermionic band insulator have been observed experimentally [34, 35, 18]. In these experiments, several independent images of the desired quantum-state were recorded after the atoms were released from the optical trap and let to expand for a finite time. These individually recorded images differ from each other only in the shot noise. Then by analyzing the same set of images, the spatial noise correlation function $g^{(2)}_{\text{ex}}$ is obtained as

$$g^{(2)}_{\text{exp}} = \frac{\int\langle n(\vec{x}+\vec{b}/2)n(\vec{x}-\vec{b}/2)\rangle d^2\vec{x}}{\int\langle n(\vec{x}+\vec{b}/2)\rangle\langle n(\vec{x}-\vec{b}/2)\rangle d^2\vec{x}}. \tag{2.17}$$

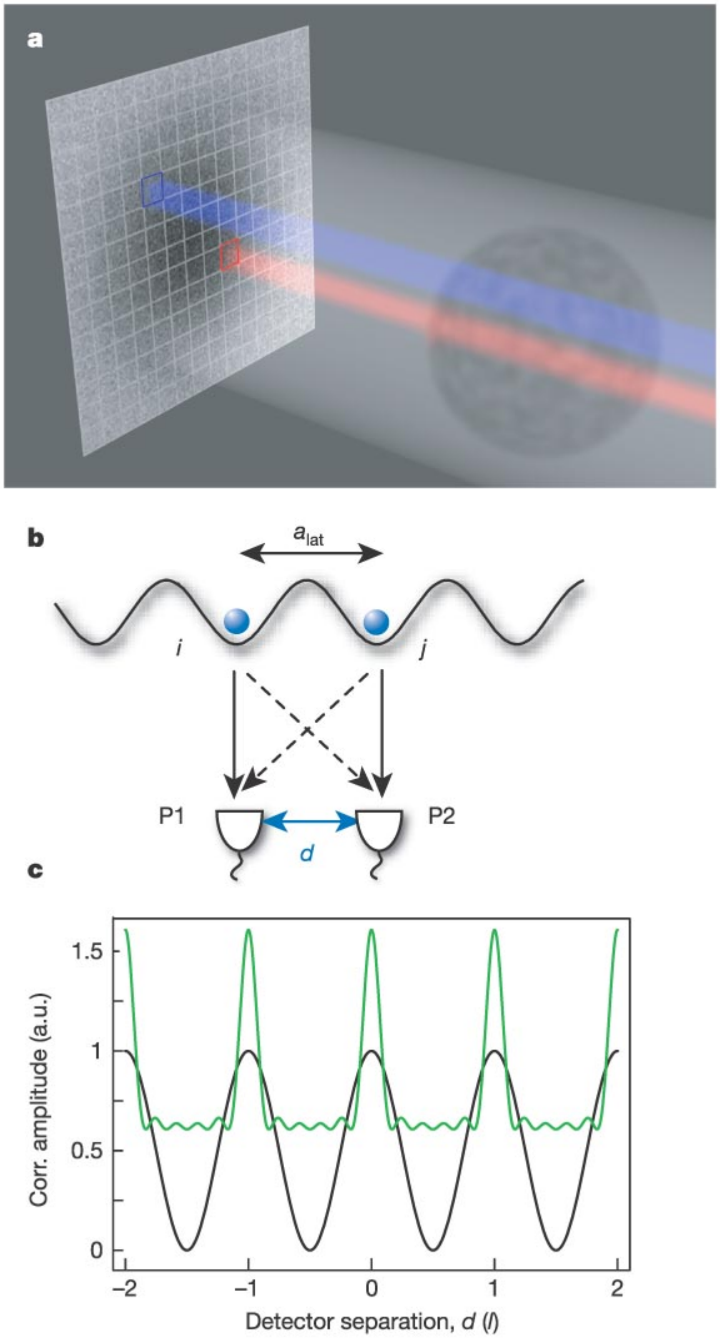

Figure 2.4: Illustration of the HBT interferometry and the origin of quantum correlations. (a), After a time-of-flight period, the absorption image of the atomic cloud is detected by a CCD camera. Two pixels of the camera P1 and P2 are highlighted, each of which records the atoms in a column along its line of sight. (b), When two atoms initially trapped at lattice sites i and j are released and detected at P1 and P2 simultaneously, the two indistinguishable paths, illustrated by solid and dashed lines, interfere constructively for bosons or destructively for fermions. (c), The resulting probability of simultaneously finding an atom at each detector is modulated sinusoidally as a function of d in the unit of l (black curve). The multiple wave generalization to a regular array of six sources with the same spacing is shown in green. a.u., arbitrary units. From [34].

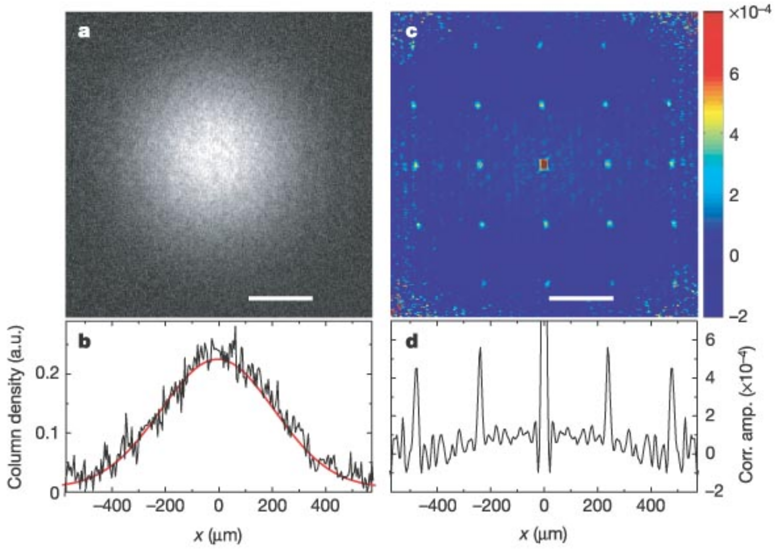

Figure 2.5: Noise correlations of a bosonic Mott insulator released from a 3D optical lattice. (a) Single shot image of the two-dimensional density-distribution of a Mott-insulating atomic cloud released from a 3D optical lattice. (b) Horizontal cross section through the center of the image in (a), and Gaussian fit to the average over many independent images. (c) Spatial noise correlations obtained by analyzing the same set of images. (d) Horizontal profile through the center of the pattern in (c). Those peaks are separated by integer multiples of $l = \frac{ht}{Ma}$, reflecting the underlying lattice-structure. From [34]

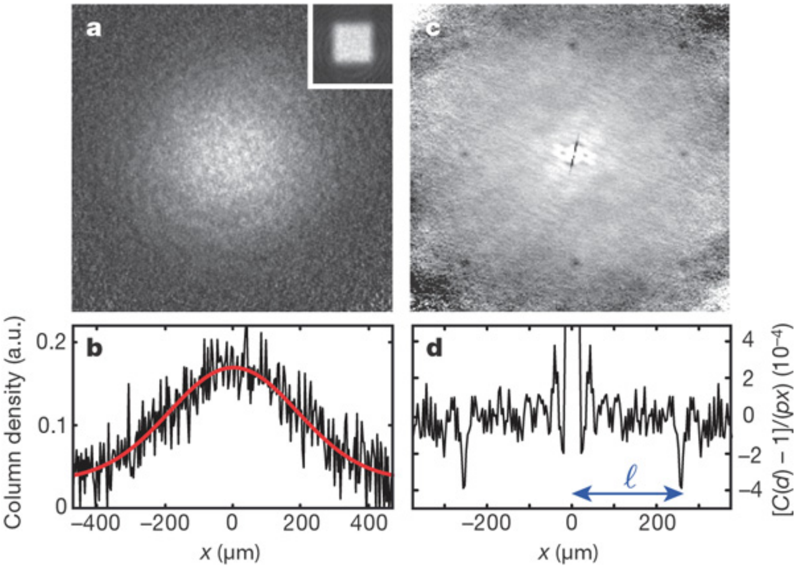

Figure 2.6: Noise correlation of a fermionic band insulator. Each plot has a similar meaning as in Fig. 2.5. Instead of the correlation "bunching" peaks observed in Fig. 2.5, the correlation function of fermioninc quantum-gas shows an antibunching effect. From [35].

As shown in Fig. 2.5 and 2.6, the Mott-insulating state exhibits long-range order in $g^{(2)}_{\text{ex}}$. Since the contribution from the averaged density $n(\vec{x})$ is smoothed out in $g^{(2)}(\vec{x},\vec{x}')$ [See Equation (2.15)], in the superfluid regime, one expects $g^{(2)}(\vec{x},\vec{x}') = 1$. In contrast, the Mott-insulator state exhibits long-range order in the pair correlation function, manifesting as an array of peaks with spacing $l = ht/aM$ in the noise correlation function.

2.5 Cold atoms in one dimension

2.5.1 Interaction strength γ

Correlation effects strongly depend on dimensionality. The experimental realization of cold atoms confined in waveguides [5, 6] provides a way of reaching the strong-interaction regime in dilute gases.

In 1963, Elliot Lieb and Werner Liniger [36] calculated the exact solutions for 1D Bose gases with $\delta(z)$ interactions (Lieb-Liniger gas). In 1998, Olshanii extended the discussion to atoms in a highly elongated cigar-shaped potential [37]. The interaction strength of a 1D gas is usually characterized by the dimensionless parameter $\gamma = E_{\text{int}}/E_{\text{kin}}$, where E_{kin} is the quantum kinetic-energy needed to correlate particles by localizing them with respect to each other on the order of the mean inter particle distance d, $E_{\text{kin}} = \frac{\hbar^2}{2Md^2}$. $E_{\text{int}} = g_{1D}n_{1D}$ is the average mean-field interaction, with g_{1D} the strength of the 1D interaction, and $n_{1D} = 1/d$ the 1D density.

Assume that a gas of cold atoms is loaded in a strong 2D optical lattice in the x, y directions, which tightly confines the atoms in the transverse direction. In the regime where the excitation energy $\hbar\omega_\perp$ of motion in the x, y direction is larger than the chemical potential, only the lowest vibrational state $\phi_0(x,y) = \frac{\exp\left[-\frac{x^2+y^2}{2a_\perp^2}\right]}{\sqrt{\pi}a_\perp}$ is accessible. At the same time, atoms can move freely along the z direction. [1] In a realistic system, the harmonic-oscillator length $a_\perp = \sqrt{\hbar/\mu\omega_\perp}$ (where $\mu = M/2$ is the reduced mass) in the transverse direction is usually larger than the 3D s-wave scattering-length a_s. Then by integrating the 3D interaction-potential over the transverse

---

[1] Considering two atoms in a harmonic confining-potential, the atomic motion can be separated into a center-of-mass motion and a relative motion. The relative wave functions are of the form $\phi_0(x,y)e^{-ikz}$.

direction, $g \int d^3x |\phi_0(x,y)|^2 \delta(\vec{x})$, one can get the resulting 1D effective interaction $g_1\delta(x)$ with $g_1 = g|\phi_0(0,0)|^2 = 2\hbar\omega_\perp a_s$ in the weak confining limit $a_s \ll a_\perp$. Consequently

$$\gamma = \frac{2a_s}{n_{1D}a_\perp^2}. \tag{2.18}$$

In contrast to the 3D situation, the strength of interaction γ scales inversely with the density n_{1D}. Therefore, in 1D, interactions dominate in the low-density limit. For $\gamma \gg 1$, the interacting bosons behave like non interacting fermions — the so-called Tonks Girardeau (TG) gas. $\gamma = 5.5$, was reached experimentally [5] and clear signatures of the fermionization of the gas were demonstrated. The momentum distribution of TG gas with a superimposed lattice-potential along z was also observed for ultracold atoms [6].

2.5.2 Two-particle correlations $g^{(2)}$

An intuitive understanding of the gradual transition from a weakly interacting gas and TG regimes with increasing value of γ can be gained by considering the two-particle pair correlations[2] $g^{(2)}(x) \equiv \frac{\langle \hat{n}(x)\hat{n}(0)\rangle - \delta(x)\langle \hat{n}(x)\rangle}{\langle \hat{n}(x)\rangle\langle \hat{n}(0)\rangle}$. It is a measure of the probability of observing two particles separated by x simultaneously. For an ideal BEC in three dimensions, $g^{(2)}(\vec{x}) = 1$ at arbitrary $\vec{x}$. For the Lieb-Liniger gas, the local value of the pair correlation $g^{(2)}(0)$ can be calculated exactly [38], which gives $g^{(2)}(0) = 1 - 2\sqrt{\gamma}/\pi + \cdots$ in the limit of $\gamma \ll 1$ and $g^{(2)}(0) = (2\pi/\sqrt{3}\gamma)^2 \to 0$ when $\gamma \gg 1$. Experimentally, $g^{(2)}(0)$ was determined by Kinoshita *et al*, [39] using photoassociation. As shown in Fig. 2.7, the experimental results are in good agreement with theory over a wide range of interaction strengths.

---

[2] Those measurements were *in situ*, but not after time of flight.

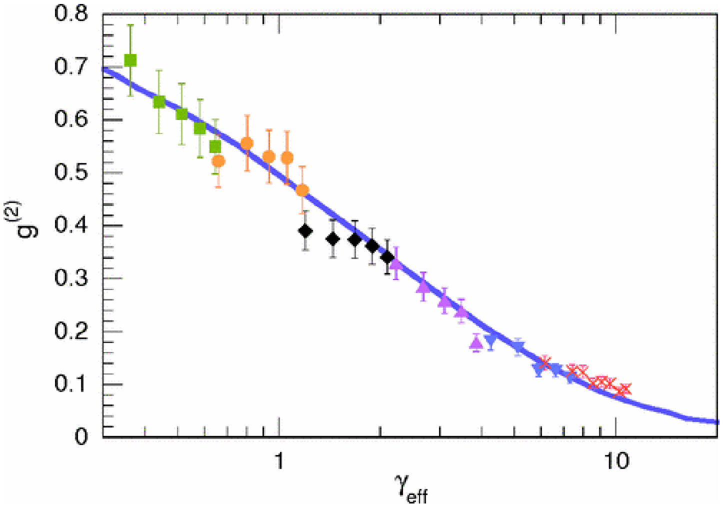

Figure 2.7: Local pair correlation function $g^{(2)} \equiv g^{(2)}(0)$ as a function of interaction strength γ. The solid line shows the theory prediction from [38] . The plot is taken from [39].

Chapter 3

Quantum correlations in bichromatic lattices

Correlation functions can be used as powerful tools to characterize complex phases. In this chapter, we study the many-body Schrödinger equation in a quasi-periodic potential and calculate the momentum distribution and noise correlations. We discuss the connection between them with the Kolmogorov-Arnold-Moser (KAM) problem of classical mechanics. We propose a possible visualization of such a connection in experimentally accessible many-body observables. Those observables are useful probes for the three characteristic phases predicted in a bichromatic lattice: the metallic, Anderson, and band-insulator phases. In addition, we show that those correlation functions exhibit fingerprints of nonlinear phenomena such as bifurcations and devil's staircases.

3.1 Introduction

Systems with competing lengths have fascinated physicists as well as mathematicians because of their exotic fractal-characteristics [40, 41]. Such systems with two competing periodicities, commonly known as almost-periodic or quasi-periodic, occur very commonly in nature. The most commonly studied example in quantum physics is the single-particle Schrödinger equation in the presence of a quasi-periodic (QP) potential.

Motivated by the experimental realization of two-color lattices, we revisit the problem of the Schrödinger equation in a quasi-periodic potential and its relationship with the Kolmogorov-Arnold-Moser (KAM) [42] problem of classical mechanics. Our particular focus is the treatment at the many-body level of those effects that have been extensively studied in QP systems at the single-particle level. By focusing on experimentally accessible observables, such as the momentum distribution and density-density correlations, we demonstrate the possibility of experimental visualization of the relationship between the metal-insulator transition and the KAM-Cantori transition [43] in many body systems. These observables are found to exhibit fingerprints of various paradigms of nonlinear systems such as Arnold tongue-like structures, bifurcations, and devil's staircases.

The many-body systems that we treat here are ensembles of ultracold spin-polarized fermionic atoms confined in one-dimensional bichromatic optical-lattices. We treat cases in which the two lattices have incommensurate periodicities, and thus constitute a quasi-periodic potential for atomic motion [44]. Since the metal-insulator transition in single-particle QP systems is associated with a localization transition of extended single-particle states, a natural probe of such transitions in many-particle systems is the density distribution and density-density correlations. At present, the density distribution of atoms confined in a lattice is not an easily accessible experimental observable; instead, the quasi-momentum distribution and its corresponding correlation-functions can be easily measured after the lattice potential is suddenly removed.

Using the momentum-position duality of our basic model [45, 46], we show that TOF images encode local-density information and can be used to identify the possible phases of ultracold atomic-gases, e.g., metallic phases and various types of insulators. Many of our results are explained analytically with perturbation theory, although the complete picture is obtained by exact numerical calculations, particularly near the metal Anderson-insulator transition.

This chapter is organized as follows. First, we give an overview of experiments on ultracold atoms in QP optical lattices. Then we discuss the basic Hamiltonian, and the experimental observables. After that, we describe the relationship between the metal Anderson-insulator transition and KAM-Cantori transition, and follow it by a discussion of possible experimental manifestations of effectively nonlinear behavior in these many-body systems. Finally, we provide a summary of our results and state our conclusions.

3.2 Ultracold atoms in a 1D bichromatic optical lattice

The systems of interest here are gases of ultracold spin-polarized fermionic atoms trapped in the lowest band of a transversal 2D optical-lattice. For many systems of current experimental interest, where atomic interactions are short-range, spin-polarized fermions are effectively noninteracting because of Pauli blocking. The 2D lattice depth is made strong enough to freeze the motion of the atoms transversally, creating an array of independent 1D tubes [5, 47]. Along the axis of the 1D tubes, additional optical lattices can be imposed, as has been done in Refs. [48, 6]. We discuss cases in which two such lattices are imposed, with incommensurate periods [8] (when one of these lattices is much stronger than the other, we refer to it as the primary lattice). The combined lattices therefore generate an effective QP potential along the axial direction. Such an experiment has been recently implemented for bosonic atoms in Ref. [49]. Our treatment considers cases where the ratio of the two lattice constants is equal to the "golden mean", $\sigma = (\sqrt{5} - 1)/2$, which is one of the best-studied examples in QP systems [46].

In most experiments, atoms are first trapped and cooled to quantum degeneracy. They are subsequently loaded into the lattice by adiabatically turning on the lattice laser beams. At the end of each experimental sequence, atoms are probed by using TOF images. These are obtained after releasing the atoms by turning off all the confinement potentials. The atomic cloud expands and is then photographed after it enters the ballistic regime. Assuming that the atoms are noninteracting from the time of release, properties of the initial state can be inferred from the spatial images [21]: the column density distribution image reflects the initial quasi-momentum distribution, and the density fluctuations, namely the noise correlations, reflect the quasi-momentum fluctuations. These quantities, which will be defined below —see Eqns. (3.5,3.6)—, have been shown to be successful diagnostic tools for characterizing quantum phases and have been recently measured in bosonic quasi-periodic systems [50].

3.3 Our model system: The Harper equation, many-body observables and self-duality

3.3.1 The Harper equation

If the intensity of the secondary lattice is much weaker than that of the primary lattice, the low energy physics of the fermionic system can be well described by the tight-binding Hamiltonian[8]:

$$H = -J\sum_j (\hat{c}_j^\dagger \hat{c}_{j+1} + \hat{c}_{j+1}^\dagger \hat{c}_j) + \sum_j V_j \hat{n}_j, \tag{3.1}$$

where $\hat{c}_j$ is the fermionic annihilation operator at the lattice site j, and J is the hopping energy between adjacent sites. The main effect of the QP potential is to modulate the on-site potential. It is accounted for by the term $V_j = 2V_0\cos(2\pi\sigma j + \phi)$. The parameter V_0 is proportional to the intensity of the lasers used to create the secondary lattice [44], σ is the ratio between the wave vectors of the two lattices that we choose to take the value $\sigma = (\sqrt{5}-1)/2$, and ϕ is a phase factor that is determined by the absolute registration of the two lattices.

To model real experimental-conditions, averaging over ϕ is required. This averaging takes into account, on one hand, the phase fluctuations from one preparation to another. Those arise because of the difficulty of locking the position of the cloud over several shots. On the other hand, the fact that typical experimental setups generally consist of an assembly of one-dimensional tubes with different lengths and phases among them.

For a single atom, the eigenfunctions $\psi_j^{(m)}$ and eigenenergies $E^{(m)}$ of the Hamiltonian in Eqn. (3.1) satisfy:

$$-\left(\psi_{j+1}^{(m)} + \psi_{j-1}^{(m)}\right) + 2\lambda\cos(2\pi\sigma j + \phi)\psi_j^{(m)} = \epsilon^{(m)}\psi_j^{(m)}, \tag{3.2}$$

where $\lambda = V_0/J$, $\epsilon^{(m)} = E^{(m)}/J$, and $\epsilon^{(m)} \leq \epsilon^{(m+1)}$. Equation (3.2) is known as the Harper equation, a paradigm in the study of 1D quasi-periodic (QP) systems [46]. For irrational σ, the model exhibits a transition from extended-to-localized states at $\lambda_c = 1$. Below criticality, all the states are extended Bloch-like states characteristic of a periodic potential. Above criticality, the Harper model becomes equivalent to a corresponding Anderson model, the spectrum is a pure point spectrum, and all states are exponentially localized. At criticality, the spectrum is a Cantor set and the gaps form a devil's staircase of measure unity [40].

In our numerical studies, σ is approximated by the ratio of two Fibonacci-numbers F_{M-1}/F_M, $(F_1 = F_0 = 1, F_{i+1} = F_i + F_{i-1})$ that describe the best rational approximant by continued fraction-expansion of σ. For this rational approximation, the unit cell has length F_M, and the single-particle spectrum consists of F_M bands and $F_M - 1$ gaps. The gaps occur at $Q_n/2$, $\pm(\pi - |Q_n|/2)$ with $Q_n = \pm(2\pi/a)\langle n\sigma\rangle$ reciprocal lattice vectors constrained in the interval $aQ_n \in (-\pi, \pi]$. Here $\langle n\sigma\rangle = n\sigma \pmod 1$, and n an integer. We denote by N_p the number of atoms, $N_l = F_M$ is the number of lattice sites, and the filling factor $\nu = N_p/N_l$ ranges from 0 to 1.

3.3.2 Many-body observables

An ensemble of spin-polarized fermions at zero temperature are "stacked up" into the single-particle eigenstates of increasing energy, with one particle per quantum-state. The energy of the highest occupied-level, which depends on the filling factor ν, is the Fermi energy, E_F. Since at the critical point all the single-particle wave-functions become localized, at the many-body level polarized fermions also exhibit a transition from metal to insulator at λ_c. However, in addition to these two phases, the fragmentation of the single-particle spectrum in a series of bands and gaps introduces additional band-insulator phases when the Fermi energy lies within a gap. The most relevant insulating phases occur at the irrational filling factors: $\nu = F_{M-1}/F_M$ and $\nu = F_{M-2}/F_M$ (which respectively correspond to $\nu = \sigma, 1 - \sigma$), associated with the leading band gaps. In the band insulator phases the many body system is an insulator, irrespective of the value of λ, as the extended-single-particle states are occupied.

Since the metal-insulator transition is clearly signaled by the onset of localization of extended single-particle states, a natural probe of this transition is the many-body density profile, ρ_j, and the density-density correlations, $\Delta(j_1, j_2)$, which can be written in terms of single particle wave functions as:

$$\begin{aligned} \rho_j &= \langle \hat{n}_j \rangle = \sum_{m=1}^{N_p} \left| \psi_j^{(m)} \right|^2 \text{, and} && (3.3) \\ \Delta(j_1, j_2) &= \langle \hat{n}_{j_1} \hat{n}_{j_2} \rangle - \langle \hat{n}_{j_1} \rangle \langle \hat{n}_{j_2} \rangle = \sum_{m=1}^{N_p} \left| \psi_{j_1}^{(m)} \right|^2 \delta_{j_1, j_2} - \left| \sum_{m=1}^{N_p} \psi_{j_1}^{(m)*} \psi_{j_2}^{(m)} \right|^2 . && (3.4) \end{aligned}$$

Here $\hat{n}_j = \hat{c}_j^\dagger \hat{c}_j$, and we have used Wick's theorem to evaluate $\Delta(j_1, j_2)$. However, in general, such local observables are hard to measure experimentally because of the lack of addressability of individual lattice- sites for typical lattice-spacing. Instead, TOF images access nonlocal observables such as the quasi-momentum distribution, $\hat{n}(Q)$ and the quasi-momentum fluctuations, $\Delta(Q, Q')$, which are given by

$$\begin{aligned} \hat{n}(Q) &= \frac{1}{N_l} \sum_{i,j} e^{iQa(i-j)} \hat{c}_i^\dagger \hat{c}_j \text{, and} && (3.5) \\ \Delta(Q, Q') &= \langle \hat{n}(Q) \hat{n}(Q') \rangle - \langle \hat{n}(Q) \rangle \langle \hat{n}(Q') \rangle, && (3.6) \end{aligned}$$

where Q is the quasi momentum that can be expressed in terms of the index k (k is an integer) as $Q(k) = \frac{2\pi}{a} \frac{k}{N_l}$. $Q(k)$ is constrained to the interval $Qa \in (-\pi, \pi]$.

Introducing η_k, the Fourier transform of ψ_k,

$$\eta_k^{(m)} = \frac{1}{\sqrt{N_l}} \sum_j e^{-i \frac{2\pi k j}{N_l}} \psi_j^{(m)}, \tag{3.7}$$

where the observables n_k (also denoted sometimes as $n[Q(k)]$) and $\Delta(Q) \equiv \Delta(Q, 0)$ can be written as

$$\begin{aligned} n_k &= \sum_{m=1}^{N_p} \left| \eta_k^{(m)*} \eta_k^{(m)} \right|, && (3.8) \\ \Delta[Q(k)] &= \sum_{m=1}^{N_p} \left| \eta_0^{(m)} \right|^2 \delta_{k,0} - \left| \sum_{m=1}^{N_p} \eta_k^{(m)*} \eta_0^{(m)} \right|^2 . && (3.9) \end{aligned}$$

3.3.3 Self-duality

The self-duality of the Harper equation corresponds to the property that single-particle eigenstates ψ_j and their corresponding Fourier-transformed eigenstates, $z_n \equiv \frac{1}{\sqrt{N_l}} e^{-in\phi} \sum \psi_j e^{-ij(2\pi\sigma n + \theta)}$

satisfy the same equation with the roles of J and V_0 interchanged [45, 46], i.e.,

$$-\left(z_{n-1}+z_{n+1}\right)+\frac{2}{\lambda}\cos(2\pi\sigma n+\theta)z_n=-\frac{\epsilon}{\lambda}z_n.. \tag{3.10}$$

The self-duality of the Harper equation implies that if ψ is an extended-eigenstate, its self-dual eigenstate z is localized and vice-versa. η_k is connected to z_n by the relation $z_n=\eta_k e^{-in\phi}$ with $k=\mathrm{Mod}[nF_{M-1},F_M]$ when θ is set to 0.

Thouless has developed a formula [51] that relates the exponent for the decay of a localized state to the integrated density of states. Denoting γ_1 and γ_2, respectively, as the decay exponent of the localized states for ψ and z, the Thouless relation can be written as,

$$\gamma_1(E) = \int dE' \ln\left|\frac{2(E-E')}{J}\right|\rho(E'). \tag{3.11}$$

$$\gamma_2(E) = \int dE' \ln\left|\frac{2(E-E')}{V_0}\right|\rho(E'). \tag{3.12}$$

The above equations imply that,

$$\gamma_1(E)=\gamma_2(E)+\ln\left(\frac{V_0}{J}\right). \tag{3.13}$$

Since γ_i $(i=1,2)$ is related to the integrated density of states, $\gamma_i\geq 0$. Consequently, if ψ is localized, then z must be extended, and therefore γ_2 must be zero and $\gamma_1=\ln(\lambda)$. The exponent γ, also known as the Lyapunov exponent, describes the exponential growth of the renormalized couplings in the renormalization-group equations [52, 53].

Self-duality is a key to obtaining experimental information on local quantities from measurements. In this context, it is important to understand the relationship between the index j of ψ_j that satisfies the Harper equation (3.2) and its corresponding index k in η_k that satisfies the dual equation (B.1). We obtain this relationship numerically by diagonalizing the Harper equation for a given λ, labeling the states in increasing order in energy, and then finding the corresponding momentum-space dual by repeating the same procedure, but with λ replaced by $1/\lambda$. An explicit example of the mapping is provided in Appendix B. Note that Fibonacci sites in real space are mapped to Fibonacci sites in momentum space up to a common displacement. This shift is dependent on the phase factor ϕ.

3.4 Localization transition as a KAM-Cantori transition

As discussed by Ostlund *et al.* [52, 53], there is a close parallel between the KAM problem of classical mechanics and the quantum problem of a particle in a QP potential.

Firstly, both systems share the mathematical difficulty of having higher-order terms with small denominators when the QP potential in the quantum problem or the nonintegrable term in the classical problem are treated perturbatively. In the classical system, Kolmogorov, Arnold and Moser (KAM) [42] solved this "small divisor" problem and demonstrated that most of the invariant tori in the phase space are not destroyed by a sufficiently weak nonintegrable perturbation, and the phase space trajectories of these weakly perturbed nonintegrable systems are topologically equivalent to those of an integrable system. Outside the perturbative regime, extensive studies have shown that the KAM tori break, becoming an invariant cantor-set, known as Cantori [43]. The transition from KAM tori to Cantori has been studied extensively using numerical and by nonperturbative renormalization-group (RG) methods both in the dissipative systems, such as circle map [54], and in Hamiltonian systems such as the area-preserving standard maps [55]. The KAM-Cantori transitions resemble second-order phase transitions of statistical mechanics because the critical point can be described by a scaling theory with universal critical exponents.

In the context of QP potential, Dinaburg and Sinai [56] showed that for a sufficiently weak QP potential, a large part of the spectrum remains continuous, and the wave functions exhibit a generalized Bloch form of $\psi_n = e^{2\pi i n \kappa}\chi(n\sigma)$, where $\chi(x)$ is smooth and periodic. Outside the perturbative regime, QP systems have been studied numerically and using various RG schemes. As discussed by Ostlund *et al.* [53], the RG methods used to describe the critical point of the QP trajectories in the circle map are closely related to the RG methods used to study scaling properties of the spectrum and the wave function of the discrete Schrödinger equation with QP potential. Numerical studies [52] have demonstrated a close parallel between the KAM tori and the smooth Hull-function of the extended phase and the Cantori and the discontinuous Hull-function of the localized phase. Similar to the critical torus, the critical Hull-functions are self-similar and are characterized by universal scaling exponents.

The correspondence between the KAM-type problem of classical physics and the quantum problem of a particle in a QP potential (as described above), has been visualized within a single-particle picture. Below, we elucidate this correspondence in the many body context, which is directly relevant for current cold-atom experiments. In other words, instead of looking at the single-particle wave function, whose Hull function, $\chi(n\sigma)$, is a smooth and continuous function in the extended phase but becomes discontinuous for $\lambda > 1$, we propose to look at the return map of the local density of the atomic cloud, ρ_j vs ρ_{j+1}. This type of return map provides a cleaner visualization of the KAM-to-Cantori transition at the many-body level.

Figure 3.1 shows the return map for various rational filling factors $\nu = N_p/N_l = 1/4, 1/2$ and different values of λ. For $\lambda < 1$, the return maps are smooth curves and correspond to the KAM tori of the extended or metallic phase. For $\lambda > 1$, the density profile is a discontinuous function, a Cantori. The discreteness of the return map for generic filling factors can be easily understood in the $\lambda \to \infty$ limit, where the wave functions are fully localized, and thus the return map can only take the four possible values of $(0,0), (0,1), (1,0), (1,1)$. Exactly at the transition point $\lambda = 1$, the smooth curves become disconnected.

Using the duality transformation, similar return maps can be drawn in momentum space, n_k vs $n_{k\pm k_0}$ ($k_0 = F_{M-1}$). While nearest-neighbor sites are connected in position space because of a finite J, quasi-momentum components separated by the main reciprocal-lattice vectors of the secondary lattice are connected by a finite V_0. We find the momentum return-maps exhibit an important advantage compared with the local-density maps related to the fact that they are insensitive to variations of the phase and retain their pattern when averaged over phase. This is not the case in the density maps shown in the insets of Fig. 3.1.

We now consider the case where the filling factor is a ratio of two main Fibonacci-numbers ($\nu = \sigma, 1-\sigma$). We refer to these filling factors as irrational filling factors since they approach an irrational number in the thermodynamical limit. As discussed earlier, at irrational filling, the system is in a band-insulating phase as the Fermi energy E_F lies in the gap, just outside a filled

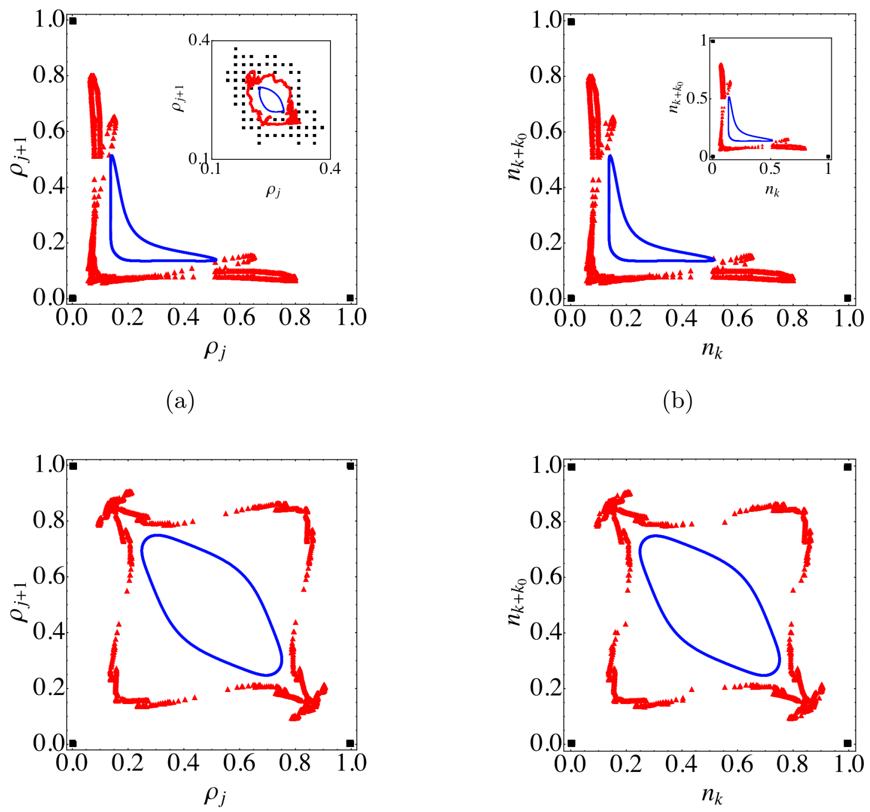

(a) (b) (c) (d)

Figure 3.1: Return maps in real space for (a) and (c) $\lambda = 10(\text{red}), 1(\text{green}), 0.5(\text{blue})$ and the corresponding return map in momentum space (b) and (d) $\lambda = 0.1(\text{red}), 1(\text{green}), 2(\text{blue})$. The filling factors are $\nu = 0.25$ for the upper panels, and $\nu = 0.5$ for the lower panels. The insets are averaged over 50 random phases.

band.

In contrast to the generic or rational filling factors discussed earlier, the return map for the irrational-filling case ($\nu = 1 - \sigma$) is found to remain smooth regardless of the value of λ (See Fig. 3.2). This result may appear somewhat counterintuitive because as $\lambda \to \infty$, all the single-particle wave functions become localized. However, an exception to this simple picture occurs near irrational filling when the density function exhibits a continuous distribution. This difference between rational and irrational filling is due to the presence of a group of paired states centered around the most dominant band edges (associated with the dominant gaps). Each of

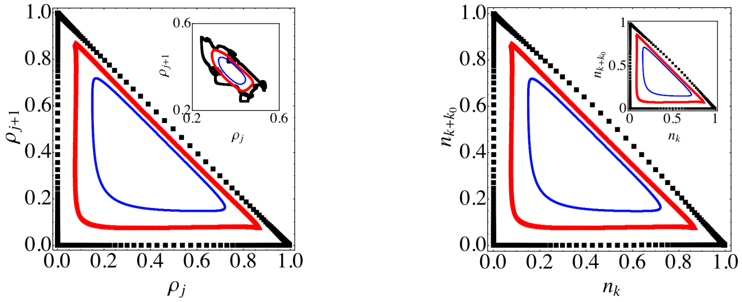

(a)

(b)

Figure 3.2: Return maps for the irrational filling factor $\nu = 1 - \sigma$. Panel (a) is in real space with $\lambda = 10(\text{red}), 1(\text{green}), 0.5(\text{blue})$ and panel (b) is in momentum space with the dual values $\lambda = 0.1(\text{red}), 1(\text{green}), 2(\text{blue})$. The insets are averaged over 50 random phases.

those states is dimerized, in other words we mean that they localize at two neighboring sites. The existence of a pair of such dimerized states is the key to understanding the difference between rational and irrational filling. Although a single dimerized-state causes delocalization near band filling (explaining irrational filling case), the existence of a pair can cancel the delocalization effect. Technical details of this argument are presented in Appendix C, where we show that the smooth character of the map at the irrational fillings, $\sigma, 1-\sigma$ associated with the leading gaps can be understood by the breakdown of nondegenerate perturbation theory in the large λ limit.

In summary, the band insulating phase belongs to the KAM phase irrespective of the strength of the disorder.

3.5 Fingerprints of nonlinear phenomena in many-body observables

We now study the quasi-momentum distribution of polarized fermions, that is directly accessible in the TOF images of ultracold atoms. In the following, we will show how the quasi-momentum distribution imprints a signature of the KAM-Cantori transition and provides experimental realization of various landmarks of nonlinear systems.

3.5.1 Fragmented Fermi sea

Fermions in the extended phase have metallic properties. For $\lambda = 0$, the single particle eigenstates are fully localized in quasi-momentum space (and thus delocalized in position space). The quasi momentum distribution $n(Q)$ has a step-like profile: $n(Q) = 1$ for $|Q| \leqslant Q_F$ and $n(Q) = 0$ for $|Q| > Q_F$ (Q_F is the Fermi momentum). For $0 < \lambda < 1$, the single particle eigenstates localized at k acquire some admixture of other quasi-momentum components ($n_{k \pm F_{M-1}}$ to leading order in λ). In this regime, the quasi-momentum distribution retains part of the step-like profile but gets fragmented into additional structures centered at different reciprocal lattice vectors of the secondary lattice. We call the filled states centered around $Q = 0$ the main Fermi sea and those around the QP-related reciprocal lattice vectors the quasi-Fermi seas.

The fragmentation of the quasi-momentum distribution and the development of QP Fermi

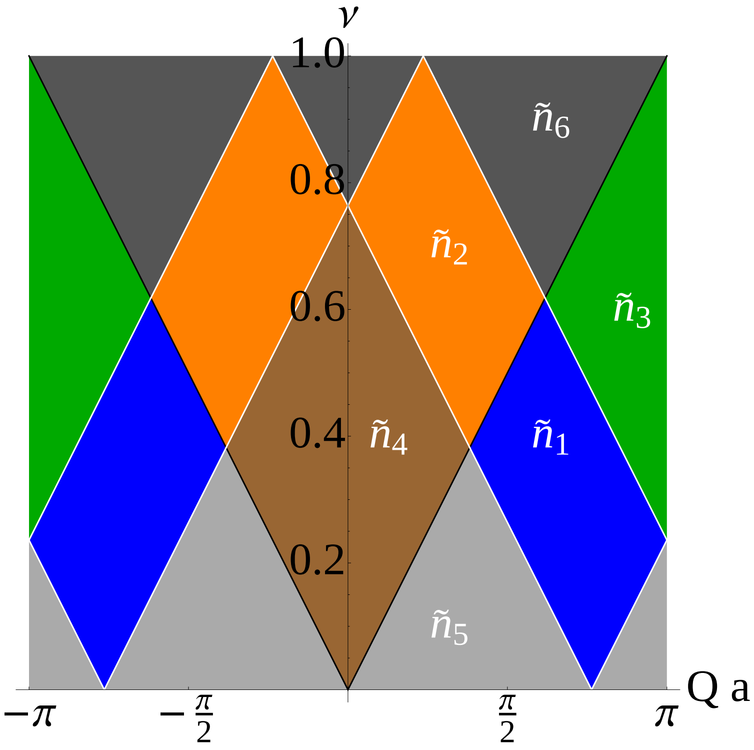

Figure 3.3: Various boundaries of the fragmented Fermi sea.

seas can be understood from first-order perturbation theory. To leading order in λ, the perturbation tools discussed in Appendix C can be used to show that the momentum landscape becomes fragmented in six regions, as shown in Fig. 3.3 and given by:

$$\tilde{n}_1(Qa) = \left(\frac{\lambda}{2}\right)^2 \frac{1}{4\sin^2\Theta \sin^2\left(|Qa| - \Theta\right)}, \tag{3.14}$$

$$\tilde{n}_2(Qa) = 1 - \tilde{n}_1(\pi - |Qa|), \tag{3.15}$$

$$\tilde{n}_3(Qa) = \left(\frac{\lambda}{2}\right)^2 \frac{1}{4\sin^2\Theta} \left(\frac{1}{\sin^2\left(|Qa| + \Theta\right)} + \frac{1}{\sin^2\left(|Qa| - \Theta\right)}\right), \tag{3.16}$$

$$\tilde{n}_4(Qa) = 1 - \tilde{n}_3(\pi - |Qa|), \tag{3.17}$$

$$\tilde{n}_5(Qa) = 0, \text{and} \tag{3.18}$$

$$\tilde{n}_6(Qa) = 1, \tag{3.19}$$

where $\Theta = \frac{F_{M-2}}{F_M}\pi = \frac{|Q_1 a|}{2}$. The various regions are delineated by the edges of the QP Fermi seas, shown by white lines in Fig. 3.3 and given in the Q vs ν space by

$$\nu = \frac{a}{\pi}|Q(k \pm \sigma N_l)| = \frac{a}{\pi}|Q(k \pm F_{M-1})|. \tag{3.20}$$

The regions $\tilde{n}_{1,2}$, $\tilde{n}_{3,4}$ and $\tilde{n}_{5,6}$ reflect the characteristic particle-hole symmetry in fermionic systems.

As disorder is increased, more quasi-Fermi seas become visible, and with the increase of ν they overlap in a complicated pattern. Exactly at criticality, $\lambda = 1$, the pattern evolves into a fractal-like structure. Beyond the critical point, $\lambda > 1$, the fragmented quasi-momentum distribution profile disappears and instead becomes a smooth function of Q and ν. This behavior is summarized in Fig. 3.4, and the corresponding cross sections for fixed Q and ν are displayed in Figs. 3.5 and 3.6.

At irrational filling factors, however, the quasi-momentum distribution profile remains smooth regardless of the value of λ. The smoothness of the momentum distribution at these special filling factors can be understood using the same reasoning as the one used to understand the smooth character of the return map in position space in terms of nondegenerate perturbation theory. In this case, however, the states that are coupled are the ones localized at the quasi-momenta $Q_F + \epsilon$ and $-Q_F + \epsilon$, $(\epsilon a \ll 1)$.

The fragmentation of the Fermi sea in the $\lambda < 1$ regime, and the smooth profile in both the $\lambda > 1$ and band-insulator phases are directly connected via the self-duality property to the discrete nature of the density return map in the localized phase, and its smooth character in the extended and band-insulator phases.

An important point to emphasize again, which is crucial for possible experimental observation of the predicted behavior, is the insensitivity of the momentum distribution to variations of the phase ϕ. We demonstrate such insensitivity by noticing that the quasi-momentum distributions plotted in Fig. 3.4 are actually averaged over many different values of ϕ. Hereafter, all the plots in momentum space are always averaged over 50 random phases.

The emergence of a tongue-like structure (see Fig. 3.7) as the QP potential increases and its disappearance beyond criticality is reminiscent of the mode-locked windows such as Arnold

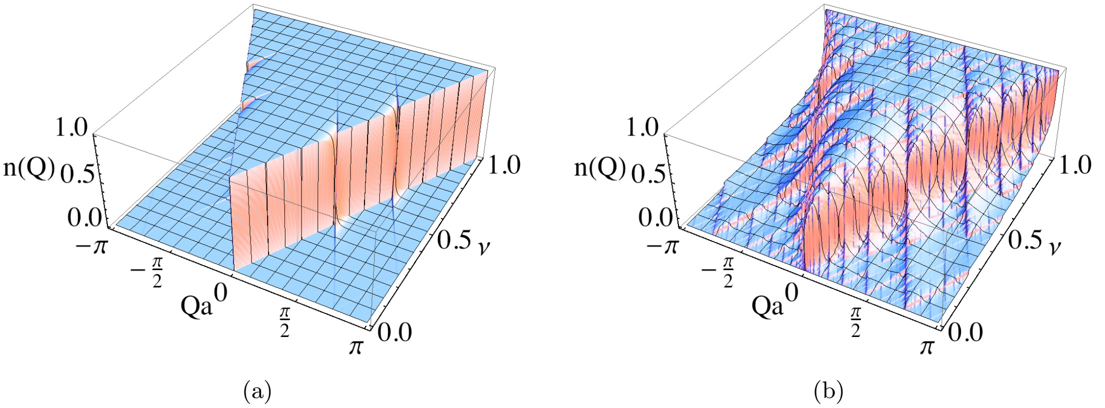

(a)

(b)

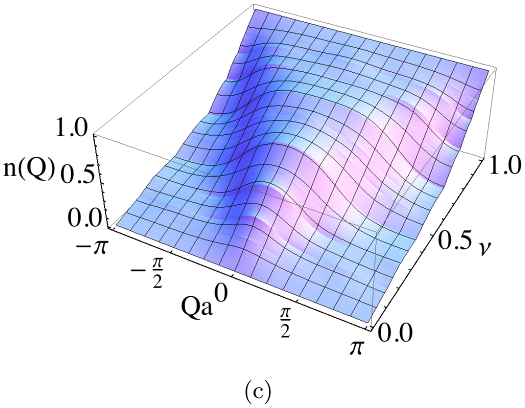

(c)

Figure 3.4: Momentum distribution for (a)$\lambda = 0.1$, (b)$\lambda = 1$, (c)$\lambda = 2$. All figures are averaged over 50 random phases to mimic a realistic experimental case. We can see that the sharp features of these distributions survive phase averaging.

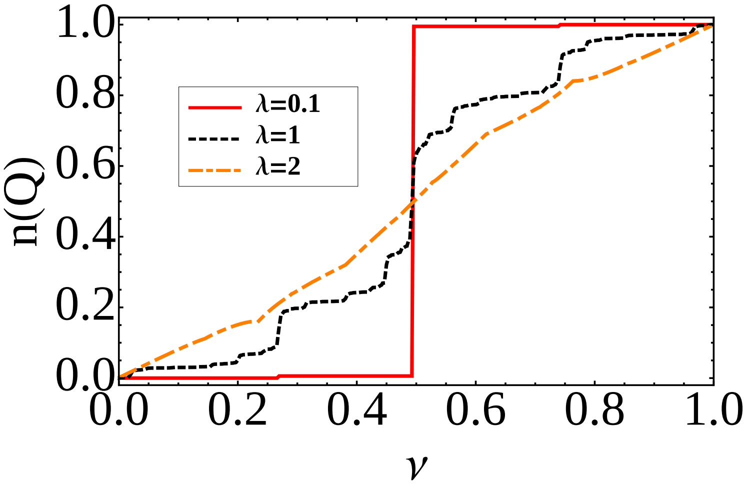

Figure 3.5: Momentum distribution for fixed $Q(k = 1045)$, $F_M = 4181$ as a function of filling factors vs. the disorder parameter.

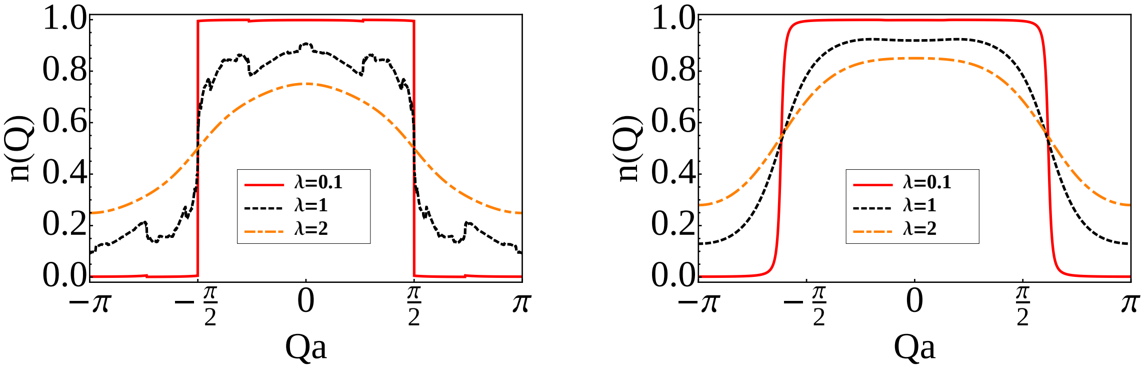

(a)

(b)

Figure 3.6: Momentum distribution vs. the disorder parameter. (a) $\nu = 0.5$, and (b) $\nu = F_{M-1}/F_M$.

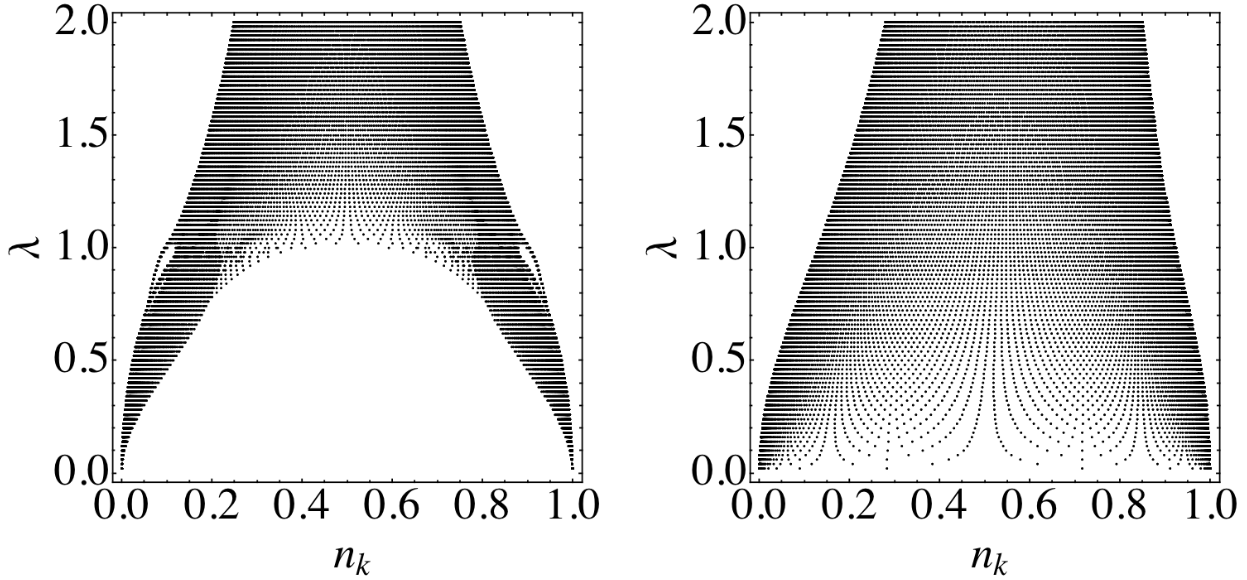

(a)

(b)

Figure 3.7: Momentum distributions as a function of the disorder parameter. (a) filling factor $\nu = 0.5$. Here we see the formation of two tongues that merge at the critical value $\lambda = 1$. (b) $\nu = \sigma$. When ν is irrational, the system is a band insulator and the Arnold tongue-like structure disappears. We have checked for the existence of the similar structure in position space when converting λ to $1/\lambda$.

tongues in QP circle maps [57]. For $\lambda = 0$, the Fermi distribution is a binary distribution with only two values $n(Q) = 0, 1$. For finite λ and for generic filling factors, two windows of values centered around zero and unity become allowed. Their width increases with λ as they can be derived from a perturbative analysis. We call such windows QP tongues. Exactly at the onset of the metal-insulator transition, the two distributions overlap, mimicking the Arnold tongue overlap at the onset to transition. We have checked that the duality of the Harper equation allows one to observe the formation of analogous structures in position space. The absence of a metal-insulator transition at the irrational filling factors at which the system is a band insulator is also signaled by the disappearance of the tongues at these fillings, as shown in Fig. 3.7(b).

3.5.2 Bifurcations

Bifurcations are common features observed in nonlinear dynamical systems that occur when a small smooth change made to specific parameters (the bifurcation parameters) of the system causes a sudden 'qualitative' or topological change in system behavior. A series of bifurcations can lead the system from order to chaos.

The density distribution provides a nice manifestation of a single bifurcation with λ as a bifurcation parameter. When the density at the various Fibonacci sites is plotted as a function of λ, for a specific filling factor that depends on the value of ϕ, a bifurcation opens up at $\lambda = 1$. In Fig. 3.8, the existence of a bifurcation at quarter filling ($\nu = 1/4$) when $\phi = 3\pi/4$ is shown.

A qualitative understanding of the bifurcation can be gained by considering the two limiting regimes, $\lambda \ll 1$ and $\lambda \gg 1$. In the weak-coupling limit, $\lambda \ll 1$, the local density is uniform and directly proportional to the filling factor ν. In contrast, in the strong coupling limit, a given site remains empty or occupied depending upon whether the on-site potential is greater than or less than the Fermi energy.

Fibonacci sites $j = F_n$ have similar on-site energies that oscillate about $\epsilon_c \equiv 2\lambda \cos(\phi)$

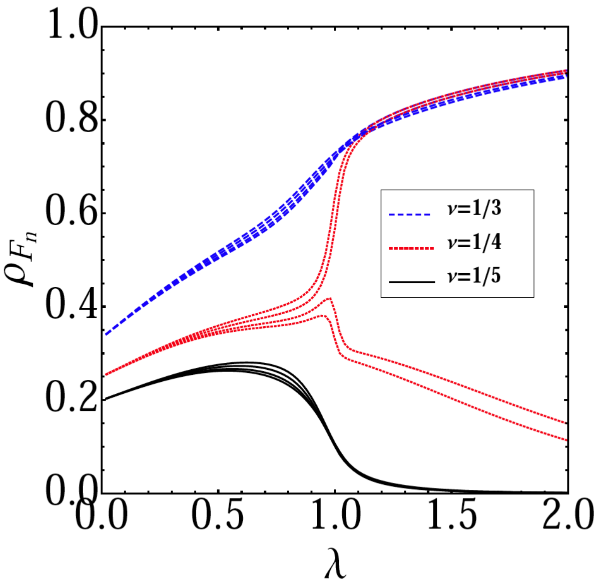

Figure 3.8: Bifurcation of local density at Fibonacci sites. The central curve (red triangle) corresponds to quarter filling while the lowest (black blocks) and the topmost (blue disks) curves, respectively, correspond to $\nu = 1/5$, and $\nu = 1/3$. Quarter filling is a special case where the local density at Fibonacci sites is 0 or 1 as $\lambda \to \infty$. For $\nu > 0.25$, the Fibonacci sites are filled, while for $\nu < 0.25$ Fibonacci sites are empty as $\lambda \to \infty$. We have checked for the existence of the same bifurcation phenomena in the quasi-momentum distribution, but with the weak and the strong coupling limits reversed ($\lambda \to 1/\lambda$).

(assuming $n \approx M$ and $\phi > 2\pi F_{M-n}/F_M$) as

$$2\lambda\cos(2\pi\sigma F_n + \phi) = 2\lambda\cos\left[2\pi(-1)^{n-1}F_{M-n}/F_M + \phi\right] \begin{cases} < \epsilon_c & \text{n is odd} \\ > \epsilon_c & \text{n is even.} \end{cases} \tag{3.21}$$

These oscillations can be seen in Fig. B.1 in Appendix B.

Consequently, at the filling factor, ν_c, at which the Fermi energy matches ϵ_c (e.g., if $\phi = 3\pi/4$, then $\nu_c \sim 0.25$) Equation (3.21) implies that as λ goes to infinity, even Fibonacci sites (F_{2l}) become empty and odd Fibonacci sites (F_{2l+1}) become occupied. This behavior, combined with the monotonic increase of the density with λ in the weak coupling limit, qualitatively explains the observed bifurcation.

The self-duality behavior described by Eq. (3.10) implies the existence of the same bifurcation phenomena in quasi-momentum distribution, but with the weak and the strong coupling limits

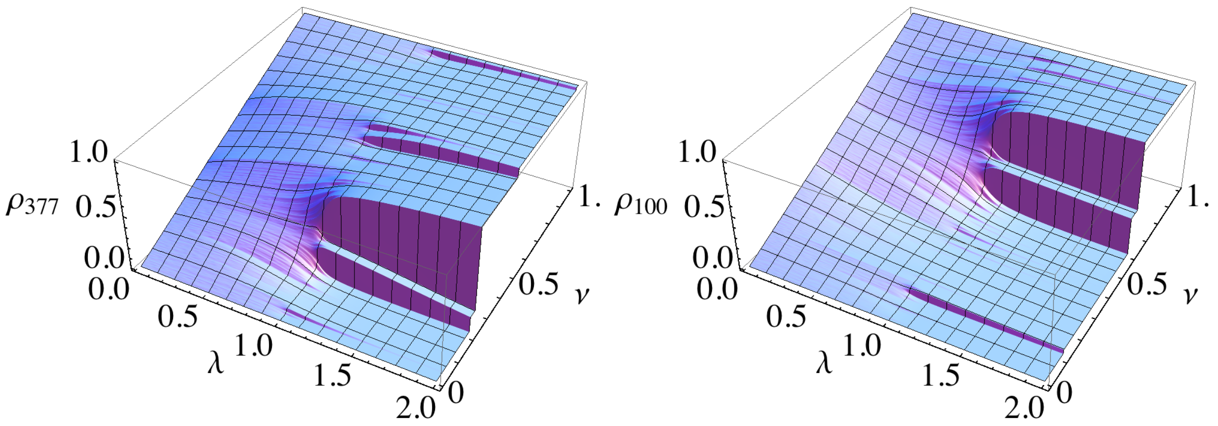

(a) (b)

Figure 3.9: Local density distribution as the disorder parameter and filling factor are varied for (a): Fibonacci site $j = 377$ and (b): normal site $j = 100$. We have checked the self-duality behavior in the quasi-momentum distribution with the weak and the strong-coupling limits reversed ($\lambda \to 1/\lambda$).

reversed ($\lambda \to 1/\lambda$).

When the local density is plotted for a generic lattice site as a function of λ and ν, the landscape shows a similar change in topology. In contrast to Fig. 3.8 where the filling factor is fixed but different curves corresponding to different Fibonacci sites are shown, in Fig. 3.9 the density at a specific lattice site is plotted, but both the filling factor and disorder strength are varied. In this plot, besides the large bifurcation, there are smaller ones which cannot be explained by studying the two limiting cases. However, in momentum space they are qualitatively understood by considering cuts at a fixed λ as a function of ν. In these cuts the big jump at small λ can be identified with the edges of the main Fermi sea in the quasi-momentum profile and the smaller jumps correspond to edges of the quasi-Fermi seas.

3.5.3 Devil's staircases

A Devil's staircase describes a self similar function $f(x)$, with a hierarchy of jumps or steps. In other words, $f(x)$ exhibits more and more steps as one views the function at a smaller and smaller length scale. The derivative of $f(x)$ vanishes almost everywhere, meaning there exists a set of points of measure 0 such that for all x outside it, the derivative of $f(x)$ exists and is zero.

Cold atom experiments may provide an opportunity to visualize Devil's staircases in momentum-momentum correlations, namely the noise correlations.

Measurement of noise correlations is an example of Hanbury-Brown-Twiss interferometry (HBTI), which is sensitive to intrinsic quantum noise in intensity correlations. HBTI is emerging as one of the most important tools for providing information beyond that offered by standard momentum distribution-based characterization of phase coherence. The noise correlation pattern in 1D QP bosonic systems has been studied theoretically [58, 59, 60, 61] and has also been measured experimentally [50]. Here, however, we focus on the fermionic system.

In the extended phase, noise correlations exhibit a series of plateaus as ν is varied, and the number of steps or plateaus increases as the strength of the disorder λ increases. The origin of this step-like structure with jumps occurring at the filling factors $\nu_{ju}^{(n)} = |Q_n|a/\pi$ can be understood from a perturbative argument as follows. For noninteracting fermions, for $Q \neq 0$ (See Fig. 3.10), $\Delta(Q(k)) = -\sum_{m=1}^{N_p} \left|\eta_k^{(m)}\eta_0^{(m)}\right|^2$, with $\eta_k^{(m)}$ being the Fourier transform of the m^{th} single-particle eigenfunction. For $\lambda = 0$, the overlap between any two different Fourier components is always zero as only the ground $(m = 1)$ state has a zero quasi-momentum component, i.e., $\eta_0^{(1)} = 1$. For small $\lambda \ll 1$, first-order perturbation theory yields a single step observed at $\nu_{ju}^{(1)} = |Q_1|a/\pi$, as only $\eta_0^{(m^{(1)})}$ with $m^{(1)} = \nu_{ju}^{(1)} N_l$ is nonzero.

Quantitatively, from first-order perturbation theory, the heights of the steps at $\nu_{ju}^{(1)}$ for $\lambda \ll 1$ are given by,

$$\begin{aligned}
\zeta(0) &= -2\left(\frac{\lambda}{2}\right)^2 \frac{1}{(1-\cos(2\pi\sigma))^2}, \\
\zeta(Q_1) &= \left(\frac{\lambda}{2}\right)^2 \frac{1}{(1-\cos(2\pi\sigma))^2}. \qquad (3.22)
\end{aligned}$$

where $\zeta(0)$ $(\zeta(Q_1))$ is the step height for $\Delta(0)$ $[\Delta(Q_1)]$ at filling factor $\nu_{ju}^{(1)}$. The minus sign implies a decrease in the noise as the filling factor ν increases. As λ increases, more and more steps are seen and can be explained using higher-order perturbation theory. At criticality (see Figs. 3.10–3.11), the steps acquire a hierarchical structure that resembles a Devil's staircase and correlates with the

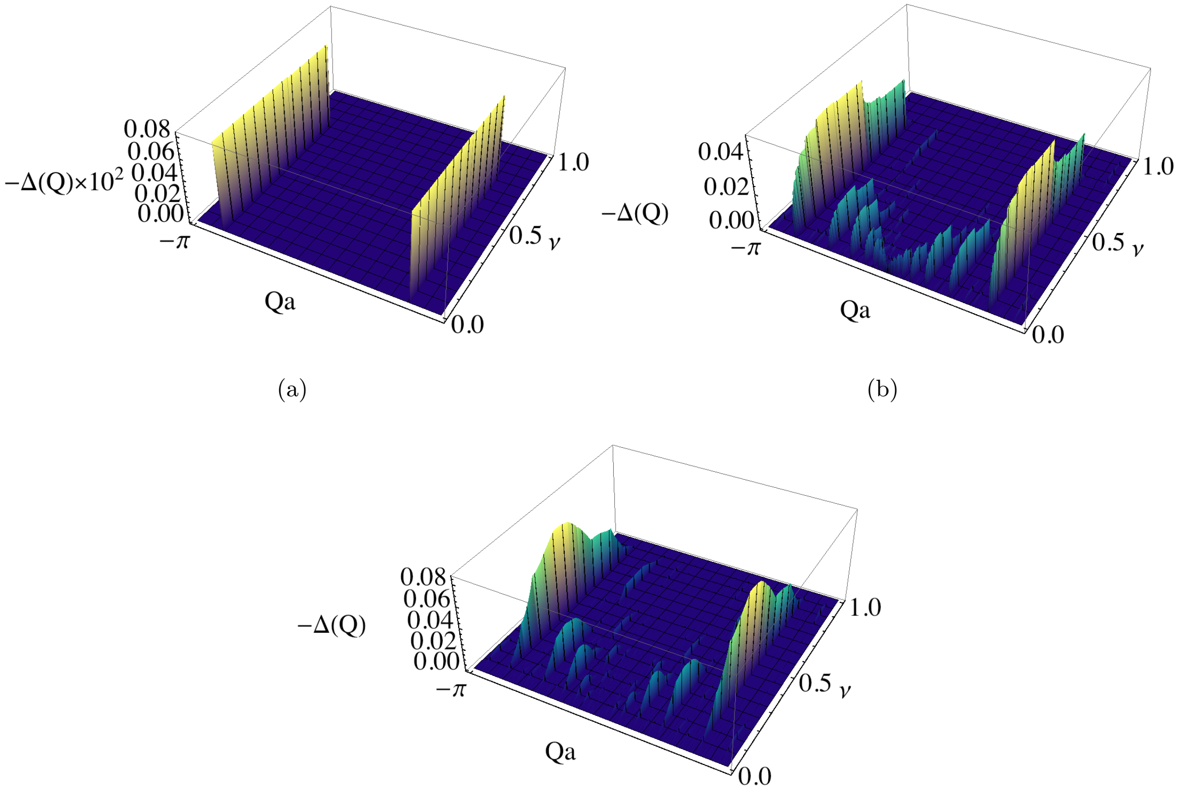

(a)

(b)

(c)

Figure 3.10: Noise correlation for (a)$\lambda = 0.1$, (b)$\lambda = 1$, (c)$\lambda = 2$. All plots display averaged quantities over 50 random phases. We can see that the structure in the noise correlations survives phase averaging, as they do in the momentum distributions of Fig. 3.4. $\Delta(Q = 0)$ is not displayed in those plots.

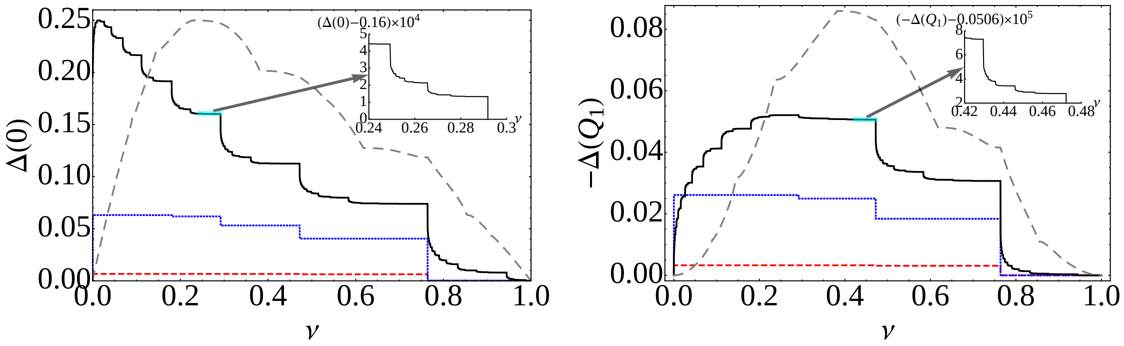

(a)

(b)

Figure 3.11: This figure shows the evolution of $\Delta(Q_n)$ ($n = 0, 1$) as a function of the filling factor for different λ values. In the limit $\lambda \ll 1$, $\Delta(Q_n)$ exhibits steps occurring at the filling factors $\nu_{ju}^{(m)}(m = 1, 2, \dots)$ (see text). In the limit $\lambda \gg 1$, it acquires a sinusoidal profile. The inset shows the self-similar nature of the steps at $\lambda = 1$.

fractal structure of the energy spectrum [52, 53]. In contrast to the momentum distribution, noise correlations do not show significant differences between the rational and irrational filling factors.

In the localized phase, $\lambda > 1$, we see the smoothing of the step-structure and the noise correlation function tends towards a sinusoidal profile $\Delta(Q_n) \approx \nu\delta_{n,0} - \frac{\sin^2(\pi\nu n)}{(\pi n)^2}$.

To emphasize the striking difference between the noise patterns in the extended and localized phases (the step-like vs. smooth profile), in Fig. 3.12, we plot a measure of the gaps developed in $\Delta(0)$ as a function of λ.

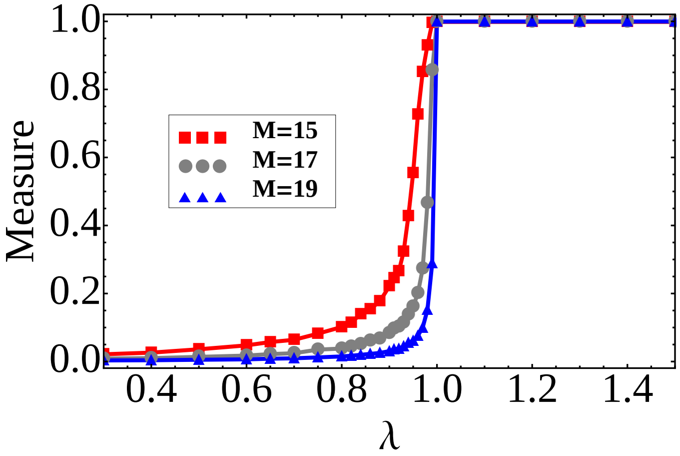

Figure 3.12: This figure shows a measure of the gaps in $\Delta(0)$ vs. λ for different system sizes, F_M. We deem that a gap occurs if $|\Delta(0)(N_p+1) - \Delta(0)(N_p)| > \epsilon$ (we choose $\epsilon = 10^{-15}$ here). We can see that with increasing M, the measure of the gaps approaches a step function with the step position at $\lambda = 1$.

3.6 Summary

We now summarize our key results in this chapter:

(1) Extended-localized vs KAM-Cantori phases

At the many-body level, the connection between the metal-insulator transition and the KAM-Cantori transition is signaled in the return map of the local density between nearest-neighbor sites. For a given angle ϕ, the metallic phase with extended single-particle wave functions exhibits a smooth return map. We identify this with the preserved-invariant

KAM tori in phase space at weak perturbations in the corresponding classical system. The localized phase displays a discrete return map, which we identify with the remaining tori or Cantori outside the perturbative regime. This behavior is shown in Fig.3.1. In addition, for the particular filling factors at which the system becomes a band insulator, the return map remains smooth for any value of λ (see Fig. 3.2).

Similar behavior can be observed in the corresponding momentum-distribution return map. However, while the local-density return map loses these characteristic features after averaging over ϕ, the momentum-distribution return map remains almost unaffected. The robustness of the momentum return map to phase variations is ideal for the experimental visualization of the metal-insulator vs KAM-Cantori connection in cold atoms.

(2) Quasi-fractal structures

The introduction of weak disorder modifies the characteristic step-function–Fermi-sea profile of the quasi-momentum distribution. Additional step-function structures centered at different reciprocal lattice vectors of the QP lattice appear for $\lambda > 0$. We refer to those structures as the “quasi-Fermi seas”. With increasing λ and ν, the number and width of the various quasi-Fermi seas increase the fragmentation of the momentum distribution, turning it into a complex pattern. At $\lambda = 1$ the fragmentation becomes maximal, and the momentum distribution evolves into a smooth profile as the system enters the localized phase (See figures 3.3-3.6).

A more appropriate analogy of such behavior can be observed by considering the set of values taken by quasi-momentum distribution for a given filling factor. In the absence of disorder, this distribution can only have the values of 1 or 0, depending upon whether quasi momentum is greater or smaller than the Fermi quasi momentum. As the strength of the quasi-periodic lattice increases, two distributions of values develop, centered around 0 and 1 respectively. Their width increases with increasing disorder and they overlap exactly at criticality (Fig. 3.7). We refer to those windows as Arnold tongue-like structures because of their resemblance to Arnold tongues in classical mechanical systems.

(3) Bifurcations

The overlap between various Arnold tongue-like structures at λ_c, can be linked, using the space-momentum duality transformation, to the appearance of a bifurcation in the density profile. The bifurcation occurs at a common, but phase-dependent, filling for the various Fibonacci sites (Fig. 3.8). At generic lattice sites, the filling factor at which the bifurcation takes place also depends on the lattice site under consideration and can be observed when the local density is plotted as a function of λ and ν (Fig. 3.9) .

(4) Devil's staircases

Noise correlations plotted as functions of the filling factor exhibit step-like structures that evolve into a Devil's staircase at the onset to the metal-insulator transition (Figs. 3.10–3.12).

Systems with competing periodicities stand in between periodic and random systems. The richness and complexity underlying such systems have been studied extensively [46]. Ultracold atoms are emerging as a promising candidate to simulate a wide variety of physical phenomena. Here we have shown they offer opportunities to experimentally realize various paradigms of nonlinear dynamics.

Our focus here was on spin-polarized fermionic systems, since we wanted to look at the simplest consequences of many-body physics in disordered systems. However, Bose-Einstein condensed systems may also be used as tools for laboratory investigation of various predictions made for the quasi-periodic systems based on single-particle arguments [44]. For example, it might be possible to confirm the strong-coupling universality prediction, which establishes that the ratio of the single particle density at two consecutive Fibonacci sites should be a universal number [62].

Chapter 4

Self-trapping dynamics in a 2D optical lattice

Cold gas experiments are well suited to studying out-of-equilibrium dynamics, such as the evolution of many-body correlations, since experimental time scales are relatively slow yet faster than typical relaxation and decoherence rates [63, 28, 64]. In this chapter, we introduce an interesting nonequilibrium phenomenon called "self-trapping" that is caused by a competition between discreteness introduced by the optical lattice and nonlinear effects due to atomic interactions. In collaboration with experimental colleagues at Pennsylvania State University [65], we found what seems to be a new type of Macroscopic Quantum Self-Trapping (MQST) effect induced by quantum correlations in a gas of ultracold ^{87}Rb atoms trapped in a two-dimensional optical lattice. The lattice potential created coupled arrays of 1D tubes. A striking inhibition of the transverse expansion dynamics was observed as the depth of the 2D lattice was increased.

Here we describe in detail various theoretical models developed to understand the observed behavior. The main conclusion is that the ST phenomena observed in this experiment is very likely caused by the strong correlations between atoms in the same tube. At first, the pure mean-field model based on the solution of coupled-nonlinear equations fails to reproduce the experimental observations. It greatly overestimates the initial expansion rates at short times and predicts a slower expansion rate of the cloud at longer times. It also predicts the formation of a hole surrounded by a steep square fort-like barrier that was not observed in the experiment. An improved theoretical description based on a simplified Truncated Wigner Approximation (TWA) (See Ref. [66] and references therein), which adds phase and number fluctuations to the initial conditions, pushes the theoretical results closer to the experimental observations, but fails to quantitatively reproduce them. To further investigate the role of genuine quantum correlations as a localization mechanism and to benchmark the validity of the approximated TWA, we study the expansion dynamics in a simpler two-tube configuration using exact numerical time-dependent Density Matrix Renormalization Group (t-DMRG) methods (See Ref. [67, 68] and references therein).

The outline of this chapter is as follows. In section 4.1, we introduce the concept of self-trapping and review the experiments where the MQST has been observed. In section 4.2, we review the treatment of MQST in terms of a mean-field model and the application of this method to prior experiments. In Sec. 4.3, we introduce our experimental setup [69] and explain a mean-field treatment of the dynamics capable of dealing with the axial expansion along the tubes. We compare our solutions obtained by numerical evolution of the nonlinear equations with the experimental data. To overcome the limitations of the mean-field model, in section 4.4 we discuss ways to incorporate quantum fluctuations using the aTWA methods. In section 4.5, we use t-DMRG to study the problem of atoms tunneling between two tubes and use it to test the parameter regime in which the GPE and the aTWA are valid. Those calculations show the relevance of quantum correlations during the expansion dynamics. Finally, we conclude in Sec. 4.6.

4.1 Introduction to self-trapping

The term “self-trapping” was first introduced by Landau to describe the motion of an electron in a crystal lattice [70]. According to Landau, the electron gets dressed by the lattice polarization and deformation caused by its own motion. The resulting *polaron* can be localized or self-trapped in the presence of strong electron-lattice interactions. Nowadays, the concept of self-trapped polarons is applied to various condensed matter systems such as semiconductors, organic molecular crystals, high-temperature cuprate superconductors and colossal magnetoresistance manganates [71, 72, 73]. Still, the theory of the dynamical coupling of a conduction electron to lattice phonons is a complicated highly nonlinear problem that is difficult to tackle even in one-dimensional situations [74]. Many questions remain open.

Macroscopic self-trapping in quantum degenerate Bose gases, where mean-field energy gradients suppress tunneling, presents an interesting set of non equilibrium phenomena, with analogs nonlinear photonics optics [75, 76] and Josephoson junction arrays [77]. Macroscopic self-trapping has been studied theoretically in all dimensions [78, 79, 80, 81, 82, 83, 84, 85, 86] and experimentally in double-well systems and in arrays of 2D pancake-like BECs [87, 88]. In those systems, self trapping is caused by a competition between the discreteness introduced by the lattice and nonlinear effects. However, in these systems, the lattice potential is rigid (imposed by optical fields), and the nonlinearity has its roots in intrinsic interatomic interactions. The self-trapping mechanism is then inherently a many-particle phenomenon, commonly referred to as MQST.

MQST can be understood as wave-packet localization caused by the interaction-induced suppression of tunneling in the presence of chemical potential gradients. In those cases, a mean field description in terms of the so called time-dependent Gross-Pitaevskii equation (GPE) is shown to be sufficient to describe the experiments.

In contrast to other self-trapping experiments, in the experiment we study, the cloud is allowed to freely expand along the axis of the tubes, so that the atom density decreases with time. The inhibited expansion persists until the density became too low to sustain MQST.

The observed transverse localization was not reproduced by a pure mean-field analysis. When phase fluctuations among the tubes were added to the theory in an attempt to approximate the effect of correlations, the agreement with the experiment improved for shallow lattices. But for deep lattices, the calculated suppression of tunneling was less complete than what was observed in the experiment, even with maximal phase fluctuations. In Ref. [65] we proposed a possible mechanism for this effect that cannot be reproduced by modifying mean-field theory. 1D gases develop quantum correlations to reduce their mean-field energy. Atoms might be prevented from tunneling because of the mean field energy cost they would have to pay in the adjacent tube, with whose atoms they are not properly correlated.

A simple understanding of this mechanism can be gained in the Tonks-Girardeau regime where because of quantum correlations bosons fermionize [89, 5, 90]. Instead of a macroscopically occupied single-particle wave function, the many-body wave function is more like a set of spatially distinct single-particle wave functions to avoid interactions. In this case it is clear that tunneling between adjacent tubes can be suppressed because of the large interaction-energy cost an atom would have to pay because of mismatched correlations between tubes, i.e., if the only region that an atom can access via tunneling (which exponentially decreases with distance) in the adjacent tube overlaps with the wave function of an atom already present there.

The succession of MSQT experiments from the double well BEC (coupled 3D gases with no lattice), to coupled 2D gases in 1D lattices, to the coupled 1D gases in 2D lattices, is something of a microcosm of the way cold atom physics has developed. As atoms become more confined and the coupling strength increases, the GPE ceases to capture all the important physics. Quantum correlations play an enhanced role, giving rise to new phenomena and posing a challenge to theory. It is natural to speculate that the new type of MSQT that appears in 2D lattice experiments could also be affecting transport in 3D lattice experiments.

4.2 MQST: an overview

A dilute bosonic gas forms a Bose Einstein condensate (BEC) below a critical temperature. The GPE has proven to be a very powerful and successful way to describe the dynamics of BECs.

A BEC confined in a double well potential can experience MQST. This was predicted theoretically [78, 79, 80] and has been directly observed experimentally [87]. MQST was induced in the experiment by creating a population difference between the left and right well. For small population imbalance, the atoms oscillate back and forth between the wells, as expected for noninteracting atoms, but beyond a critical population imbalance, the mean-field interactions inhibit tunneling and the atoms become self-trapped.

At the mean-field level, the double-well system can be described by a two-state model as

$$i\hbar\frac{d}{dt}\begin{pmatrix}\psi_L\\ \psi_R\end{pmatrix}=\begin{pmatrix}U_LN_L+E_L^0 & -J\\ -J & U_RN_R+E_R^0\end{pmatrix}\begin{pmatrix}\psi_L\\ \psi_R\end{pmatrix}, \tag{4.1}$$

where ψ_L and ψ_R are “macroscopic” wave functions of the particles in the left and right wells, J is the tunneling matrix element, and $U_{L,R}$ describe the interaction energy cost of having two particles in the left or in the right well respectively. $N_{L,R} = |\psi_{L,R}|^2$ are the numbers of particles in the two wells, and $E_{L,R}$ are the respective zero-point energies. These parameters can be determined by the overlap integrals of the eigenfunctions of isolated wells.

We set $E_L + E_R = 0$ and denote the zero point energy difference between the two levels as $\Delta E = E_R - E_L$. Assuming that all particles initially occupy one well, when $U_{L,R}N_{L,R} \rightarrow 0$, Eqn. (4.1) yields Josephson oscillations of the population with a frequency $\sqrt{4J^2 + \Delta E^2}$ and an amplitude $\frac{4J^2}{4J^2+\Delta E^2}$. When $\Delta E \gg J$, the system is off-resonant and the atoms oscillate rapidly with a small amplitude around the initial configuration.

When $\Delta E = 0$ and $|U_L N_L - U_R N_R| \gg J$, the atoms also show reduced-amplitude oscillations. In this case, however, the population imbalance is self-locked to the initial value because of MQST.

MQST in 1D optical lattices has also been studied theoretically and observed experimentally [82, 88, 83, 81]. Atoms were first loaded in a 1D optical lattice with an additional dipole trap, forming arrays of 2D pancake-like BECs. Then the dipole-trapping beam along the lattice direction was suddenly removed. Even though the 1D lattice system is more complicated than the double well, the physics responsible for the MQST is similar in the two cases. In the 1D lattice MQST manifests as a dynamical localization of an initially prepared wave packet. In contrast to the noninteracting case, in which a continuous increase of the width of the wave packet with time is expected, interactions can stop the expansion. The MQST starts at the edges of the cloud where the density gradient is the largest. As the system evolves, atoms form a hole at the center surrounded by immobile steep edges. In Ref. [88], the MQST behavior was probed by directly imaging the atom spatial distribution. At a critical value of interaction energy, a transition from diffusive dynamics (monotonic expansion of the wave packet with time) to MQST was observed.

The local dynamics of MQST in lattices is complex, but the global dynamics, i.e., evolution of the root-mean-square (RMS) width of the wave packet can be predicted analytically using a very simple model. A variational ansatz has been used to predict when MQST will occur, and the result is solely determined by global properties of the gas [81]. It has been applied to 1D lattice systems in which the lattice splits the BEC into an array of two dimensional "disks" or pancakes [88]. The predictions of the model were found to be in qualitative agreement with the experimental observations. Details of the variational method are presented in the Appendix D.

4.3 MQST in a 2D lattice

During the expansion, dynamics took place in an array of quasi-1D tubes, where atoms expanded along the tubes as they underwent their transverse dynamics. This made it possible to observe a self-trapping transition "on the fly", as the overall density steadily dropped because of the axial expansion.

A BEC of $N \sim 3.5 \times 10^5$ ^{87}Rb atoms was initially prepared in a crossed-dipole-harmonic trap with transverse frequency $\omega_\perp = 2\pi \times 38$ Hz and vertical confinement $\omega_{||} = 2\pi \times 94$ Hz. It was then loaded into a 2D square-lattice potential with lattice spacing $a = 385$ nm. Details of the experimental setup are given in Ref. [69] and the experimental geometry is depicted in Fig. 4.1. The blue-detuned 2D lattice was ramped up in time according to $I(t) \propto [1-(t/\tau)]^{-2}$, reaching a final lattice depth of $V_0 = 7.25\ E_R, 9.25\ E_R, 11\ E_R$ or $13\ E_R$ and creating an array of 1D tubes. Here I is the lattice intensity, $\tau = 4.15$ ms is the time constant, and $E_R = h^2/(8Ma^2)$ is the recoil energy, where d is the lattice spacing. After the initial preparation, all the harmonic confining potentials were suddenly turned off so that the atoms could expand in the 2D lattice. The expansion dynamics were investigated by direct imaging. The line of sight was along a direction 45 degrees between the lattice directions (45 degrees from x and y), and the image of the 2D density-distribution squared was recorded as a function of time. The main finding was a suppressed expansion rate of the RMS width of the density profile along the lattice, consistent with MQST. However, the expansion rate did not agree with the mean-field predictions. Moreover, no signature of MQST behavior predicted by the mean-field theory was observed, such as the formation of steep edges or a hole at the center of the density profile.

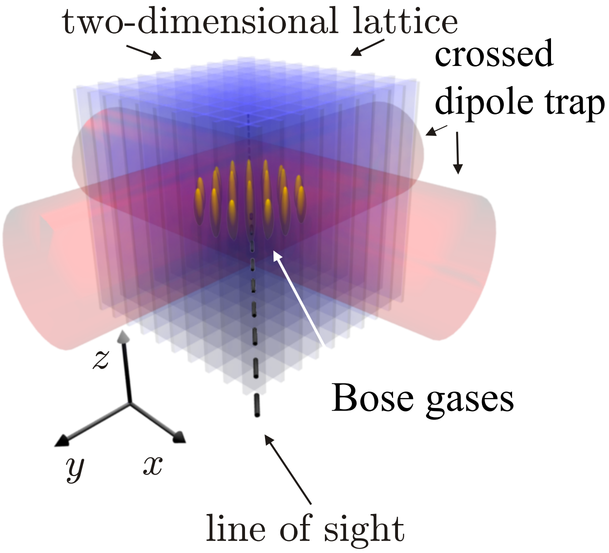

Figure 4.1: Schematic of the experimental setup. A BEC of ^{87}Rb atoms was initially prepared in the crossed-dipole-harmonic trap. A 2D optical lattice along the x-y direction was then adiabatically ramped on to create an array of quasi-1D tubes. The crossed dipole-trap was then turned off, and the expansion dynamics in the presence of the 2D periodic potential were investigated by direct imaging. The line of sight was at 45 degrees from the lattice directions (45 degrees from x and y). The 2D atom density distribution was recorded after various expansion times.

4.3.1 Mean field: Coupled GPEs

For the 2D lattice configuration, the total external potential was given by $V_{\text{ext}}(x,y) = V_{\text{lat}}(x,y) + V_{\text{dip}}(\vec{x})$ with $V_{\text{lat}}(x,y) = V_0[\sin^2(\pi x/a) + \sin^2(\pi y/a)]$ the lattice potential and $V_{\text{dip}}(\vec{x}) = \frac{1}{2}M\omega_{\perp}^2(x^2+y^2) + \frac{1}{2}M\omega_{||}^2 z^2$ the confinement introduced by the crossed-dipole-trap. The dipole confinement was turned off during the expansion, and therefore it was only relevant for determining the initial conditions. A small antitrapping potential remained because of the Gaussian profile of the laser beams that generated the lattice. The parameters of the crossed dipole trap used to set up the initial state in the theoretical model were chosen so that the atom distribution matched the initial spatial extent and energy of the atoms in the experiment. The experimental parameters cannot simply be used because atoms in the experiment do not expand by as much as mean-field theory predicts when the blue-detuned lattice is turned on. The explanation for this may be related to the anomalous self-trapping that is the subject of this paper, but a full understanding of that effect will require future work. The suppressed atom expansion during the turn-on of the lattice might also mean that the initial atom correlations are not the same as in the mean-field model.

Assuming that only the lowest band of the 2D optical lattices was populated, a condition that was satisfied in the experiment, we write Ψ in terms of the lowest-band Wannier orbitals as,

$$\Psi = \sum_{m,n} W(x-an)W(y-am)\Phi_{nm}(z,t), \tag{4.2}$$

where Φ_{nm} is the order parameter describing the tube centered at lattice site $\{n,m\}$, and $N_{nm}(t) = \int dz|\Phi_{nm}(z,t)|^2$ is its corresponding atom number. The normalization condition $\sum_{n,m} N_{nm} = N$ with N the total number of atoms, is satisfied.

By assuming $\Phi_{nm}(z,t) = \psi_{nm}(t)\phi_{nm}[z,N_{nm}(t)]$ with $\int dz\,|\phi_{nm}[z,N_{nm}(t)]|^2 = 1$ and $N_{nm} = |\psi_{nm}(t)|^2$ and using a similar variational method to the one described in Appendix D, we can obtain the following effective Hamiltonian

$$\begin{aligned} H_{eff} &= N\left[-4J + \frac{9}{25}U_{eff}\left(\frac{2}{\pi r^2}\right)^{2/3} N^{2/3}\right] \\ &= N\left[-4J + \frac{9}{25}U\rho a^3\right], \end{aligned} \tag{4.3}$$

where r is the width of the wave packet in the lattice directions (in the lattice units). Here we have defined the 2D interaction strength as $U = \frac{g}{a}\int dxdy\; W^4(x)W^4(y)$. $U_{eff} = \left(\frac{9M\omega_{||}^2 a^2 U^2}{32}\right)^{1/3}$ plays a similar role as U_α in the Appendix D, and $J = \int dx\; W(x-a)\left[\frac{\hbar^2}{2M}\frac{\partial^2}{\partial x^2} - V_{lat}\right] W(x)$. $\rho = \frac{3}{4a^3}\left(\frac{2N}{r^2\pi}\right)^{2/3}\left(\frac{2M\omega_{||}^2 a^2}{3U}\right)^{1/3}$ is the 3D density at the center of the cloud. Based on the variational method, we predict that the MQST in the 2D optical lattice should take place when $U\rho a^3/J \geq \frac{100}{9}$.

Although the variational method roughly describes the global dynamics and gives the threshold value ρ of the MQST, it only explicitly accounts for the expansion dynamics across the lattice but not along the tube's direction. We first tried to adapt the variational methods to capture the expansion in both directions. For that purpose, we assumed the density profile along each tube $\phi_{nm}(z,t)$ to have either a Thomas-Fermi (TF) or a Gaussian shape with a width $R_{nm}(t)$ and a phase $\delta_{nm}(t)$. In the lattice direction, on the other hand, the evolution of the amplitudes $\psi_{nm}(t)$ at each lattice site was numerically computed. Unfortunately, we found that it was quantitatively accurate only at very short times. The reason is that (in the experiment) atoms in the tubes rapidly expanded vertically with a number-dependent expansion rate. Since the atoms tunneled between neighboring tubes at the same time, these two processes destroyed the assumed Gaussian or TF shape in each tube and the ansatz broke down.

Since the variational method failed, we instead numerically solve for the axial dynamics. We neglect any temporal dependence of the Wannier functions, which is justified because the interwell number/phase dynamics are much faster than the time associated with the change in shape of such functions. Generically, the wave field $\Psi(\vec{x},t)$ can still be written in terms of Eqn. (4.2), so we keep $\Phi_{nm}(z,t)$ as an arbitrary function. After integrating out the lattice directions, we obtain the following nonlinear Schrödinger equations and solve them numerically.

$$\begin{aligned} i\hbar\dot{\Phi}_{nm}(z,t) = \quad & \left[-\frac{\hbar^2}{2M}\frac{\partial^2}{\partial z^2} + V_{\text{dip}}(an,am,z) + Ud|\Phi_{nm}(z,t)|^2\right]\Phi_{nm}(z,t) \\ & -J\left[\Phi_{n+1,m}(z,t) + \Phi_{n-1,m}(z,t) + \Phi_{n,m+1}(z,t) + \Phi_{n,m-1}(z,t)\right]. \qquad (4.4) \end{aligned}$$

To characterize the MQST, we numerically compute the root mean square (RMS) transverse width, x_{rms}, of a vertical slice of the cloud centered at $z = 0$ and with a width corresponding to

$\pm 10\%$ of the total axial width (characterized by the Thomas-Fermi radius, R_z). The reason for selecting a slice instead of integrating over the whole cloud is to consider a sample of approximately constant density. Theoretically, x_{rms} is directly calculated as: $x_{rms} = a\sqrt{\sum_m \rho_m m^2 / \sum_m \rho_m}$, where $\rho_m = \int_{-Rz/10}^{Rz/10} dz \sum_n |\Phi_{nm}(z,t)|^2$.

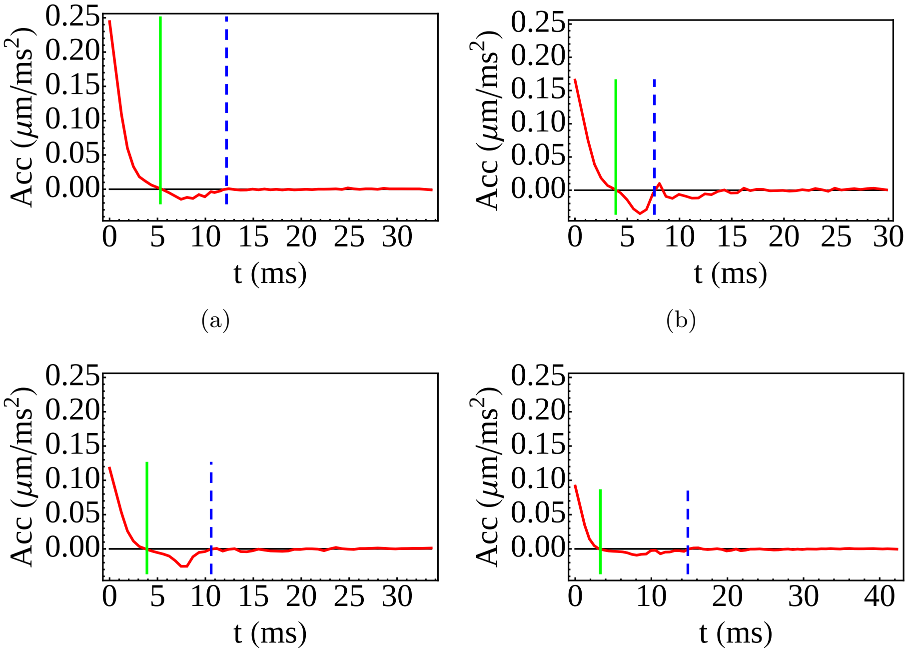

(a)

(b)

(c)

(d)

Figure 4.2: The acceleration of x_{rms} ($\ddot{x}_{rms}$) obtained from the mean-field calculations for all lattice depths used in the experiment: (a) 7.25 E_R, (b) 9.25 E_R, (c) 11 E_R and (d) 13 E_R. From the sign of $\ddot{x}_{rms}$, the evolution can be separated into three different regimes indicated by a solid green line and a dashed blue line. The three regimes are discussed in detail in the text. MQST is signaled in the x_{rms} as a negative acceleration. It starts at the solid green line and stops at $\sim t_c$ (indicated by the dashed blue line) when the acceleration curves cross 0 from below. The values of $U\rho(t_c)/Ja^3$ for the four depths under consideration at t_c are $\{0.4, 3.0, 3.0, 3.0\}$. Those correspond to $\rho(t_c)/J = \{60, 350, 320, 300\}$ $\mu\text{m}^{-3}E_R^{-1}$, respectively.

The expansion along the tubes makes MQST a time-dependent phenomenon, since as the atoms freely expand, the density decreases with time until the system becomes too dilute to sustain self-trapping. To determine the critical value of ρ/J at which MQST stops, we numerically calculate $\ddot{x}_{rms}$. We construct an approximation function that interpolates the numerical values of $x_{rms}(t_i)$ at recorded time t_i. As shown in Fig. 4.2, the curves of $\ddot{x}_{rms}$ are not completely smooth, especially

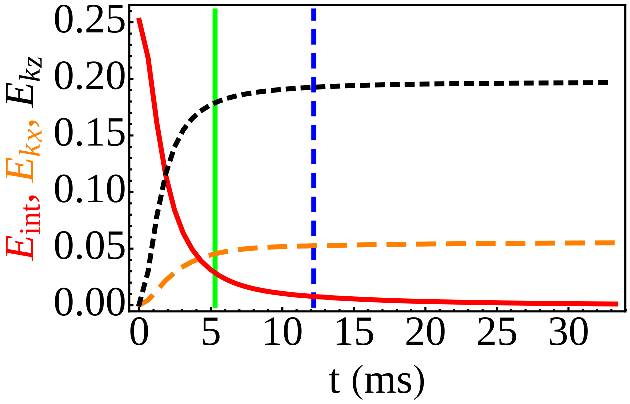

Figure 4.3: Time evolutions of: the kinetic energy along the lattice direction (E_{kx}, dashed orange line), the kinetic energy along z (E_{kz}, dotted black line), and the interaction energy (E_{int}, solid red line). Here energy is in units of E_R. This plot is computed using the mean-field model for a 7.25 E_R lattice. The vertical lines are at the same positions as in Fig. 4.2 (a).

at long times, because of accumulated numerical errors. We define the critical time t_c to be the time when the acceleration first crosses zero from below, i.e., it is negative for times shorter than the critical time due to the MQST (See Fig. 4.2). Note that t_c as well as $\rho(t_c)/J$ are only roughly estimated.

The variational method gives the criterion, $U\rho(t_c)/Ja^3 \approx 11$. Numerically, we found $U\rho(t_c)/Ja^3 = \{0.4, 3.0, 3.0, 3.0\}$ for lattice depths 7.25, 9.25, 11 and 13 E_R, which correspond to $\rho(t_c)/J = \{60, 360, 320, 300\}$ μm^{-3} E_R^{-1}, respectively. Although the numerical values of $\rho(t_c)/J$ are smaller than the value predicted by the variational method, they are almost constant, except for the one associated to the 7.25 E_R curve, consistent with the general concept of a self-trapping threshold.

There are three distinct regimes clearly observed in $\ddot{x}_{rms}$ that we use to characterize the dynamics. We will discuss those different regimes in detail below.

4.3.2 General behavior: Three different regimes

Based on the sign of $\ddot{x}_{rms}$, we classify the dynamical evolution of the system into three different regimes: Initial expansion (Exp), MQST, and Ballistic expansion (BE). Each regime has a distinct behavior that can be further characterized by other observables such as the ratio between

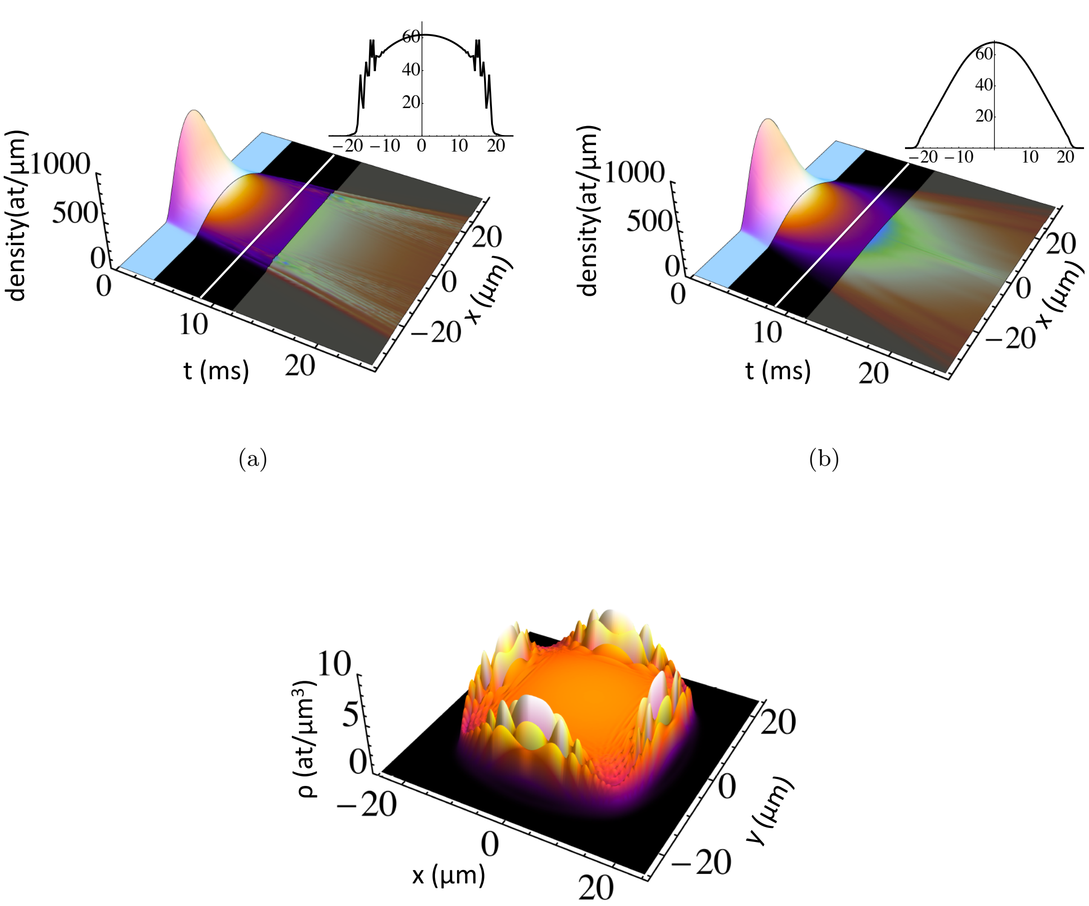

(a)

(b)

(c)

Figure 4.4: Expansion dynamics predicted by mean-field calculations for the lowest lattice-depth (7.25 E_R): Panel (a) displays the evolution of the density profiles at $z = 0$, after integrating along one transverse direction. Panel (b) displays the same density profiles, but after integrating along a direction that is 45 degrees between the x and y axes (as done in the experiment). Panel (c) shows transverse density profiles at $z = 0$, during the MQST regime at $t = 8.7$ ms. The insets in Panel (a) and (b) are intersecting profiles at $t = 8.7$ ms marked by white lines in the 3D density plots and have the same units as in the 3D plots.

interaction and kinetic-energies (Fig. 4.3) and the shape of the density profile (See Fig. 4.4).

- *Initial expansion (Exp)*:

The initial expansion regime describes early times during which the atoms at the center of the cloud expand transversely. We determine this regime by looking at the time period over which the transverse RMS width of the cloud expands with a nonlinear rate (positive acceleration, $\ddot{x}_{rms} > 0$). During this time, the density-profile remains smooth. The interaction energy decreases very rapidly and is converted into kinetic energy along the axial and transverse directions. In contrast to a noninteracting system, in which the initial potential energy in the trap is converted to kinetic energy while the width of the quasi-momentum distribution stays constant, the mean-field interactions cause a broadening of the quasi-momentum distribution whose width grows until it reaches values of quasi-momenta at which the effective mass becomes negative. At this point, sharp peaks in the density profile develop.

For the 7.25 E_R lattice, the initial-expansion takes place within the first 5ms [See Fig. 4.2 (a)] after the parabolic-confinement is turned off. In Fig. 4.4 (a) and 4.4 (b), we also show the time evolution of a horizontal slice of the cloud $z = 0$, after having integrated along one transverse direction (along x), and a direction 45 degrees from the transverse direction (45 degrees from x and y), which is the line of sight direction in the experiment.

- *Macroscopic Quantum Self-Trapping (MQST):*

At intermediate times ($t \sim 5 - 12$ ms for the lowest lattice depth) MQST is signaled by the RMS width of the cloud. During the MQST, regime the interaction energy decreases slowly and remains comparable to the kinetic energy of the atoms in the lattice. The interplay between interatomic interactions and the atomic density gradient at the cloud edges prevents atoms from tunneling outward. In this regime, the atoms start to pile up at the edges, and a hole forms at the center of the cloud [see Fig. 4.4 (c)]. The radial expansion slows-down, or even stops, as illustrated by a negative x_{rms} acceleration. The slowing down can also be linked to the population of a large number of quasi-momentum states with negative effective mass.

Global observables, such as the RMS width are easily measured and characterized. They encode some important signatures of MQST. However, MQST is an inherently local effect, and important information can be hidden in the global probes. For example, although the formation of steep edges and a hole is shared by the MQST phenomena in both 1D and 2D lattices and is observable in the RMS width, there are more features in the 2D system.

In the MQST regime, the atom distribution in the lattice is no longer smooth, and its profile evolves from having a circular shape to a square one. Atoms at 45^o to the lattice axes are only self-trapped at larger radii, since the corresponding density gradients are smaller than in the lattice directions. This gives rise to the square fort-like barrier around the edges, as seen in Fig. 4.5. The formation of steep edges also happens in the 1D system, but in 2D there is always a direction along which atoms can tunnel. Since they are not fully frozen, the self-trapped edges are not stationary as in the 1D case, but instead they evolve with time.

The shape of the integrated-density distribution strongly depends on the direction along which the integration is performed [See Fig. 4.4(a) and Fig. 4.4 (b)]. For example, while the peaks at the edges, signaling the hole at the center of the cloud, are clearly visible in Fig. 4.4 (a), when the imaging direction is along the lattices, they are barely visible when the imaging direction is along the diagonals as in Fig. 4.4 (b).

- *Ballistic Expansion Regime (BE):*

Because atoms expand axially along the tubes, the interatomic interactions decrease as time evolves, and at some point, they are no longer strong enough to enforce the self-trapping mechanism. This determines the interruption of the MQST and the onset of the ballistic regime. In this regime mean-field interactions have decreased so significantly that an analysis in terms of single-particle eigenstates and eigenmodes can be carried out.

4.3.3 Comparison with experiment

The experimentally measured RMS widths are slightly different from the x_{rms} defined above. In the experiment, the density-square distribution, instead of the density, was directly measured. To mimic the RMS widths measured in the experiment, we define another RMS width, denoted as

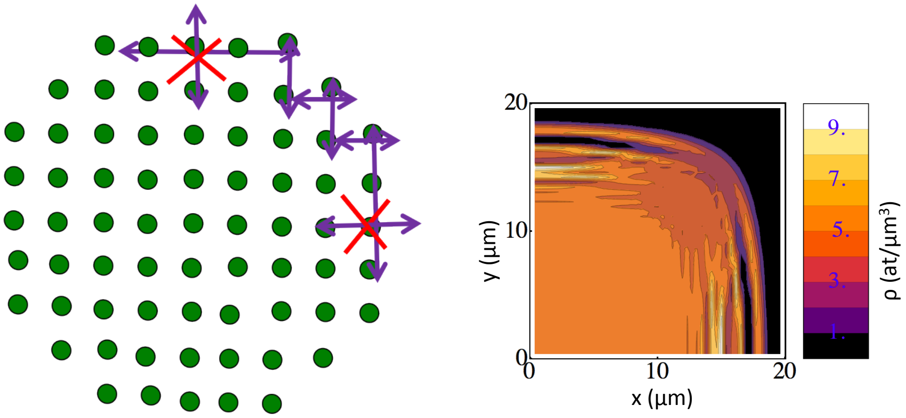

(a)

(b)

Figure 4.5: Panel (a) is a schematic picture of the tunneling in 2D optical lattices. In 2D, no site is self-trapped in all directions, so atoms are not fully frozen. The arrows show the directions that atoms may tunnel, while the crosses mean that tunneling along those directions is forbidden by MQST. Panel (b) is a density (ρ at $z = 0$) contour plot of a square fort-like barrier developed during the MQST regime.

σ_{n^2}. To get σ_{n^2}, we square the 1D distribution ρ_m (ρ_m is obtained by integrating the 3D density distribution along a line 45 degrees from a lattice direction over a slice centered at $z = 0$) and convolve it with a Gaussian of RMS width 1.7 μm (the imaging system resolution) to get the convolved-density-square distribution, n_m^2 or $\tilde{\rho}_m$. The convolution procedure mimics the finite-size resolution of the imaging system. Finally, σ_{n^2} is directly calculated by the definition: $\sigma_{n^2} = a\sqrt{\sum_m \tilde{\rho}_m m^2/\sum_m \tilde{\rho}_m}$. This process removes fine features from the theoretical curves that are not resolvable in the experiment.

Another observable measured in the experiment was the Thomas-Fermi radius R_z of the atomic density along z. It was obtained by fitting the atomic density distribution, after integrating along the transverse directions, to $\frac{3}{4R_z}\max[0, 1-(z/R_z)^2]$. Because the initial width of the cloud is sensitive to the loading procedure and because the mean field treatment tends to overestimate the initial width of the cloud compared to the one measured in the experiment, we use different initial sizes to compare with the experiment, subject to the constraint of matching axial expansion rates at long times. The latter just ensures that we are using the correct total energy, which is conserved during the evolution. Comparisons between the numerical simulations and the experimental data are shown in Figs. 4.6 and 4.7. In general, the theory overestimates the expansion rate of the RMS widths. Only for 7.25 E_R does the mean-field theory roughly capture the experimental observations at short times. For deeper lattice depths, such as 13 E_R, the mean-field theory fails to reproduce the observed dynamics.

The long-time dynamics of σ_{n^2} predicted by the mean-field method is sensitive to the initial width of the cloud. When the initial RMS width is larger, the MQST boundary is further away from the center, and thus it takes more time for the RMS width to reflect the presence of MQST at the edges. In contrast, the MQST is more visible for smaller initial RMS widths, as shown in Figs. 4.6 and 4.7.

The plots in Fig. 4.4 share the same initial condition as the dashed blue line in Fig. 4.6. With this initial condition, the MQST effect is weak and the self-trapping signatures, such as peaks at the edges [Fig. 4.4 (a)] and a hole in the middle [Fig. 4.4 (c)], are not very pronounced. These self-trapping signatures were not seen in the experiment even when imaged from above. These characteristic signatures might be visible in future experiments with smaller lattice depths, smaller initial RMS widths, and larger values of R_z.

4.4 Beyond mean-field model

As shown in Sec. 4.3, the mean-field treatment does not correctly describe the experiment. A fundamental limitation of this treatment is that it assumes all the atoms are in the condensate and neglects condensate depletion due to quantum correlations or thermal fluctuations (coming from an initial thermal component or nonadiabatic effects as the lattice is turned on). Condensate depletion modifies the dynamics predicted by the single mode approximation.

One way to quantify the role of quantum fluctuations is to view the system as an array of approximately one-dimensional Bose gases. 1D Bose gases are typically characterized by the dimensionless parameter γ [91], the ratio of the mean-field interaction energy per particle calculated without correlations to the kinetic energy calculated with maximal correlations. In a cigar-shaped

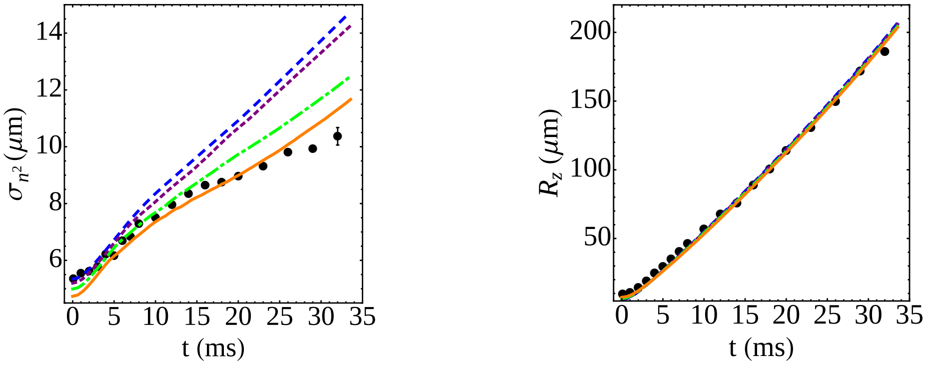

(a) (b)

Figure 4.6: The evolution of (a) σ_{n^2} and (b) R_z for $7.25 E_R$ from mean field calculations and the experiment. Each black point is the average of 10 experimental measurements. In Panel (a), the error bars represent random uncertainty, but an overall systematic uncertainty of 0.5μm associated with the imaging resolution is not included. To illustrate the dependence of the mean-field dynamics on the initial width, we show the evolution of σ_n^2 for different initial conditions for the $7.25 E_R$ lattice. Each line corresponds to a particular initial condition, subject to the constraint of matching axial expansion rates at long times. In Panel (b), error bars are not shown, since we are mainly interested in the long-time dynamics when R_z is very large and the error bars are negligible. Even with different initial conditions, the expansion rates along z are almost the same, therefore in Panel (b) all lines are almost on top of each other.

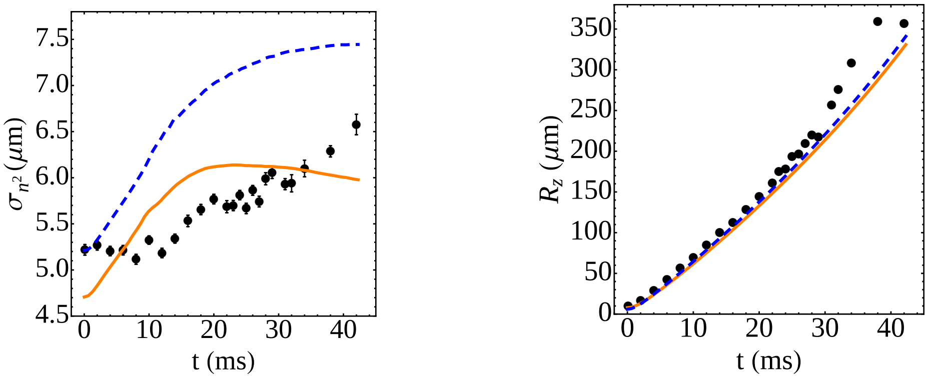

(a) (b)

Figure 4.7: Time evolution of (a) σ_{n^2} and (b) R_z for 13 E_R from mean-field calculations and the experiment. As in Fig. 4.6, the solid and dashed lines are simulation results, and each corresponds to a particular initial condition. The long-time dynamics of σ_{n^2} are sensitive to the initial width of the cloud also at 13 E_R. The black points are experimental data.

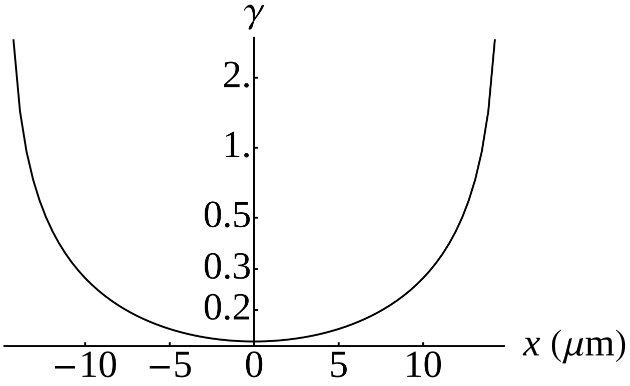

Figure 4.8: Dimensionless coupling strength at $t = 0$ as a function of tube location along the y axis, if the tubes are approximated to be independent. Here $V_0 = 13\ E_R$. The approximation is never fully warranted in the regime of this work, where the tubes are manifestly not independent. Still, we suspect that this γ gives a sense of the initial axial correlations in the relatively deep lattices.

trap ($\omega_\perp \gg \omega_z$), $\gamma = \frac{2}{n_{1D}|a_{1D}|}$ is inversely proportional to the one-dimensional gas parameter $n_{1D}|a_{1D}|$, where n_{1D} is the one-dimensional number density of particles, and $a_{1D} \approx -\frac{a_\perp^2}{2a_s}$ is the one-dimensional scattering length. Here $a_\perp = \sqrt{\frac{\hbar}{\mu\omega_\perp}}$ is the size of the ground state in the transverse direction, and $\mu = \frac{M}{2}$ is the reduced mass of two colliding particles. A weakly interacting 1D gas ($\gamma \ll 1$) is well described by mean-field theory. In contrast, in the strongly interacting regime, $\gamma \gg 1$, atoms avoid each other to reduce mean-field energy, and the bosons behave like noninteracting fermions [89].

In this approximate treatment of each tube as an independent 1D system, for 7.25 E_R, 9.25 E_R, 11 E_R and 13 E_R, the corresponding γ values at time $t = 0$ in the central tubes (around $z = 0$) are 0.088, 0.115, 0.132 and 0.144 and increase monotonically from the centers to the edges. To be more specific, in Fig. 4.8, we plot γ as a function of tube position for this idealized scenario of independent tubes and find that γ can become larger than one at the edges.

The values of γ are not small even at time $t = 0$, particularly at the edges where MQST is expected to take place. Moreover, they are expected to increase at short times because of the rapid decrease in density along each tube caused by the axial expansion. This observation is consistent with the failure of the mean-field GP equation to describe the dynamics and the need to account for beyond mean-field corrections. The latter is especially true for deeper lattices, for which the picture of an array of 1D tubes is more appropriate. For lattices shallower than the ones used in the current experiment, tunneling between tubes is expected to become significant. In this case the system must be treated as a three-dimensional object. In 3D, quantum correlations are less relevant and a pure mean-field analysis should correctly describe the dynamics.

At longer times, the system has expanded so much that the probability of having two particles close to each other becomes negligibly small, and a pure single-particle analysis of the dynamics becomes accurate. Note, however, that even in this regime a quantitative analysis is still not trivial, since the state of the gas in the ballistic regime depends on the conditions at the time at which correlations become irrelevant.

In an attempt to include quantum fluctuations, we use an approximate TWA [66, 92, 93]. The TWA incorporates leading-order corrections to the dynamics expanded around the classical (GPE) limit. The whole idea of the TWA is that the expectation value of a quantity at time t can be determined by solving the classical equations of motion from 0 to t and sampling over the Wigner distribution at time $t = 0$. The TWA is guaranteed to be accurate at short times. For longer times, there are also higher-order corrections to the classical trajectories. In a 3D lattice (0D condensate in each well) there are two limiting regimes where the Wigner function can be easily found and has been shown to capture the exact dynamics well [66]. One is the very weakly interacting regime in which the system is almost an eigenstate of the noninteracting Hamiltonian, a product of coherent states. The other case is the strongly interacting regime with commensurate filling, in which the system is a Mott insulator. In this case the many-body wave function is mostly a product Fock state $\prod_{j=1}^{L} |n\rangle_j$ with n the filling factor. The semiclassical wave function is $\prod_{j=1}^{L} \sqrt{n} \exp(\mathrm{i}\phi_j)$ and the corresponding Wigner function is characterized by independent random variables ϕ_j uniformly distributed between 0 and 2π.

The case that we are dealing with now has the complication that not only is it in the intermediate regime where neither of the two limiting cases holds, but also instead of a 0D condensate within a lattice site, we have a quasi-1D gas. Finding the Wigner function therefore is not a trivial task. Prior work done for two-coupled 1D tubes [94] has already shown the importance of taking into account quantum correlations for the proper characterization of the dynamics. Consequently, we expect that beyond-mean-field corrections will play an important role in our system.

With this goal in mind and subject to the limitation that the pure mean-field dynamics involve the propagation of thousands of coupled GPEs, we implement the TWA in an ad-hoc way that we refer to as aTWA. We account for initial phase fluctuations within each tube by adding random phase factors: $\phi_{nm}(t=0) \rightarrow \eta\theta_{nm}$, where θ_{nm} is a uniformly distributed random variable between 0 and 2π, and η parameterizes the strength of the phase fluctuations. When $\eta = 0$, the initial conditions correspond to a fully coherent array of 1D gases, and when $\eta = 1$, we have an initially fully incoherent array. $0 < \eta < 1$ corresponds to a partially coherent array. Since η is not determined in the theory, we compare the results for different η to experiment, and choose the most similar one. We average the results over at least 20 initial configurations.

Besides phase fluctuations, we also study the effect of including number fluctuations in the initial conditions. The results obtained using the aTWA are described in detail in the following subsections.

The aTWA considerably improves the agreement between theory and experiment. The value of η that optimizes the agreement with the experiment increases with increasing lattice depth. This is expected, since as tunneling between tubes becomes weaker, phase coherence is suppressed. The noise introduced by those random phases quickly generates local self-trapping everywhere, suppressing the transverse dynamics until, because of the axial expansion, interactions drop so significantly that the system goes to the ballistic expansion regime. Noise also tends to suppress the hole formation. See Fig. 4.9.

4.4.1 Comparison between theory and experiment: phase fluctuations

Phase fluctuation among tubes substantially suppresses the expansion dynamics. To illustrate this effect, consider the toy model of a double well with initial relative phase difference $\phi(0)$. The

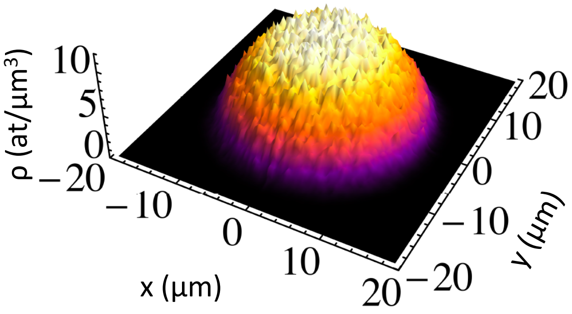

Figure 4.9: Transverse density profiles at $z = 0$ during the MQST regime at $t = 8.7$ ms for the 13 E_R lattice obtained from the aTWA results.

critical value of Λ (Λ is proportional to the ratio of the on-site interaction energy and the tunneling matrix element between two wells, see the Appendix D for details) that determines the MQST-to-diffusive transition depends on ϕ as [80],

$$\Lambda_c = 2\left(\frac{\sqrt{1-z(0)^2}\cos[\phi(0)]+1}{z(0)^2}\right), \tag{4.5}$$

where z is the fractional population difference between the two wells, and $z = \frac{N_L - N_R}{N_L + N_R}$. In this case, one can see that even when the initial population imbalance is small, $z(0) \ll 1$, the system can become self-trapped if $\phi(0) \to \pi$ ($\Lambda_c \to 1$).

Our simulation agrees with this expectation. Fig. 4.10–4.11 show the transverse RMS σ_{n^2} and the vertical Thomas-Fermi radius R_z. The aTWA treatment agrees much better with experimental observations, especially for the deepest lattices. In Fig. 4.10, we can see that the greater the η, the slower is the expansion rate of σ_{n^2}. When $\eta = 1$, i.e., when the phase fluctuations are maximal, the expansion rate of σ_{n^2} reaches its smallest value.

Although the modeled curves with the appropriate η are never too far from the data, for $V_0 \geq 11\ E_R$, the experiment shows a more delayed and more sudden onset of ballistic expansion than the model. For $V_0 = 7.25\ E_R$, $\eta \approx 0.4$ best fits the early evolution, when there is MQST. For larger V_0, $\eta = 1$ clearly fits best for the short evolution time. For $V_0 = 7.25\ E_R$, $\eta \approx 0.4$, the three regimes predicted by the pure mean-field model are still visible, although $\ddot{x}_{rms}$ becomes barely negative in the MQST regime. On the other hand, for the deeper lattices, the random initial phases cause a fast development of site-to-site density fluctuations and the formation of localized domains randomly distributed throughout the tube array. In contrast to the pure mean-field model, localization occurs without the formation of sharp edges, there is no reflection from them, and $\ddot{x}_{rms}$ never becomes negative. Instead, $\ddot{x}_{rms}$ asymptotically approaches zero from above as shown in Fig. 4.12. MQST always disappears when the density drops below a critical value that depends on V_0. The model predicts the following values for the transition to a ballistic regime, $\rho(t_c)/J = \{840, 1900, 1970\}\ \mu\text{m}^{-3}E_R^{-1}$ for $V_0/E_R = \{9.25, 11, 13\}$. We can compare these values

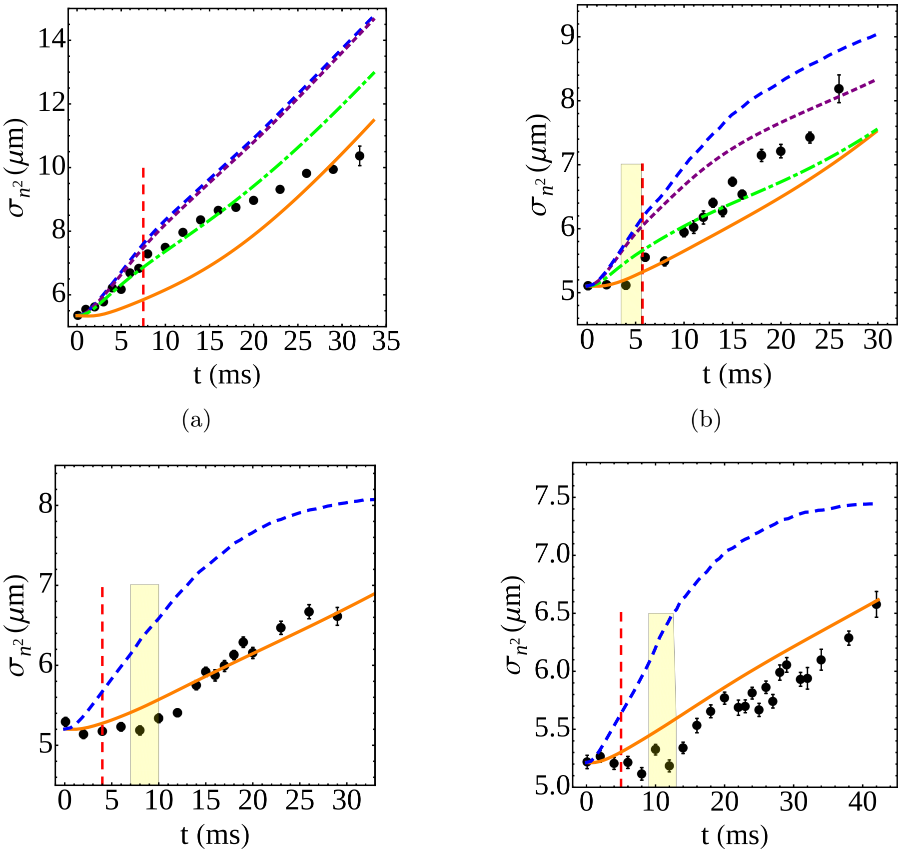

(a) (b) (c) (d)

Figure 4.10: Mean-field, aTWA, and experimental results for the evolution of σ_n^2 for all lattice depths used in the experiment. The lattice depths are (a) 7.25 E_R, (b) 9.25 E_R, (c) 11 E_R and (d) 13 E_R. At low lattice depth, a small η seems to account for the observed behavior at short times. The dashed blue line is the result of a mean-field calculation of the dynamics with no random phase between the tubes ($\eta = 0$). The dotted purple line is for $\eta = 0.2$, the dashed-dotted green lines are for (a) $\eta = 0.4$ and (b) $\eta = 0.5$, and the solid orange line is for $\eta = 1$. The dashed-vertical red lines indicate the transition from MQST to BE predicted by the aTWA. The yellow shadow regions indicate the t_c inferred from the experimental data.

Figure 4.11: Evolution of R_z for all lattice depths used in the experiment. The dots show experimental data, and the solid and dashed lines show the predictions obtained from the aTWA for different η. The lattice depths are (a) 7.25 E_R, (b) 9.25 E_R, (c) 11 E_R and (d) 13 E_R. R_z is obtained by fitting the density along z to a Thomas-Fermi profile. The theoretical curves use the same parameters as the ones shown in Fig. 4.10.

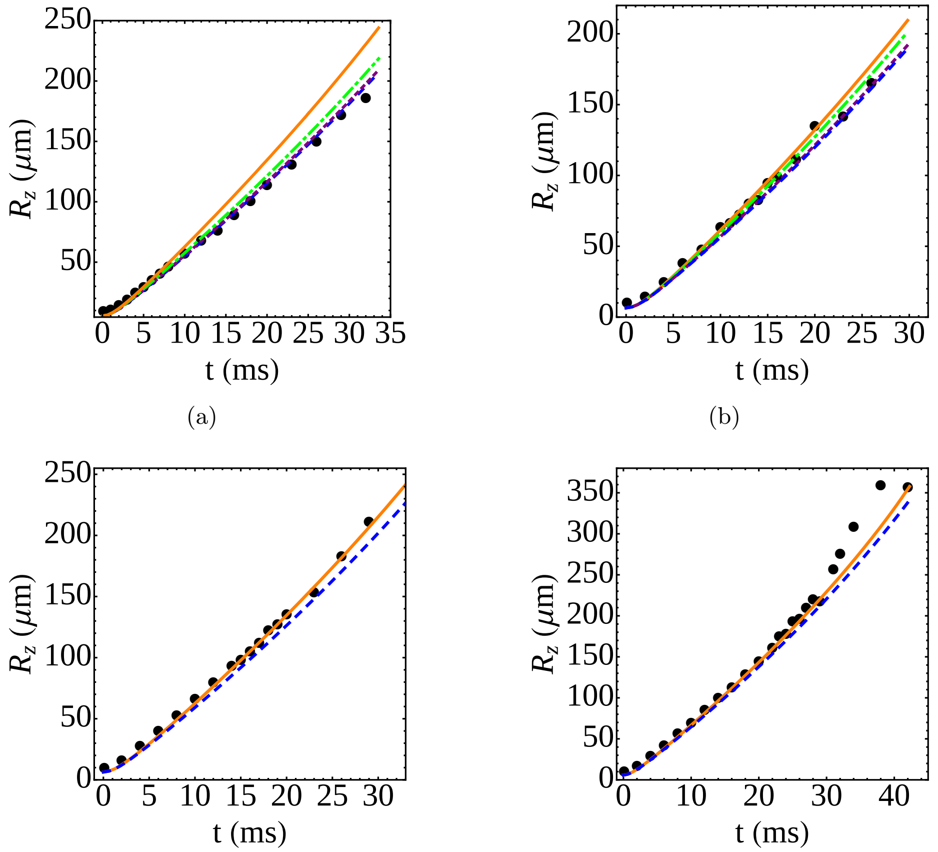

(a) (b) (c) (d)

Figure 4.12: $\ddot{x}_{rms}$ calculated using the aTWA for different lattice depths and for the corresponding optimal η, (a) 7.25 E_R, $\eta = 0.4$ and (b) 13 E_R, $\eta = 1$. The boundaries between MQST and BE are indicated by the dashed blue lines. In panel (a), the boundary between EXP and MQST is indicated by the solid-vertical green line. In panel (b), because $\ddot{x}_{rms}$ is almost 0 at all times, it can be interpreted that the self-trapping starts at $t = 0$ ms.

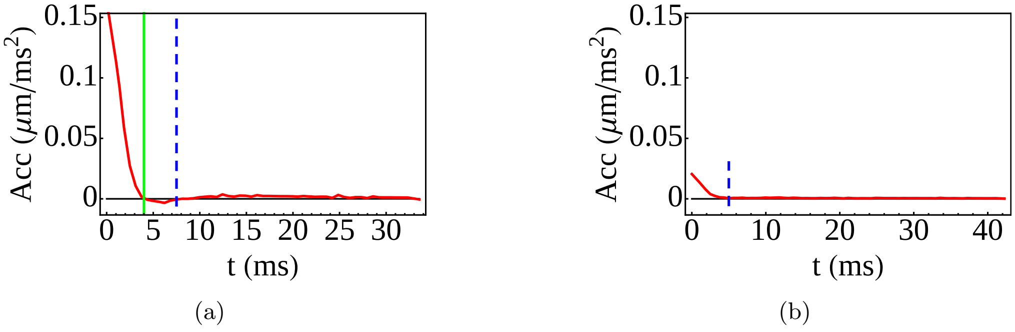

(a) (b)

Figure 4.13: Transverse density profiles: The solid and dashed lines are obtained from the aTWA results for the $V = 7.25\ E_R$ lattice and for $\eta = 0.4$. The profiles are taken at $z = 0$ and viewed transversely at an angle 45^o from the lattice axis and normalized to 1. The solid blue lines indicate the theoretical profiles before convolution, and the dashed black lines after convolution. The red points are averaged experimental data of 10 measurements.

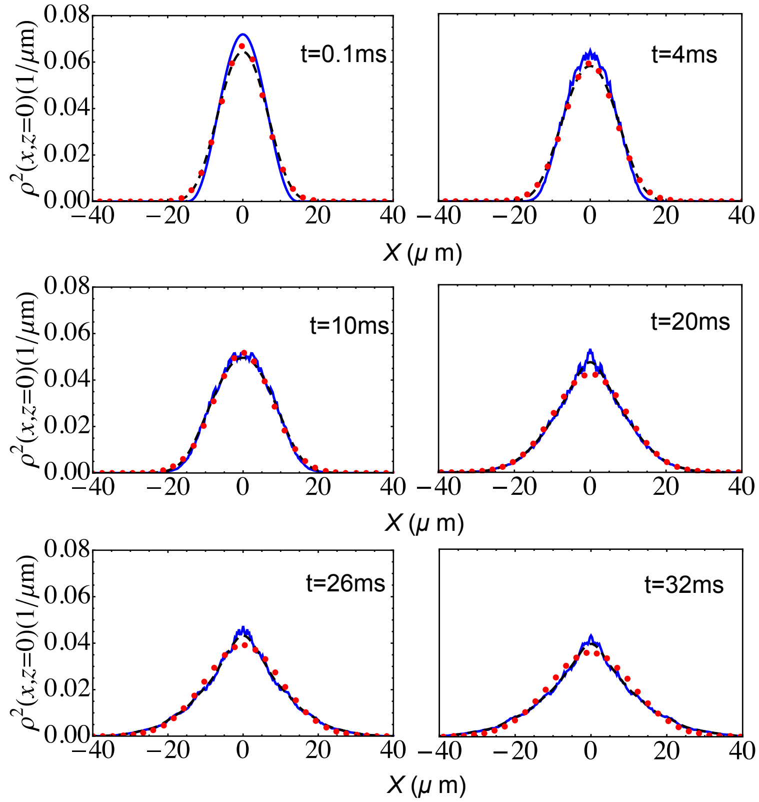

Figure 4.14: Transverse density profiles: The solid and dashed lines are obtained from the aTWA results for the $V = 13\ E_R$ lattice and for $\eta = 1$. The profiles are taken at $z = 0$ and viewed transversely at an angle 45^o from the lattice axis and normalized to 1. The solid blue lines indicate the theoretical profiles before convolution and the dashed black lines after convolution. The red points are averaged experimental data of 10 measurements.

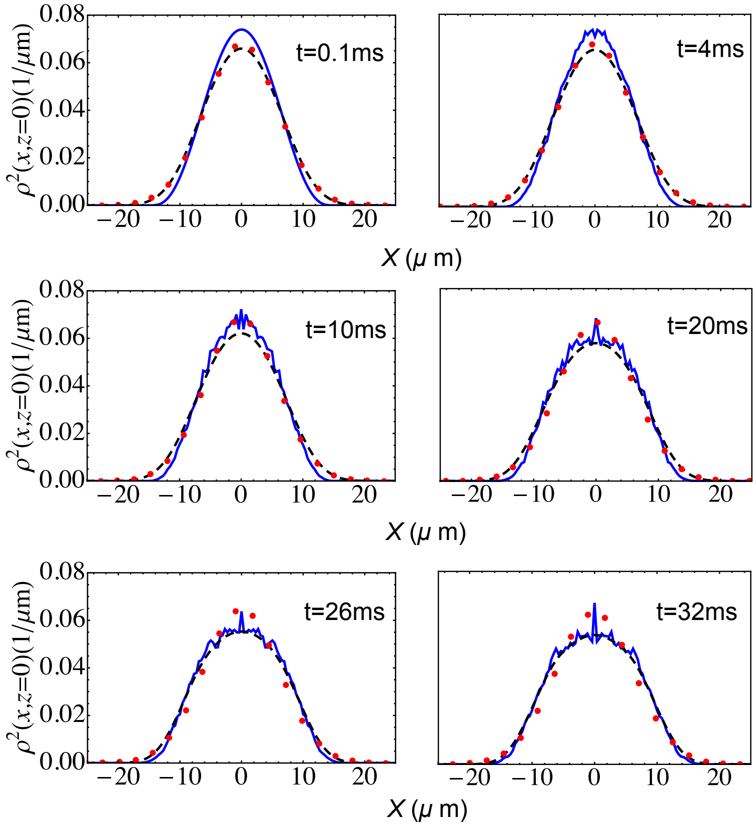

with the ones measured in the experiment that occur when the ratio $\rho(t_c)/J = \{1190 \pm 310, 860 \pm 190, 910 \pm 210\}$ $\mu\text{m}^{-3}E_R^{-1}$ for $V_0/E_R = \{9.25, 11, 13\}$, respectively. We can see that the ratio of $\rho(t_c)/J$ in the experiment is roughly constant. However, while the values of $\rho(t_c)/J$ predicted by the aTWA are almost the same for 11 E_R and 13 E_R, $\rho(t_c)/J$ for 9.25 E_R is only half of that value. On the other hand, the actual $\rho(t_c)/J$ value predicted by the aTWA at 9.25 E_R is closer to the observed value.

Figures 4.13–4.14 show the density profiles measured experimentally for the shallowest and deepest lattices and the corresponding theoretically computed profiles. For the 7.25 E_R lattice, one can see a good agreement after the theory curves are convolved to account for the imaging system resolution. However, the theoretical distributions are not well fitted by a Gaussian at longer times. The experimental distributions, on the other hand, always retain a Gaussian profile. In general, phase fluctuations prevent the hole formation and help to keep the density distributions closer to a Gaussian profile.

4.4.2 Number fluctuations

So far we have included only phase fluctuations. However, we know that in the superfluid regime, relative atom number fluctuations provide the dominant beyond-mean-field corrections. To investigate the role of number fluctuations in the expansion dynamics, we introduce number fluctuations in the initial conditions. We implement this by allowing $\approx 1/\sqrt{N_{nm}}$ fluctuations in the atom number in each tube, with $N_{nm}(0)$ being the total number of atoms in a tube centered at $\{n, m\}$. We focus on the case $V_0 = 7.25$ E_R. The results are shown in Fig. 4.15, where we can see that number fluctuations do suppress the expansion rate of the cloud, but by only a small amount.

4.4.3 Phase and number fluctuations

In the intermediate regime—between the superfluid and Mott phases—both quantum and number fluctuations are relevant, but constrained by the corresponding Heisenberg uncertainty

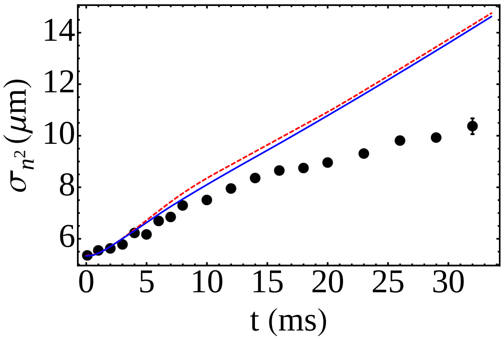

Figure 4.15: Time evolution of σ_{n^2} computed for a 7.25 E_R lattice, and for $\eta = 0$. The dashed red line shows the result when number fluctuations are neglected, and the solid blue line shows the result when number fluctuations ($\approx 1/\sqrt{N_{mn}}$) are included. The plot clearly shows that number fluctuations suppress the expansion, but only by a small amount.

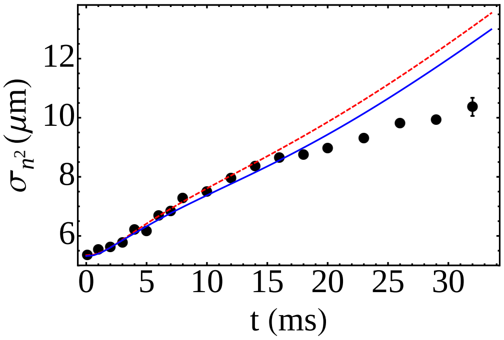

Figure 4.16: aTWA results for the time evolution of σ_{n^2} for a 7.25 E_R lattice, and for $\eta = 0.35$. The dashed red line shows the result when only phase fluctuations are included, and the solid blue line shows the result when both number fluctuations ($\approx 1/\sqrt{N_{mn}}$) and phase fluctuations are included. The plot shows that number fluctuations slightly suppress the initial expansion rate.

relation. To get an upper bound of the amount of localization predicted by the aTWA, we add both number fluctuations ($\approx 1/\sqrt{N_{nm}}$) and phase fluctuations in the initial conditions. The results are shown in Fig. 4.16. Indeed the addition of both phase and number fluctuations helps to suppress the expansion rate of the cloud for moderate η (as in the 7.25 E_R case) but for large η, the addition of number fluctuations is barely noticeable. In other words, the curves with number and phase fluctuations are quite similar to the curves with phase fluctuations only.

In summary, so far we have accounted for the quantum correlations developed in the tubes by adding an overall random phase in a phenomenological way. Although this procedure pushes the theory closer to the experimental observations, a fundamental problem with the aTWA is that it misses the correlations within each tube. Those might be the key ingredient responsible for the observed localization at short times because of the additional energy cost they impose when atoms tunnel from one tube to the next. Those correlations are expected to play a major role at short times when interactions are dominant. A significantly better treatment could be obtained by computing the full Wigner function of the interacting systems. The latter could, in principle, be achieved by starting with the Wigner function of the noninteracting system (which is known) and then by adiabatically increasing the interactions to the desired value. The large number of degrees of freedom in consideration substantially complicates this implementation.

4.5 Beyond the aTWA—two coupled tubes

To test the validity of the various approximations used so far, we now turn to a simplified model system that is amenable to a numerically exact treatment using the t-DMRG. In the following, we will consider a configuration of two-coupled tubes (see Fig. 4.17) and compare the dynamics of this minimal system to the one obtained with the pure GPE and the aTWA methods. To be more specific, we replace in our toy two-tube model the axial parabolic-trapping potential along the tubes by a box potential that is easier to treat numerically, and we create the population imbalance at the beginning of the dynamics by choosing different chemical potentials on the two tubes. We then set the chemical potentials to zero instantaneously to mimic the time evolution in the experiment. Note that when removing the box potential in this setup, the dynamics at the edges of the cloud can dominate the tunneling between the two tubes. Therefore, we find it more convenient to keep the box turned on throughout the time evolution. Moreover, to avoid the complications of dealing with a continuum system, we assume that along each tube there is a weak lattice (with L lattice sites) and use the tight-binding approximation to describe the dynamics.

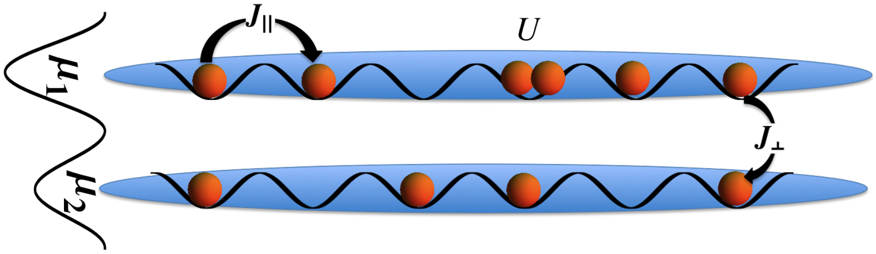

Figure 4.17: Schematic configuration of the two-tube system.

This gives rise to a Bose-Hubbard model,

$$H = -J_\parallel \sum_{l=1,2} \sum_{<i,j>} \left(\hat{a}^\dagger_{l,i} \hat{a}_{l,j} + h.c \right) + \sum_{l,i} \frac{U}{2} \hat{n}_{l,i} (\hat{n}_{l,i} - 1) - J_\perp \sum_i \left(\hat{a}^\dagger_{1,i} \hat{a}_{2,i} + h.c \right) - \sum_{l,i} \mu_l \hat{n}_{l,i}, \quad (4.6)$$

where $\hat{a}^\dagger_{l,i}$ and $\hat{a}_{l,i}$ are bosonic creation and annihilation operators, and $\hat{n}_{l,i} = \hat{a}^\dagger_{l,i} \hat{a}_{l,i}$ gives the number of particles at site i on tube l. $J_\parallel$ is the tunneling matrix element between nearest neighboring sites within each tube, $J_\perp$ is the tunneling matrix element between tubes, U is the on-site interaction strength and μ_l is the chemical potential on tube l ($l = 1, 2$). The difference in chemical potentials $\mu_1 - \mu_2$ equals the bias between the two tubes that is adjusted to obtain the desired population on each of the tubes. Note that we assume tunneling between the tubes takes place at nearest neighbouring sites only, so that we obtain a ladder geometry.

4.5.1 The DMRG method

DMRG is a numerical method that is capable of obtaining ground-state properties of (quasi)one-dimensional systems with very high efficiency and accuracy for lattices with up to several thousand sites. This is achieved by working in a truncated basis of eigenstates of reduced density matrices obtained for different bipartitions of the lattice. The so-called discarded weight, which is the sum of the weights of the density-matrix eigenstates that are neglected and which should be as small as possible [67] quantifies the error of the method. Also, its time-dependent extensions (t-DMRG) can treat the real-time evolution of strongly correlated quantum many-body systems substantially larger than the ones amenable to exactly diagonalizing the Hamiltonian and with an accuracy that

	U $\mathrm{N}_{\mathrm{total}}$	$\mathrm{J}_{\parallel}$	$\mathrm{J}_{\perp}$	L (lattice sites)
case 1	30	1	0.025	40
case 2	30	1	0.05	40
case 3	30	1	0.1	40
case 4	60	1	0.05	40
	$\mathrm{N}_{\mathrm{total}}$	$\mathrm{J}_{\parallel}$	$\mathrm{J}_{\perp}$	L (lattice sites)
case 5	30	1	0.05	40

Table 4.1: Set of parameters and different initial conditions used to study the dynamics. N_{total} is the total particle number in the ladder. U is the on-site interaction strength, $J_{\parallel}$ is the nearest-neighbor tunneling matrix element within each tube, and $J_{\perp}$ is the tunneling matrix element between tubes.

can be, at short and intermediate times, similar to what is achieved in ground-state calculations. Here, we use this accuracy to obtain high-precision numerical results. During the evolution, we aim for a discarded weight of $< 10^{-9}$ and keep up to 500 density-matrix eigenstates for systems with $L = 40$ sites in each tube. We apply a time step of $\Delta t = 0.01/J_{\parallel}$ and find a discarded weight of $\lesssim 10^{-6}$ at the end of the time evolution displayed in the plots.

In the 1D Bose-Hubbard model, $\gamma \approx \frac{U}{J}$. Therefore in our ladder configuration, we will use $\gamma = \frac{U}{J_{\parallel}}$ to quantify the interaction strength of the system. This is expected to be a good characterization when the intertube tunneling is much smaller than the intratube tunneling ($J_{\perp} \ll J_{\parallel}$). We set $J_{\parallel} = 1$ in all cases and vary both γ (by changing U) and the density. Table 4.1 summarizes the set of parameters that we use to study the dynamics. N_{total} is the total particle number in the system.

4.5.2 Short-time dynamics

Even in this simpler two-tube system, the many-body dynamics after a quench can be quite complicated. To compare the differences between results obtained using the mean-field theory, the aTWA, and the t-DMRG, as well as to check the validity of the aTWA, we first focus on the short-time dynamics, for which we can obtain analytical expressions and numerical results.

A quantity that gives relevant information about the system's dynamics is the total particle number in each tube, i.e., $N_l = \sum_i n_{l,i}$ with $n_{l,i} = \langle \hat{n}_{l,i} \rangle$. Heisenberg's equations of motion for the atom number in the tubes then read ($\hbar \equiv 1$),

$$\frac{d}{dt}N_l = -iJ_\perp \sum_i \left(\langle \hat{a}^\dagger_{l',i}\hat{a}_{l,i} \rangle - \langle \hat{a}^\dagger_{l,i}\hat{a}_{l',i} \rangle \right), \tag{4.7}$$

$$\frac{d^2}{dt^2}N_l = -\frac{J_\perp U}{2} \sum_i \langle \left\{ \hat{n}_{l,i} - \hat{n}_{l',i}, \hat{a}^\dagger_{l',i}\hat{a}_{l,i} + \hat{a}^\dagger_{l,i}\hat{a}_{l',i} \right\} \rangle - 2J_\perp^2 (N_l - N_{l'}), \tag{4.8}$$

where $l' \neq l$ denotes the position in either tube 1 or 2.

Generally, for the ground state, $\mathrm{Im}[\langle a^\dagger_{l,i} a_{l',j} \rangle] = 0$ (there are no currents in the system), and therefore the first derivative of N_l is zero at $t = 0$, i.e., $\frac{d}{dt}N_l\big|_{t=0} = 0$.

The second derivative of N_l is generally nonzero when there is a population imbalance between the two tubes, because of the second term on the right hand side of Eqn. (4.8). The first term accounts for the role of interactions in the dynamics and involves four-particle correlation functions, which can play a fundamental role in the dynamics. For strongly repulsive bosons (hard-core bosons), on-site occupancies > 1 are energetically forbidden, so the four-particle correlations vanish. Therefore only the term proportional to the population imbalance contributes to the dynamics. Hence, the dynamics of hard-core bosons are governed by,

$$\frac{d^2}{dt^2}N_l = -2J_\perp^2 (N_l - N_{l'}). \tag{4.9}$$

Analytical expressions for the short-time dynamics can also be obtained using the mean-field (GPE) approximations and the aTWA.

At the mean-field (GPE) level, the operators $\hat{a}_{l,i}$ are replaced with c-numbers $\psi_{l,i}$. At $t = 0$, the ground state corresponds to $\psi_{l,i} = \sqrt{n_{l,i}}e^{i\phi}$, and there is a global phase for all sites. Without loss of generality, $\psi_{l,i}(0)$ can be chosen as $\sqrt{n_{l,i}}$. Under the aTWA, $\psi_{l,i}$ is chosen as $\sqrt{n_{l,i}}$ times a global phase factor for each tube, i.e., $\psi_{l,i}(0) \to \sqrt{n_{l,i}}e^{i\theta_l \cdot \eta}$. As we explained in section 4.4, η is a tunable parameter thatcharacterizes the strength of phase fluctuations, and θ_l is a uniformly distributed random variable between 0 and 2π. The average can be computed analytically, and in the aTWA we obtain that the dynamics is governed by

$$\left.\frac{d^2}{dt^2}N_l\right|_{t=0} = -2J_\perp^2 (N_l - N_{l'}) - 2J_\perp U \frac{N_l - N_{l'}}{L} \sqrt{N_l N_{l'}} \frac{\sin^2(\pi\eta)}{\pi^2\eta^2}. \tag{4.10}$$

	η for case 1	η for case 2	η for case 3	η for case 4	η for case 5
U=1	0.31	0.30	0.30	0.27	0.30
U=2	0.46	0.45	0.46	0.39	0.39
U=3	0.56	0.56	0.57	0.48	0.45
U=5	0.69	0.70	0.71	0.61	0.54

Table 4.2: Fitted values of η for different set of parameters used to investigate the dynamics: at short times the t-DMRG dynamics are well captured by the aTWA when η is used as a fitting parameter.

The second term in the above equation equals $-2J_\perp U\frac{(N_l-N_{l'})}{L}\sqrt{N_lN_{l'}}$ when $\eta = 0$ and goes to 0 when $\eta = 1$, agreeing with the GPE and hard-core boson limits. Since $\frac{d}{dt}N_l\big|_{t=0} = 0$, to lowest order, $N_l(t) = \frac{1}{2}\left(\frac{d^2}{dt^2}N_l\big|_{t=0}\right)t^2 + N_l(0)$ at short times. Numerically, we can either directly calculate $\frac{d^2}{dt^2}N_l\big|_{t=0}$ from the initial wave-function at $t = 0$ or extract it from $N_l(t)$ by fitting it to a quadratic polynomial. Here we use the second (fitting) method to get $\frac{d^2}{dt^2}N_l\big|_{t=0}$.

At $t = 0$, Eqn. (4.10) becomes,

$$\ddot{x}|_{t=0} = f(x) + g(x)\frac{\sin^2(\pi\eta)}{\pi^2\eta^2}, \tag{4.11}$$

where $x = \frac{N_1}{N_{total}}$, $f(x) \equiv 2J_\perp^2(1-2x)$, and $g(x) \equiv 2J_\perp\frac{UN_{total}}{L}(1-2x)\sqrt{x(1-x)}$. When $x = 0$, the population imbalance between the two tubes is maximum, and all particles occupy the same tube. When $x = 1/2$, atoms are equally distributed between the tubes.

The fitted values of η that best reproduce the t-DMRG calculations obtained for different parameter regimes are shown in Table 4.2. Figure 4.18 shows comparisons between the aTWA results and the t-DMRG results for the optimal value of η found for one of the parameters displayed in Table II. In the GPE limit ($\eta = 0$), only the product UN_{total} enters in the equations of motion, meaning that, as long as UN_{total} is kept constant, the dynamics of the system are independent of U. This feature can be clearly seen in Eqn. (4.10). This is certainly not the behavior predicted by the t-DMRG solutions that show a slow down of the dynamics with increasing U. The TWA is expected to fully capture the role of quantum correlations at short times. Interestingly, we find that $\ddot{x}|_{t=0}$ computed by t-DMRG is extremely well described by $f(x) + g(x)\frac{\sin^2(\pi\eta)}{\pi^2\eta^2}$, where η is the only fitting parameter. The excellent agreement between t-DMRG and aTWA allows us to

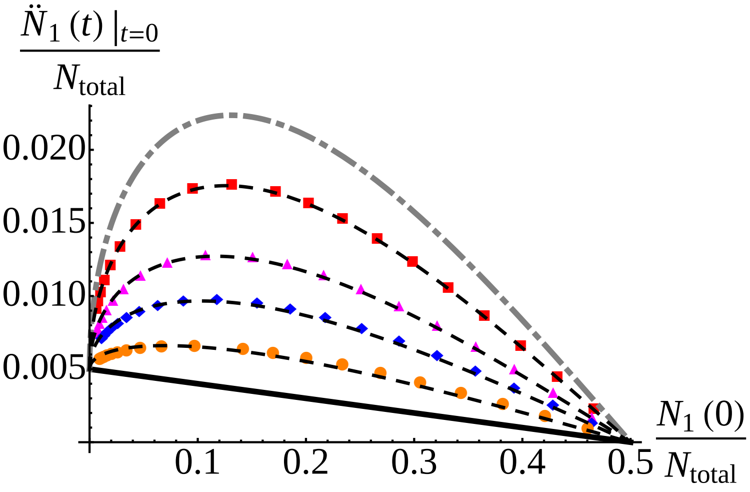

Figure 4.18: $\frac{\ddot{N}_1}{N_{total}}|_{t=0}$ (in units of $J_{\|}^2$) as a function of $\frac{N_1(t=0)}{N_{total}}, J = 0.05, UN_{total} = 30$. The solid black line shows the GPE limit, and the dash-dotted gray line the hard-core boson limit [see Eqn. (4.11)]. The red squares, magenta upper-triangles, blue diamonds, and orange disks show the initial curvature $\frac{\ddot{N}_1}{N_{total}}|_{t=0}$ extracted from the t-DMRG results at $U = 1$, $U = 2$, $U = 3$ and $U = 5$, respectively. The dashed black lines show the aTWA solutions using η as a fitting parameter. The values of η are listed in Table 4.2 . This plot is computed using the "case 2" parameters shown in Table 4.2.

conclude that the aTWA captures well the quantum correlations parameterized by η at short times in this simple two-tube model. We also see, that when UN_{total} is fixed in the parameter regime under consideration, the fitted values of η that best reproduce the t-DMRG calculations are almost independent of the initial population imbalance, i.e., $1 - 2x$, and the tunneling between tubes, i.e., $J_{\perp}$, when $J_{\perp} \ll J_{\|}$.

4.5.3 Long-time dynamics

In Fig. 4.19 we compare the GPE, the aTWA and the t-DMRG dynamics. We see significant deviations between the approximate methods and the t-DMRG at longer times. This shows that the dynamics of the Bose-Hubbard model on this ladder geometry is dominated by correlation effects. Although at short times the t-DMRG results are well described by the aTWA results with an appropriate value of η, at longer times the aTWA fails to reproduce the many-body dynamics. This behavior confirms the relevance of quantum correlations neglected by the aTWA. Those deviations are consistent with the deviations we saw when trying to model the experimental data with the aTWA.

Figure 4.19 shows that the weakly interacting regime is the regime where the GPE and the aTWA (with small η) predictions are closer to the t-DMRG results for longer times. The aTWA gives slightly better agreement at short times, indicating that for weak interactions, it better captures correlation effects. In the strongly interacting regime, tunneling is greatly suppressed, especially in the presence of a large initial population imbalance. While in the GPE and the aTWA, $N_1(t)$ oscillates with more or less constant frequency and amplitude, in the t-DMRG, $N_1(t)$ oscillates with a lower frequency and gradually "relaxes" towards an equal distribution of atoms in the two tubes.

To further quantify the quantum correlations (which are not captured in the GPE and are only partially captured in the aTWA) in the ladder system, we calculate the local pair correlation function, $g^{(2)}$, which is proportional to the probability of observing two particles in the same lattice site [39, 1]. For a 1D gas, when $\gamma \ll 1$, $g^{(2)} \to 1$, and when $\gamma \gg 1$, $g^{(2)} \to 0$. In our quasi 1D system, we define $g_l^{(2)}$ in the tube l as,

$$g_l^{(2)} = \frac{L}{N_l^2} \sum_i \langle \hat{n}_{l,i}^2 \rangle - \langle \hat{n}_{l,i} \rangle. \tag{4.12}$$

Figure 4.20 shows that $g_l^{(2)}$ decreases with increasing U (larger γ) and approaches zero when γ goes to infinity. $g_l^{(2)}$ is a slowly varying function when compared to the evolution of the total atomic population in each tube (N_l).

By using t-DMRG as a means to benchmark the GPE and the aTWA, we clearly see that while the aTWA is accurate at short times, both approaches break down at longer times. We can also clearly observe the complexity of the nonequilibrium behavior even in this simple coupled-tube model.

It is important to keep in mind that the two-tube model used in this section is much simpler than the multitube system of the experiment, where in addition the axial external confinement was turned off, and no lattice was present along the tubes. Consequently, the conclusions of this analysis

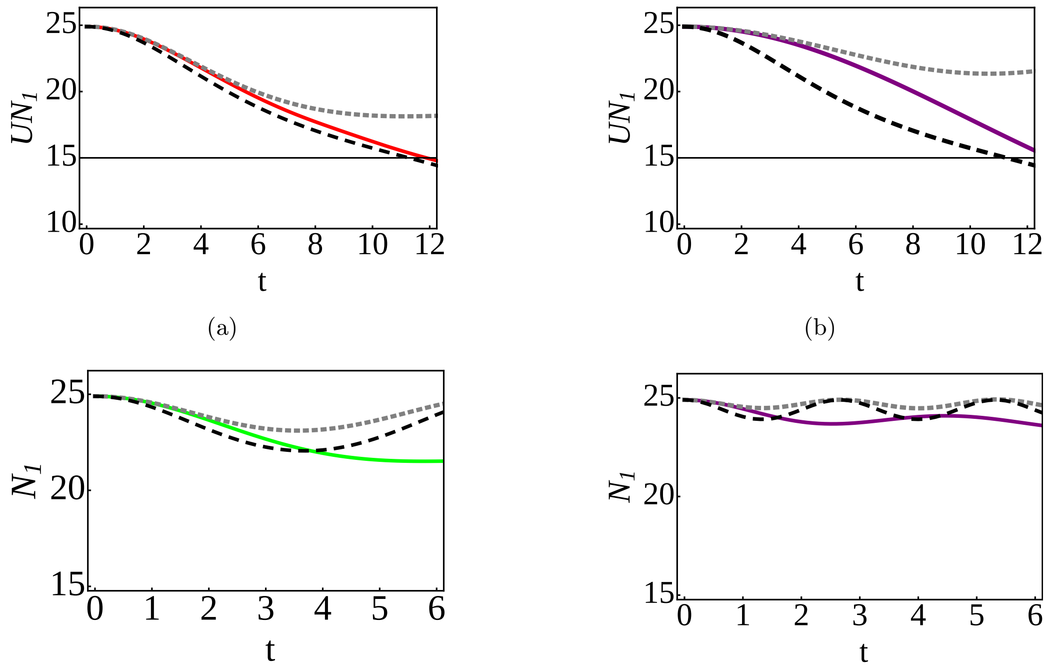

(a)

(b)

(c)

(d)

Figure 4.19: Evolutions of UN_1 (in units of $J_{\parallel}$) and N_1 as functions of time (in units of $1/J_{\parallel}$) calculated using the DMRG and GPE methods. In panel (a) and (b), the values of U are 1 and 5, respectively, while UN_{total} is fixed to 30. In panel (c) and (d), the values of U are 2 and 5, respectively, while N_{total} is fixed to 30. In each panel, the solid line is the t-DMRG solution, and the dashed black line is the mean-field calculation with no random phase (GPE). The dotted gray line is for (a) $\eta = 0.3$, (b) $\eta = 0.7$, (c) $\eta = 0.4$ and (d) $\eta = 0.53$.

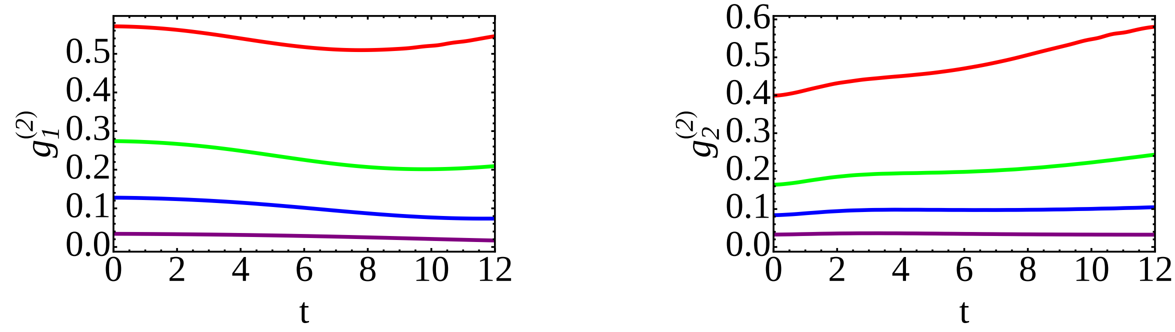

(a)

(b)

Figure 4.20: $g_l^{(2)}$ as a function of time in different regimes. The correlations are extracted from the t-DMRG results for the parameters describing case 2. Panel (a) shows $g_1^{(2)}$, $\frac{L}{N_1^2}\sum_i \langle \hat{n}_{1,i}^2 \rangle - n_{1,i}$, and Panel (b) shows $g_2^{(2)}$, $\frac{L}{N_2^2}\sum_i \langle \hat{n}_{2,i}^2 \rangle - n_{2,i}$. In each panel, from top to bottom, the lines correspond to $U = 1$, $U = 2$, $U = 3$, and $U = 5$, respectively.

cannot be simply compared to the experimentally observed dynamics. However, this simple two-tube model clearly shows that correlations can play a dominant role in suppressing the tunneling dynamics, without the need for density gradients. [1]

4.5.4 Discussion

Although we see decent agreement between the aTWA and the DMRG results at short times in the two-tube model, in the real experiment, we find that the aTWA deviates from the measurements almost as soon as the expansion starts. We will now discuss the various possible explanations for the experiment-theory discrepancy.

First, although the aTWA adds phase fluctuations that arise from quantum correlations, they are added in an *ad hoc* way, and not as the result of the system lowering its energy. In a complete theory (and presumably in the experiment) correlations build up in order to decrease the mean interaction energy. Since the wave function of a tunneling atom will not in general be appropriately correlated with the atoms in an adjacent tube, it would have to pay much of the interaction energy cost that the correlations avoid. If that energy cost is larger than the tunneling energy, then hopping between tubes will be suppressed. Although γ is not initially large near the central tubes, the fast density decrease due to the axial expansion could dynamically increase the quantum correlations, so that this mechanism could play an important role in suppressing transverse expansion.

Second, it is possible that the initial phase variations along the tubes, which are left out of the aTWA, could be important. Note, however, that phase variations along tubes are generated dynamically in the aTWA when atoms tunnel between tubes. Still, the resulting phase fluctuations may not be sufficient to capture the quantum dynamics.

Finally, we have seen recent experimental evidence that the initial atom distribution among the central tubes is flatter than a Thomas-Fermi profile. Such a distribution is probably a conse-

---

[1] In the strong coupling limit, correlation-suppressed tunneling is similar to Pauli Blocking. It does not require density gradients, which is why in the experiment the expansion of the central part of the tube bundle is fully suppressed until the overall density, and hence the mean-field cost of tunneling, gets sufficiently small. We speculate that such a process might tend to suppress mass transport whenever there is intermediate or strong coupling, regardless of the dimension [48, 95].

quence of the known nonadiabaticity of the 2D lattice turn-on, which leads to much-higher initial densities than adiabatic turn-on predicts, in a way that is quite insensitive to turn-on time. We expect that a more flat-top initial distribution would lead to less initial expansion, but it is not clear that it would be decreased enough to explain the experimental results. The limited spatial resolution of the experiment prevents us from directly checking the distribution of atoms among tubes and performing a calculation based on the result.

In summary, there remain several logical possibilities for the discrepancy between experiment and theory here. Further investigation is needed.

4.6 Conclusion

We have presented various mean-field and beyond-mean-field models to describe our recent experimental observations of interaction-induced localization effects during the expansion of an array of coupled 1D tubes. In contrast to previous 1D-lattice experiments, where a pure mean-field model was able to capture the observed MQST behavior, in our case, we find important corrections induced by quantum fluctuations. Thermal fluctuations and nonadibatic loading conditions, which are not accounted for in our analysis, may give rise to similar effects, but we have not explored those in this work. [2]

The addition of phase fluctuations in the initial conditions (aTWA) coarsely captured the main self-trapping features seen in the experiment, but underestimated the observed localization. The fact that the aTWA does not properly account for the full quantum correlations could be responsible for the failure of the theory to reproduce the experiment. Comparisons with t-DMRG calculations performed in a simple two-tube model find very good agreement between the aTWA and the t-DMRG at short times, but a break down of the aTWA at longer times. The two-tube calculations support the fact that quantum correlations, not captured by the mean-field model, can play an important role in suppressing tunneling. Further comparisons among the various methods

---

[2] It is hard to adiabatically transform a 3D gas into a 1D gas in theory [96], and there is some irreversibility in turning on the lattice.

used for modeling the dynamics and experiments are needed to help shed light on the complex many-body dynamics of coupled-correlated systems.

Bibliography

[1] I. Bloch, J. Dalibard, and W. Zwerger. Many-body physics with ultracold gases. Rev. Mod. Phys., 80:885, 2008.

[2] S. Peil et al. Patterned loading of a bose-einstein condensate into an optical lattice. Phys. Rev. A, 67:051603, 2003.

[3] P. Blair Blakie and Charles W. Clark. Wannier states and bose-hubbard parameters for 2d optical lattices. J. Phys. B: At. Mol., Opt. Phys., 37:1391, 2004.

[4] C. Orzel et al. Squeezed states in a bose-einstein condensate. Science, 291:2386, 2001.

[5] T. Kinoshita, T. Wenger, and D. S. Weiss. Observation of a one-dimensional tonks-girardeau gas. Science, 305:1125, 2004.

[6] B. Paredes et al. Tonks-girardeau gas of ultracold atoms in an optical lattice. Nature, 429:277, 2004.

[7] M. Greiner, O. Mandel, T. Esslinger, T. W. Hänsch, and I. Bloch. Quantum phase transition from a superfluid to a mott insulator in a gas of ultracold atoms. Nature, 415:39, 2002.

[8] M. Lewenstein et al. Ultracold atomic gases in optical lattices: mimicking condensed matter physics and beyond. Advances in Physics, 56:243, 2007.

[9] J. D. Jackson. Classical Electrodynamics. John Wiley & Sons, Inc., New York, 1999.

[10] R. Grimm, M. Weidemüller, and Y. B. Ovchinnikov. Optical dipole traps for neutral atoms. arXiv: physics/9902072v1, 1999.

[11] A. M. Rey. Ultracold bosonic atoms in optical lattices. PhD thesis, University of Maryland, 2004.

[12] N. W. Ashcroft and N. D. Mermin. Solid State Physics. Brooks/Cole, Cengage Learning, 1976.

[13] J. M. Ziman. Principles of the Theory of Solids. Cambridge University Press, 1964.

[14] M. Fisher, P. B. Weichman, G. Grinstein, and D. S. Fisher. Boson localization and the superfluid-insulator transition. Phys. Rev. B, 40:546, 1989.

[15] J. Hubbard. Electron correlations in narrow energy bands. Proceedings of the Royal Society of London Series a-Mathematical and Physical Sciences, 276:238, 1963.

[16] D. Jaksch, C. Bruder, J. I. Cirac, C. W. Gardiner, and P. Zoller. Cold bosonic atoms in optical lattices. Phys. Rev. Lett., 81:3108, 1998.

[17] T. Stöferle et al. Transition from a strongly interacting 1d superfluid to a mott insulator. Phys. Rev. Lett., 92:130403, 2004.

[18] I. B. Spielman, W. D. Phillips, and J. V. Porto. Mott-insulator transition in a two-dimensional atomic bose gas. Phys. Rev. Lett., 98:080404, 2007.

[19] I. B. Spielman, W. D. Phillips, and J. V. Porto. Condensate fraction in a 2d bose gas measured across the mott-insulator transition. Phys. Rev. Lett., 100:120402, 2008.

[20] T. Esslinger. Fermi-hubbard physics with atoms in an optical lattice. arXiv:1007.0012, 2010.

[21] E. Altman, E. Demler, and M. D. Lukin. Probing many-body states of ultracold atoms via noise correlations. Phys. Rev. A, 70:013603, 2004.

[22] M. H. Anderson, J. R. Ensher, M. R. Matthews, C. E. Wieman, and E. A. Cornell. Observation of bose-einstein condensation in a dilute atomic vapor. science, 269:198, 1995.

[23] K. B. Davis, M.-O. Mewes, M. R. Andrews, N. J. van Druten, D. S. Durfee, D. M. Kurn, and W. Ketterle. Bose-einstein condensation in a gas of sodium atoms. Phys. Rev. Lett., 75:3969, 1995.

[24] C. J. Pethick and H. Smith. Bose-Einstein Condensation in Dilute Gases. Cambridge University Press, Cambridge, 2002.

[25] M. R. Andrews, C. G. Townsend, H.-J. Miesner, D. S. Durfee, D. M. Kurn, and W. Ketterle. Observation of interference between two bose condensates. Science, 275:637, 1997.

[26] R. Hanbury Brown and R. Q. Twiss. Correlation between photons in two coherent beams of light. Nature, 177:27, 1956.

[27] N. Gemelke, X. Zhang, C-L. Hung, and C. Chin. In situ observation of incompressible mott-insulating domains in ultracold atomic gases. Nature, 460:995, 2008.

[28] W. S. Bakr, A. Peng, M. E. Tai, R. Ma, J. Simon, J. I. Gillen, S. Fölling, L. Pollet, and M. Greiner. Probing the superfluid-to-mott insulator transition at the single-atom level. Science, 329:547, 2010.

[29] J. F. Sherson, C. Weitenberg, M. Endres, M. Cheneau, I. Bloch, and S. Kuhr. Single-atom-resolved fluorescence imaging of an atomic mott insulator. Nature, 467:68, 2010.

[30] E. Toth, A. M. Rey, and P. B. Blakie. Theory of correlations between ultracold bosons released from an optical lattice. Phys. Rev. A, 78:013627, 2008.

[31] M. Köhl, H. Moritz, T. Stöferle, K. Günter, and T. Esslinger. Fermionic atoms in a three dimensional optical lattice: Observing fermi surfaces, dynamics, and interactions. Phys. Rev. Lett., 94:080403, 2005.

[32] R. Jördens, N. Strohmaier, K. Gunther, H. Moritz, and T. Esslinger. A mott insulator of fermionic atoms in an optical lattice. Nature, 455:204, 2008.

[33] U. Schneider et al. Metallic and insulating phases of repulsively interacting fermions in a 3d optical lattice. Science, 322:1520, 2008.

[34] S. Folling et al. Spatial quantum noise interferometry in expanding ultracold atom clouds. Nature, 434:481, 2005.

[35] T. Rom et al. Free fermion antibunching in a degenerate atomic fermi gas released from an optical lattice. Nature, 444:733, 2006.

[36] E. H. Lieb and Liniger. Exact analysis of an interacting bose gas. i. the general solution and the ground state. Phys. Rev, 130:1605, 1963.

[37] M. Olshanii. Atomic scattering in the presence of an external confinement and a gas of impenetrable bosons. Phys. Rev. Lett., 81:938, 1998.

[38] D. M. Gangardt and G. V. Shlyapnikov. Stability and phase coherence of trapped 1d bose gases. Phys. Rev. Lett., 90:010401, 2003.

[39] T. Kinoshita, T. Wenger, and D. S. Weiss. Local pair correlations in one-dimensional bose gases. Phys. Rev. Lett., 95:190406, 2005.

[40] D. R. Hofstadter. Energy levels and wave functions of bloch electrons in rational and irrational magnetic fields. Phys. Rev. B, 14:2239, 1976.

[41] M. Y. Azbel and M. Rubinstein. Resistance and phase diagram of quasi periodic systems. Phys. Rev. B, 27:6530, 1983.

[42] A. N. Kolmogorov. O dinamicheskikh sistemakh s integralnym invariantom na tore. Doklady Akad. Nauk SSSR, 93:763, 1953.

[43] I. C. Percival. Variational principle for invariant tori of fixed frequency. Journal of Physics A: Mathematical and General, 12:L57, 1979.

[44] K. Drese and M. Holthaus. Exploring a metal-insulator transition with ultracold atoms in standing light waves? Phys. Rev. Lett., 78:2932, 1997.

[45] S. Aubry and G. Andre. Proceedings of the Israel Physical Society, volume 3. Hilger, Bristol, 1979.

[46] J. B. Sokoloff. Unusual band structure, wave functions and electrical conductance in crystals with incommensurate periodic potentials. Physics Reports, 126:189, 1985.

[47] B. Laburthe-Tolra et al. Observation of reduced three-body recombination in a correlated 1d degenerate bose gas. Phys. Rev. Lett., 92:190401, 2004.

[48] C. D. Fertig et al. Strongly inhibited transport of a degenerate 1d bose gas in a lattice. Phys. Rev. Lett., 94:120403, 2005.

[49] L. Fallani, J. E. Lye, V. Guarrera, C. Fort, and M. Inguscio. Ultracold atoms in a disordered crystal of light: Towards a bose glass. Phys. Rev. Lett., 98:130404, 2007.

[50] V. Guarrera et al. Noise correlation spectroscopy of the broken order of a mott insulating phase. Phys. Rev. Lett., 100:250403, 2008.

[51] D.J. Thouless. J. Phys., C5:77, 1972.

[52] S. Ostlund and R. Pandit. Renormalization-group analysis of the discrete quasiperiodic schrodinger equation. Phys. Rev. B, 29:1394, 1984.

[53] S. Ostlund, R. Pandit, D. Rand, H. J. Schellnhuber, and E. D. Siggia. One-dimensional schrodinger equation with an almost periodic potential. Phys. Rev. Lett., 50:1873, 1983.

[54] D. Rand, S. Ostlund, J. Sethna, and E. Siggia. Phys Rev. Lett., 49:132, 1983.

[55] S.J. Shenker and L.P. Kadanoff. J. Stat. Phys., 27:631, 1982.

[56] E.I. Dinaburg and Ya. G. Sinai. Func. Anal. Appl., 9:279, 1976.

[57] E. Ott. Chaos in Dynamical Systems. Cambridge University Press, 1993.

[58] A. M. Rey, I. I. Satija, and C. W. Clark. Hanbury brown-twiss interferometry for fractional and integer mott phases. New Journal of Physics, 8:155, 2006.

[59] A. M. Rey, I. I. Satija, and C. W. Clark. Quantum coherence of hard-core bosons: Extended, glassy, and mott phases. Phys. Rev. A, 73:063610, 2006.

[60] A. M. Rey, I. I. Satija, and C. W. Clark. Noise correlations of fermions and hard core bosons in a quasi-periodic potential. Laser Physics, 17:205, 2007.

[61] T. Roscilde. Bosons in one-dimensional incommensurate superlattices. Phys. Rev. A, 77:063605, 2008.

[62] Jukka A.Ketoja and Indubala I. Satija. Self-similarity and localization. Phys. Rev. Lett., 75:2762, 1995.

[63] A. Óttl, S. Ritter, M. Kóhl, and T. Esslinger. Correlations and counting statistics of an atom laser. Phys. Rev. Lett, 95:090404, 2005.

[64] C. L. Hung, X. Zhang, N. Gemelke, and C. Chin. Slow mass transport and statistical evolution of an atomic gas across the superfluidcmott-insulator transition. Phys. Rev. Lett, 104:160403, 2010.

[65] Aaron Reinhard, Jean-Felix Riou, Laura A. Zundel, David S. Weiss, Shuming Li, Ana M. Rey, and Rafael Hipolito. Self-trapping in an array of coupled 1d bose gases. Phys. Rev. Lett., 110:033001, 2013.

[66] Anatoli Polkovnikov. Phase space representation of quantum dynamics. Annals of Physics, 325:1790–1852, 2010.

[67] U. Schollwöck. The density-matrix renormalization group. Rev. Mod. Phys, 77:259, 2005.

[68] A. J. Daley, C. Kollath, U. Schollwöck, and G. Vidal. J. Stat. Mech, page 04005, 2004.

[69] T. Kinoshita, T. Wenger, and D. S. Weiss. All-optical bose-einstein condensation using a compressible crossed dipole trap. Phys. Rev. A, 71:011602, 2005.

[70] L. D. Landau. Z. Phys. (N.Y.), 13:905, 1933.

[71] A. L. Shluger and A. M. Stoneham. Small polarons in real crystals: concepts and problems. J. Phys.: Condens. Matter, 5:3049, 1993.

[72] E. K. H. Salje, A. S. Alexandrov, and W. Y. Liang. Polarons and Bipolarons in High Temperature Superconductors and Related Materials. Cambridge University Press, Cambridge, England, 1995.

[73] A. J. Millis, P. B. Littlewood, and B. I. Shraiman. Phys. Rev. Lett., 74:5144, 1995.

[74] G. Wellein and H. Fehske. Self-trapping problem of electrons or excitons in one dimension. Phys. Rev. B, 58:6208, 1998.

[75] Z. H. Musslimani and J. Yang. J. Opt. Soc. Am. B, 21:973, 2004.

[76] M. Hartmann, F. Brandao, and M. Plenio. Laser Photon. Rev., 2:527, 2008.

[77] P. Martinoli and C. Leemann. J. Low. Temp. Phys., 118:699, 2000.

[78] G. J. Milburn, J. Corney, E. M. Wright, and D. F. Walls. Quantum dynamics of an atomic bose-einstein condensate in a double-well potential. Phys. Rev. A, 55:4318, 1997.

[79] A. Smerzi, S. Fantoni, S. Giovanazzi, and S. R. Shenoy. Quantum coherent atomic tunneling between two trapped bose-einstein condensates. Phys. Rev. Lett., 79:4950, 1997.

[80] S. Raghavan, A. Smerzi, S. Fantoni, and S. R. Shenoy. Coherent oscillations between two weakly coupled bose-einstein condensates: Josephson effects, pi oscillations, and macroscopic quantum self-trapping. Phys. Rev. A, 59:620, 1999.

[81] A. Trombettoni and A. Smerzi. Discrete solitons and breathers with dilute bose-einstein condensates. Phys. Rev. Lett., 86:2353, 2001.

[82] O. Morsch, M. Cristiani, J. H. Muller, D. Ciampini, and E. Arimondo. Free expansion of a bose-einstein condensate in a one-dimensional optical lattice. Phys. Rev. A, 66:021601(R), 2002.

[83] A. Smerzi and A. Trombettoni. Nonlinear tight-binding approximation for bose-einstein condensates in a lattice. Phys. Rev. A, 68:023613, 2003.

[84] T. J. Alexander, E. A. Ostrovskaya, and Y. S. Kivshar. Phys. Rev. Lett., 96:040401, 2006.

[85] Ju-Kui Xue, Ai-Xia Zhang, and Jie Liu. Self-trapping of bose-einstein condensates in optical lattices:the effect of the lattice dimension. Phys. Rev. A, 77:013602, 2008.

[86] S. Wüster, B. J. Dabrowska-Wüster, and M. J. Davis. Phys. Rev. Lett, 109:080401, 2012.

[87] M. Albiez et al. Direct observation of tunneling and nonlinear self-trapping in a single bosonic josephson junction. Phys. Rev. Lett., 95:010402, 2005.

[88] T. Anker et al. Nonlinear self-trapping of matter waves in periodic potentials. Phys. Rev. Lett., 94:020403, 2005.

[89] M. Girardeau. Relationship between systems of impenetrable bosons and fermions in one dimension. Journal of Mathematical Physics, 1:516, 1960.

[90] B. Paredes, A. Widera, V. Murg, O. Mandel, S. Fölling, I. Cirac, G. V. Shlyapnikov, T. W. Hänsch, and I. Bloch. Tonks-girardeau gas of ultracold atoms in an optical lattice. Nature, 429:277, 2004.

[91] V. Dunjko, V. Lorent, and M. Olshanii. Bosons in cigar-shaped traps: Thomas-fermi regime, tonks-girardeau regime, and in between. Phys. Rev. Lett., 86:5413, 2001.

[92] P. B. Blakie, A. S. Bradley, M. J. Davis, R. J. Ballagh, and C. W. Gardiner. Dynamics and statistical mechanics of ultra-cold bose gases using c-field techniques. Advances in Physcs, 57:5:363–455, 2008.

[93] A.Sinatra, C. Lobo, and Y.Castin. Rigorous results on valence-bond ground-states in antiferromagnets. J. Phys. B, 35:3599, 2002.

[94] Rafael Hipolito and Anatoli Polkovnikov. Breakdown of macroscopic quantum self-trapping in coupled mesoscopic one-dimensional bose gases. Phys. Rev. A, 81:013621, 2010.

[95] J. Mun et al. Phase diagram for a bose-einstein condensate moving in an optical lattice. Phys. Rev. Lett., 99:150604, 2007.

[96] A. Polkovnikov and V. Gritsev. Breakdown of the adiabatic limit in low-dimensional gapless systems. Nat. Phys., 4:477, 2008.

Appendix A

Time-of-flight image in a single-particle expansion

Considering one atom initially trapped in the optical lattice at lattice site i, the wave function of the atom is $w(x-x_i)$. Assuming at time $t=0$, the lattice potential is suddenly turned off, and the atom freely expands. The wave function of the atom after some time t is,

$$\psi(x,t) = \frac{1}{\sqrt{2\pi}} \int e^{iq(x-x_i)} \tilde{w}(q) e^{-i\frac{\hbar q^2 t}{2M}} dq = \int dx' \left[\frac{1}{2\pi} \int e^{iq(x-x')-i\frac{\hbar q^2 t}{2M}} dq \right] w(x'-x_i), \tag{A.1}$$

where $\tilde{w}(q)$ is the Fourier transform of $w(x)$, i.e., $\tilde{w}(q) = \frac{1}{\sqrt{2\pi}} \int e^{-iqx} w(x) dx$. Therefore,

$$\begin{aligned} n(x,t) &= |\psi(x,t)|^2 = \frac{1}{2\pi} \int e^{iq(x-x_i)} \tilde{w}(q) e^{-i\frac{\hbar q^2 t}{2M}} e^{-iq'(x-x_i)} \tilde{w}^*(q') e^{i\frac{\hbar q'^2 t}{2M}} dq', && \text{(A.2)} \\ &= \frac{M}{2\pi\hbar t} \left| \int e^{-i\frac{M}{\hbar t}(x-x_i)x_1 + i\frac{M}{2\hbar t}x_1^2} w(x_1) dx_1 \right|^2 . && \text{(A.3)} \end{aligned}$$

Assuming the width of the Wannier function $w(x-x_i)$ is x_0, when the expansion time is long enough such that $\frac{M}{\hbar t} x_i x_0 \ll 1$, and $\frac{M}{\hbar t} x_0^2 \ll 1$, we have

$$n(x,t) \approx \frac{M}{2\pi\hbar t} \left| \int e^{-i\frac{Mx}{\hbar t}x_1} w(x_1) dx_1 \right|^2 = \frac{M}{\hbar t} \left| \tilde{w}(Q) \right|^2 , \tag{A.4}$$

with $Q = \frac{Mx}{\hbar t}$. This expression represents an important approximation in the time-of-flight technique, i.e., the density distributions in the time-of-flight images actually show the momentum distribution before the lattice is turned off.

Appendix B

Mapping from position-to-momentum space

As we have mentioned in chapter 3, η_k is connected to z_n by the relation that $z_n = \eta_k e^{-in\phi}$ with $k = \text{Mod}[nF_{M-1}, F_M]$, while θ is set to 0. Combining the above relation with Eqn. (3.10), we can shown that the experimentally relevant variables, η_k, satisfy the following equation:

$$-\left(\eta_{\text{Mod}[k+F_{M-1},F_M]}e^{-i\phi} + \eta_{\text{Mod}[k-F_{M-1},F_M]}e^{i\phi}\right) + \frac{2}{\lambda}\cos(2\pi k/F_M)\eta_k = -\frac{\epsilon}{\lambda}\eta_k \qquad \text{(B.1)}$$

Here we provide an example ($\phi = 3\pi/4$) of the mapping between position coordinates j and quasi-momentum coordinates k, represented by $K(j)$ that we use to link the quasi-momentum-position observables. In the plot, we highlight the Fibonacci sites. A small system size is used to make the visualization clearer.

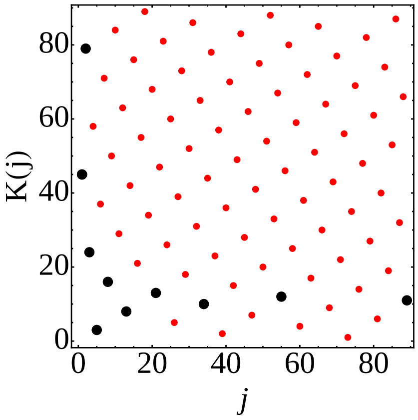

Figure B.1: Mapping from j to k , denoted by $K(j)$ used to determine momentum-space observables from position-space observables and vice versa. Larger points are Fibonacci sites. Here we choose $F_M = 87$, and $K(j)$ is the relation that maps j to k.

Appendix C

Perturbation theory and dimerized states

We begin our analysis with the Harper equation (3.2). For $\lambda \to \infty$, the single-particle wave functions are localized at individual lattice sites, $\psi_j^{(m)} = \delta_{j,L_m}$ and $\epsilon^{(m)} = \cos(2\pi\sigma L_m + \phi)$, where L_m is defined by $\cos(2\pi\sigma L_{m-1} + \phi) \leq \cos(2\pi\sigma L_m + \phi)$. When $\lambda \gg 1$, we can get the single-particle wave function through exact diagonalization, or we can use the perturbation theory to obtain the approximate eigenvalues and eigenfunctions.

We focus first on the site L_m. Assuming that $2\lambda|\cos(2\pi\sigma L_m + \phi) - \cos(2\pi\sigma(L_m \pm 1) + \phi)| \gg 1$, non-degenerate perturbation theory can be used, and the results are:

$$\epsilon^{(m,0)} = 2\lambda\cos(2\pi\sigma L_m + \phi), \tag{C.1}$$

$$\epsilon^{(m,1)} = 0, \tag{C.2}$$

$$\epsilon^{(m,2)} = \frac{1}{\epsilon^{(m,0)} - 2\lambda\cos[2\pi\sigma(L_m+1)+\phi]} + \frac{1}{\epsilon^{(m,0)} - \cos[2\pi\sigma(L_m-1)+\phi]}, \tag{C.3}$$

$$\psi_j^{(m,0)} = \delta_{L_m,j}, \text{ and} \tag{C.4}$$

$$\psi_j^{(m,1)} = -\left\{\frac{\delta_{L_m+1,j}}{\epsilon^{(m,0)} - 2\lambda\cos[2\pi\sigma(L_m+1)+\phi]} + \frac{\delta_{L_m-1,j}}{\epsilon^{(m,0)} - 2\lambda\cos[2\pi\sigma(L_m-1)+\phi]}\right\}, \tag{C.5}$$

where $\epsilon^{(m,0)}$, $\epsilon^{(m,1)}$, $\epsilon^{(m,2)}$ are the zeroth, first, and second order terms of the eigenvalue $\epsilon^{(m)}$, with a similar meaning for $\psi_j^{(m,0)}$ and $\psi_j^{(m,1)}$. Also, $|\psi_j^{(m)}|^2 = \delta_{L_m,j} + O\left[\left(\frac{1}{\lambda}\right)^2\right]$. So, up to first order of $\frac{1}{\lambda}$, $\sum_j \left|\psi_j^{(m)}\right|^2 = 1$.

For other sites L_m that satisfy $1 \approx 2\lambda|\cos(2\pi\sigma L_m + \phi) - \cos[2\pi\sigma(L_m+1)+\phi]|$, nondegenerate perturbation theory doesn't work and degenerate perturbation theory will be used. In that case, the zero-order energies ϵ and eigenfunctions ψ satisfy:

$$\begin{pmatrix} 2\lambda\cos(2\pi\sigma L_m+\phi) & -1 \\ -1 & 2\lambda\cos[2\pi\sigma(L_m+1)+\phi] \end{pmatrix} \begin{pmatrix} \psi^{(m,0)}_{L_m} \\ \psi^{(m,0)}_{L_m+1} \end{pmatrix} = \epsilon \begin{pmatrix} \psi^{(m,0)}_{L_m} \\ \psi^{(m,0)}_{L_m+1} \end{pmatrix}. \tag{C.6}$$

The above equations result in a pair of energies that we denote as ϵ_u and ϵ_d:

$$\epsilon_d = \lambda\{\cos(2\pi\sigma L_m+\phi)+\cos[2\pi\sigma(L_m+1)+\phi]\} - \sqrt{1+\Lambda_m^2}, \text{and} \tag{C.7}$$

$$\epsilon_u = \lambda\{\cos(2\pi\sigma L_m+\phi)+\cos[2\pi\sigma(L_m+1)+\phi]\} + \sqrt{1+\Lambda_m^2}, \tag{C.8}$$

where $\Lambda_m = \lambda\{\cos(2\pi\sigma L_m+\phi) - \cos[2\pi\sigma(L_m+1)+\phi]\}$. The corresponding orthogonal eigenfunctions can be written as:

$$\psi_d = \begin{pmatrix} A \\ B \end{pmatrix} \quad \text{and} \quad \psi_{\mathrm{u}} = \begin{pmatrix} B \\ -A \end{pmatrix}, \tag{C.9}$$

where $A = \sqrt{\frac{\sqrt{\Lambda_m^2+1}-\Lambda_m}{2\sqrt{\Lambda_m^2+1}}}$, and $B = \sqrt{\frac{\sqrt{\Lambda_m^2+1}+\Lambda_m}{2\sqrt{\Lambda_m^2+1}}}$. We can choose α (β) to be the greater (lesser) of A and B: $|\alpha|^2 = \frac{\sqrt{1+\Lambda_m^2}+|\Lambda_m|}{2\sqrt{1+\Lambda_m^2}}$, $|\beta|^2 = \frac{\sqrt{1+\Lambda_m^2}-|\Lambda_m|}{2\sqrt{1+\Lambda_m^2}}$. From these results one can see that $|\alpha|^2$ increases as $|\Lambda_m|$ increases. For example, when $|\Lambda_m| = 0$, $|\alpha|^2 = 0.5$ and when $|\Lambda_m| = \infty$, $|\alpha|^2 = 1$.

When $|\Lambda_m| \ll 1$, $|\beta|^2$ is comparable to $|\alpha|^2$, and the states are localized at the same two neighboring sites. Hence, they will be referred as a *pair of dimerized states* [The numerical results are shown in Fig.C.1 (a)]. The dimerized states are found by noticing that:

$$\cos(2\pi\sigma L_m+\phi) - \cos[2\pi\sigma(L_m+1)+\phi] = 2\sin[2\pi\sigma(L_m+1/2)+\phi]\sin(\pi\sigma). \tag{C.10}$$

So for the points that satisfy $|\sin\left[2\pi\sigma(L_m+\frac{1}{2})+\phi\right]| \ll \frac{1}{\lambda}$, dimerized sites exist at L_m, and L_m+1. Since $\sigma = \frac{F_{M-1}}{F_M}$, it is clear that we can construct the relation $\mathrm{Mod}[2\pi\sigma L_m + \phi, 2\pi] \approx 2\pi\ \mathrm{Mod}[B_m/F_M, 1]$, where $m \in (1,2,\ldots,F_M)$ are indexes of increasing energy level, $L_m \in (1,2,\ldots,F_M)$ are indexes of sites' positions, and $B_m = \mathrm{Mod}[L_m \times F_{M-1} + l, F_M] \in (0,1,2,\ldots,F_M-1)$ are indexes that we introduce for the convenience of discussion (l is the closest integer to $\frac{\phi}{2\pi}F_M$). Using this relation, it can be shown that $m \approx 2|B_m - F_M/2|$ (we use $\approx$ here, since the exact expression for even and odd F_M are slightly different). The relations of m, L_m and B_m are plotted for the case of $F_M = 610$ in Fig. C.1 (b).

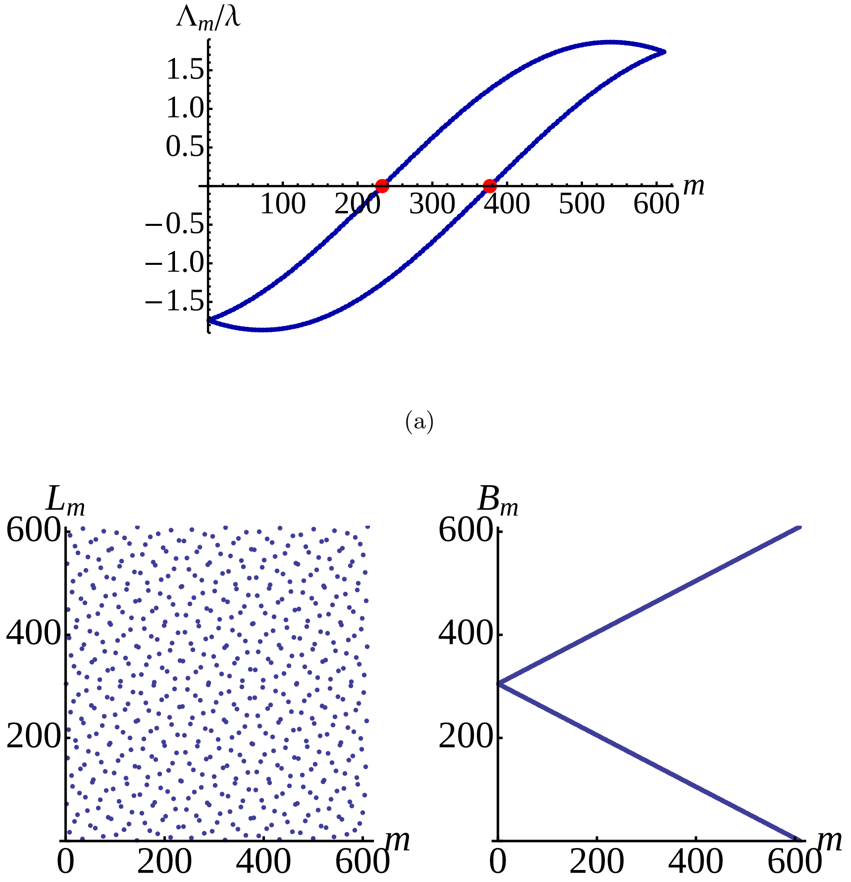

(a)

(b)

Figure C.1: Panel (a) shows numerically that at the two red points, $m_1 = F_{M-1}$ and $m_2 = F_{M-2}$, Λ_m vanishes, so that degenerate perturbation theory is required. Panel (b) shows the relations of L_m, B_m and m (see text) for $\phi = \frac{3\pi}{4}$. The relations between L_m and m are very sensitive to the value of ϕ while the relations between B_m and m are not sensitive at all.

As we discussed, the dimerized states L_m satisfy:

$$\sin(2\pi\sigma(L_m + 1/2) + \phi) \approx 0. \tag{C.11}$$

Writing the above equation in terms of B_m, we get:

$$\sin\left(\frac{2\pi B_m}{F_M} + \pi\sigma\right) \approx 0.$$

The solutions are $\frac{2B_m+F_{M-1}}{F_M} \approx 1$ or 2. Therefore,

$$B_{m_1} \approx (F_M - F_{M-1})/2. \tag{C.12}$$

$$B_{m_2} \approx (2F_M - F_{M-1})/2. \tag{C.13}$$

which correspond to:

$$m_1 \approx |2(B_{m_1} - F_{M/2})| \approx F_{M-1}. \tag{C.14}$$

$$m_2 \approx |2(B_{m_2} - F_M/2)| \approx F_{M-2}. \tag{C.15}$$

A detailed analysis shows that the band opens exactly at $m_1 = F_{M-1}$ and $m_2 = F_{M-2}$, regardless of F_M being even or odd. This demonstrates, at perturbative level, the special behavior of the return map at the irrational filling number F_{M-2} or F_{M-1} (See Fig.3.2).

In our calculations, we find out those L_m with the lowest values of $|\sin(2\pi\sigma(L_m + 1/2) + \phi)|$ (avoiding double counting of L_m in different pairs) and then apply to those points the perturbation theory we discussed above.

Because of the latter considerations, it is possible to demonstrate that around $m_1 = F_{M-1}$ or $m_2 = F_{M-2}$, there exists a sequence of paired states, exhibiting the following relationships as $\lambda \to \infty$,

$$\begin{aligned} \psi_d^{i,\tau} &= \sqrt{A_i}\delta_{j,L_{m_\tau-i}} + \sqrt{1-A_i}\delta_{j,L_{m_\tau-i}+1}, \\ \psi_u^{i,\tau} &= \sqrt{1-A_i}\delta_{j,L_{m_\tau-i}} - \sqrt{A_i}\delta_{j,L_{m_\tau-i}+1}, \end{aligned}$$

with $i \ll F_M$, and $\tau = 1, 2$. These states determine the properties of the system when the Fermi energy is close to the major gaps, i.e., $\nu = \sigma$, or $\nu = 1 - \sigma$, and thus the main properties of the band insulator phases.

Appendix D

Variational method for 1D optical lattice

In a deep 1D optical lattice, the external potential V_{ext} is composed of a 1D lattice potential $V_{lat} = V_0 \sin^2(\pi x/d)$ and an external magnetic or dipole confinement $V_{dip} = \frac{1}{2}M(\omega_x^2 x^2 + \omega_y^2 y^2 + \omega_z^2 z^2)$, where V_0 is the lattice depth, and d is the lattice spacing. In the tight-binding approximation, the macroscopic wave function can be written as,

$$\Psi = \sum_j \psi_j(t)\phi_j[\vec{x}, N_j(t)]. \tag{D.1}$$

$\phi_j[\vec{x}, N_j(t)]$, which is centered at the minimum of the jth well, is a time-dependent function that depends on the particle number on site j at a given instant and on the trapping frequencies along the two transverse directions. $\phi_j[\vec{x}, N_j(t)]$ is normalized to 1, i.e., $\int d\vec{x}\phi_j[\vec{x}, N_j(t)]^2$=1.

By using the tight-binding approximation, Eqn. (D.1), and after integrating out the spatial degrees of freedom in the GPE, one gets the so-called discrete nonlinear Schrödinger equation (DNLS)[83],

$$i\hbar\frac{\partial \psi_j}{\partial t} = \epsilon_j \psi_j - J(\psi_{j+1} + \psi_{j-1}) + \mu_j \psi_j. \tag{D.2}$$

The on-site energies ϵ_j arise from the external potential (along the lattice direction) superimposed on the optical lattice, i.e.,

$$\epsilon_j \quad = \quad \int d\vec{x}\ \phi_j(\vec{x})^2 \frac{1}{2} M \omega_x^2 x^2 = \frac{1}{2} M \omega_x^2 d^2 j^2. \tag{D.3}$$

J is the tunneling matrix between adjacent sites,

$$J = \int d\vec{x}\ \phi_j(\vec{x}) \left[\frac{\hbar^2}{2M}\frac{\partial^2}{\partial x^2} - V_{lat}\right] \phi_{j\pm 1}(\vec{x}), \tag{D.4}$$

and μ_j^{loc} is the “local” chemical potential,

$$\begin{aligned}\mu_j^{loc} &= \mu_j^{kin} + \mu_j^{int} + \mu_j^{pot} \\ &= \int d\vec{x}\, \frac{\hbar^2}{2M}\left(\vec{\nabla}\phi_j\right)^2 + g\left|\psi_j(t)\right|^2 \int d\vec{x}\ \left|\phi_j\right|^4 + \int d\vec{x}\ \phi_j^2 \frac{1}{2} M\left(\omega_y^2 y^2 + \omega_z^2 z^2\right). \qquad \text{(D.5)}\end{aligned}$$

Depending on the relative values of the dipole-trapping frequencies and the on-site chemical potential, the condensates in each well of the lattice can be regarded as 0D, 1D and 2D. The effective dimensionality of the condensate gives a different scaling of the local potential with the number of atoms [83],

$$\mu_j^{\text{loc}} = U_\alpha |\psi_j|^\alpha, \qquad \text{(D.6)}$$

where $\alpha = \frac{4}{2+D}, D = 0, 1, 2$ is the dimensionality of the condensate, and U_α is a constant that does not depend on the particle number or site index. The effective Hamiltonian of the system is [83]

$$H_{eff} = \sum_j \left[\epsilon_j |\psi_j|^2 - J(\psi_j^* \psi_{j+1} + c.c) + \frac{2}{2+\alpha} U_\alpha \left|\psi_j\right|^{\alpha+2}\right]. \qquad \text{(D.7)}$$

To proceed further, a variational method can be used. For this method, we assume that the amplitudes ψ_j can be, to a good approximation, parameterized by a Gaussian function, $\psi_j(t) = \sqrt{N}\sqrt[4]{\frac{2}{\pi r(t)^2}} \exp\left[-\frac{(j-\xi)^2}{r(t)^2} + ip(j-\xi) + i\frac{\delta(t)}{2}(j-\xi)^2\right]$. From this assumption, we can determine the equations of motion of $q_i(t) = \{r, \delta, p, \xi\}$. Here N is the particle number, $\xi(t)$ and $r(t)$ are, respectively, the center and the width of the atom distribution, and $p(t)$ and $\delta(t)$ are their associated conjugate momenta (in the lattice units). For the case $\epsilon_j = 0$, the effective Hamiltonian under this assumption becomes

$$H_{eff} = 2JN\left[-\cos p e^{-\sigma} + \left(\frac{2}{2+\alpha}\right)^{\frac{3}{2}} \left(\frac{2}{\pi}\right)^{\frac{\alpha}{4}} \frac{\Lambda}{r^{\alpha/2}}\right], \qquad \text{(D.8)}$$

where $\sigma = \frac{1}{2r^2} + \frac{r^2\delta^2}{8}$, $\Lambda = \frac{N^{\alpha/2}U_\alpha}{2J}$. The quasi-momentum dependence of the effective mass, $m^{*-1} \equiv \frac{\partial^2 H}{\partial p^2} = \cos p e^{-\sigma}$, and group velocity, $\nu_g \equiv \frac{\partial H}{\partial p} = \tan p/m^*$, allows a rich variety of dynamical regimes. A diverging effective mass $m^* \to \infty$ is the signature of wave-packet self-trapping.

The variational method has been shown to be a great success in characterizing various regimes of the dynamics. It also gives a critical value of MQST-to-diffusive transition (when $r_0 \gg 1$, where

r_0 is the initial value of r) as

$$\Lambda_c = r_0^{\alpha/2} \left(\frac{2+\alpha}{2}\right)^{3/2} \left(\frac{\pi}{2}\right)^{\alpha/4}. \tag{D.9}$$

Based on the variational method, when $\Lambda > \Lambda_c$ (MQST regime), $m^*(t \to \infty) \to \infty$. The ratio between r_0 and the asymptotic width $r_{\max}(t \to \infty)$ is given by the relation $\frac{r_0}{r_{max}} = \left(1 - \frac{\Lambda_c}{\Lambda}\right)^{\frac{2}{\alpha}}$. When $\Lambda \leq \Lambda_c$ (the diffusive regime), $m^*(t \to \infty) \to \frac{\Lambda_c}{\Lambda_c - \Lambda}$, $r(t \to \infty) \to \infty$. The same variational method has also been extended into 2D and 3D optical lattices with 0D condensates [85].